Bayerische Julius-Maximilians-Universität Würzburg
Fakultät für Physik und Astronomie
Lehrstuhl für Astronomie

Master Thesis

VLBI Monitoring of Five TeV Blazars

Author
Amar Hekalo

Supervisor
Prof. Dr. Matthias Kadler

A thesis submitted in fulfillment of the requirements
for the degree of Master of Science
in the group of

Prof. Dr. Matthias Kadler

Chair of Astronomy

Deutsche Zusammenfassung

Aktive Galaxienkerne (Active Galactic Nuclei, AGN) gehören zu den hellsten Objekten im Himmel und können im gesamten elektromagnetischen Spektrum beobachtet werden, von Radio-Frequenzen bis hin zu γ-Strahlung. Einige AGN, welche starke Radiostrahlung aussenden, besitzen hochrelativistische Jets, Materieströme bestehend aus relativistischen geladenen Teilchen, welche entgegengesetzt zueinander aus dem supermassiven schwarzen Loch im Zentrum jedes AGN propagieren. Abhängig von ihren spezifischen Emissionseigenschaften können sie in verschiedene Klassen unterteilt werden.

Besonders interessant hier ist die Unterklasse der BL Lac Objekte, genauer gesagt solche, die ihr Emissionsmaximum in höheren Frequenzen aufweisen (high frequency peaked BL Lac, HBL). Für BL Lac Objekte zeigt der Jet nur unter einem kleinen Winkel, also fast direkt, zum Beobachter, sodass es zu Effekten von Doppler Boosts und scheinbarer Überlichtgeschwindigkeit (superluminal motion) aufgrund von Projektionseffekten kommt. Diese Objekte weisen starke Emission bis zu sehr hohen Energien (very high energy, VHE) im Bereich von TeV auf. Diese Emission ist auf Zeitskalen bis hinunter zu Minuten stark variabel. Daraus lassen sich hohe intrinsische Lorentzfaktoren der Jets berechnen, welche bis zu $\Gamma \sim 50$ betragen.

Die Technik der Very Long Baseline Interferometrie (VLBI) kombiniert Radioteleskope, die auf der ganzen Welt verteilt sind, zu einem Array, um Auflösungen auf mas-Skalen zu erreichen. Damit lassen sich die innersten Regionen eines Jets auflösen und mit kreiförmigen Gaussschen Komponenten modellieren, um die projizierte, oder auch scheinbare, Geschwindigkeit des Jets zu berechnen. Anders als die VHE Ergebnisse zeigen Studien von Piner & Edwards größtenteils subluminale oder nur leicht superluminale Geschwindigkeiten. Diese Diskrepanz der intrinsischen und scheinbaren Geschwindigkeiten ist bekannt als Dopplerkrise. Ein-Zonen-Jetmodelle benötigen dabei unvernünftig kleine Sichtwinkel $\ll 1\,^\circ$, um diesen Sachverhalt zu erklären.

Das Ziel dieser Thesis ist es, eine unabhängige Studie mit VLBI Daten eines ausgewählten Samples an TeV Blazaren zu analysieren und die bereits bekannten Ergebnisse zu bestätigen oder zu bestreiten. Das Sample besteht aus den Quellen PKS 1440−389, PKS 0447−439, PKS 2005−489, PKS 2155−304 und PKS 0625−354, also fast alle Blazare aus dem TANAMI (Tracking Active galactic Nuclei with Austral Milliarcsecond Interferometry) Sample, welche im TeV-Bereich detektiert und hell genug sind, um bei 8.4 GHz beobachtet werden zu können. TANAMI ist ein Multiwellenlängen-Programm mit Fokus auf VLBI, welches Quellen südlich einer Deklination von $\delta < -30\,^\circ$ beobachtet. Alle untersuchten Jets des Samples weisen entweder stationäre, subluminale oder nur

leicht superluminale Bewegung auf. PKS 2155−304 besitzt dabei die schnellste Komponente mit $(7.8\pm2.5)c$, was die zuvor gewonnen Ergebnisse von Piner & Edwards bestätigt und erweitert. Weitere Eigenschaften, wie die Inklination von PKS 0625−354, die Krümmung des Jets von PKS 2155−304, sowie Multi-Zonen-Jetmodelle, die die Dopplerkrise versuchen zu lösen, werden ebenfalls diskutiert.

Abstract

Active Galactic Nuclei (AGN) are some of the brightest sources found in the sky and can be observed throughout the entire electromagnetic spectrum, from radio frequencies up to the γ-rays. Some AGN, which are strong radio emitters, feature highly relativsitic jets, streams of matter consisting of relativistic charged particles, propagating opposite to each other from the supermassive black hole in the center of every AGN. They can be divided into several different classes based on their specific emission properties.

Of particular interest here is the subclass of BL Lac objects, and more precisely the class of high frequency peaked BL Lacs (HBL). In the case of BL Lacs, the jet is pointed under a low angle to the observer, leading to effects of Doppler boosting and apparent superluminal motion, i.e. motion faster than the speed of light due to the projection. These objects feature strong emission up to very high energies (VHE) in the range of TeV. This emission is highly variable on timescales down to minutes, from which high intrinsic bulk Lorentz factors of the jet can be derived to be $\Gamma \sim 50$.

The technique of Very Long Baseline Interferometry (VLBI) combines radio telescopes stationed across the globe in an array to reach resolution on the scales of mas. With this, the innermost regions of a jet can be resolved and modelled with circular Gaussian model components to compute the projected, or apparent, speed of a jet. Contrary to the VHE results, studies from Piner & Edwards mostly feature subluminal or only slightly superluminal motion. This discrepancy of intrinsic and apparent velocities is known as the Doppler crisis or bulk Lorentz factor crisis. Single-zone jet models require unreasonably low inclination angles $\ll 1\,^\circ$ to explain this behaviour.

The purpose of this thesis is to perform an independent study with VLBI data of a chosen sample of TeV blazars to either confirm or deny the established results. The sample consists of PKS 1440−389, PKS 0447−439, PKS 2005−489, PKS 2155−304 and PKS 0625−354, which are nearly all TeV detected blazars of the TANAMI (Tracking Active galactic Nuclei with Austral Milliarcsecond Interferometry) sample and which are bright enough to be observed in the radio frequencies at 8.4 GHz. TANAMI is a multiwavelength program with VLBI at its core, focusing on AGN with a declination of $\delta < -30\,^\circ$. All of the jets investigated here feature either stationary, subluminal or only slightly superluminal motion, with PKS 2155−304 featuring the fastest component with $(7.8 \pm 2.5)c$, confirming the previous results by Piner & Edwards. Other properties, such as the inclination of PKS 0625−354 and jet-bending in 2155−304 as well as multi-zone jet models, which try to solve the Doppler crisis, are also discussed.

Contents

1. Active Galactic Nuclei

Active Galactic Nuclei (AGN) belong to the brightest and most interesting observable sources in the sky. While the main emission of "regular" galaxies stems from thermal stellar emission, galaxies containing AGN emit across the entire electromagnetic spectrum. They can even reach the highest of energies and as such are a likely candidate for high energetic neutrino emission as investigated in Kadler et al. (2016).

In order to achieve such luminosities, Shakura and Sunyaev (1973) showed that the accretion of surrounding material by a supermassive black hole in the center of the galaxy acting as a driving engine is the best model. The luminosity of AGN ranges from $10^{42}\,\frac{\mathrm{erg}}{\mathrm{s}}$ to $10^{48}\,\frac{\mathrm{erg}}{\mathrm{s}}$ with corresponding black hole masses of the order of $10^7 M_\odot$ to $10^{10} M_\odot$ as shown in studies such as Vestergaard and Peterson (2006) and Peterson et al. (2016).

Observations in different wavelengths provide various properties of AGN, ranging from kinematic results to emission lines, which lead to various classes with coinciding properties. Most of the general information about AGN can be found in books such as Krolik (1999), Robson (1996) and Schneider (2008), however only the aspects relevant for this thesis are provided below.

The important AGN classes for this thesis are Blazars, more particularly BL Lac objects, and to an extent Radio Galaxies. This chapter will provide general information about these two AGN types and the underlying emission processes as well as kinematic properties.

1.1. Classification of AGN

A first rough classification is provided by Kellermann et al. (1989), which divides AGN based on their radio emission. Depending on the ratio $R_{\mathrm{r-o}}$ of their optical and radio flux densities S_{o} and S_{r}, they are divided into *radio-loud* and *radio-quiet* sources

$$R_{\mathrm{r-o}} = \frac{S_r}{S_o} = \begin{cases} \geq 10, & \text{radio-loud} \\ 0.1 < R_{\mathrm{r-o}} < 10, & \text{radio-quiet} \end{cases} \tag{1.1.1}$$

In general radio-loud objects are accompanied by two highly relativistic streams of charged particles , which are referred to as jets, and as such show extended emission. They propagate perpendicular to the plane of the accretion disk, where one jet is located opposite to the other. It is assumed that radio-quiet objects do not possess such relativistic jets. However, there are suggestions that some of these sources either pro-

duce a highly collimated, powerful, relativistic jet or a subrelativistic, uncollimated wind (Stocke et al. 1992).

In this thesis the focus will be on radio-loud objects, while radio-quiet ones will be mentioned in Sect. 1.2 for completion.

1.1.1. Blazars

For most types of AGN, a host galaxy can be determined by means of observations. Since Blazars are among the brightest AGN, they outshine their host galaxy so none can be attributed in most cases. They are core-dominated, compact radio sources with a flat or inverted spectrum with emission going up to very high energy γ-rays. Blazars can be divided into Quasars (Quasi-stellar radio sources) and BL Lac objects, named after the prototypical source BL Lacertae. Quasars are characterized by the emission lines in the optical spectrum. They can be subdivided into optically violently variable (OVV) quasars and flat-spectrum radio quasars (FSRQ), which differ by the dominance in the optical and radio regime respectively. They feature strong narrow or broad emission lines and strong short-term variability on timescales of down to hours (Foschini et al. 2011), depending on the wavelength. For this thesis, BL Lac objects are of special interest since four out of five sources in this sample are confirmed to be of the BL Lac type with one source's classification being ambiguous. While still showing strong variability in flux density and polarization on time-scales of down to minutes (Heidt and Wagner 1998), they feature no or only very weak emission lines, often making it difficult to determine their redshift.

Being radio-loud objects, blazars feature highly relativistic jets which are observable throughout the entire electromagnetic spectrum. Radio observations provide apparent superluminal motion of jets with speeds of up to $25c$ (Piner et al. 2006) for some of the sources and bulk Lorentz factors of up to 50 (Lister and MOJAVE Collaboration 2016). The superluminal motion does not disagree with general relativity since it is simply a projectional effect, which will be explained in Sect. 1.4.

Of particular interest is the spectral energy distribution (SED) of blazars, which is the bolometric luminosity function. It features a double hump structure with two peaks: One is located in the X-ray regime and the other at high energy γ-rays. Figure 1.1 shows the SED of the FR 1 radio galaxy Centaurus A, which features a double hump structure characteristic of BL Lacs despite its classification. The lower part of the SED is produced by synchrotron emission from electrons which are accelerated radially in a circular magnetic field, while the higher energy peak is created from low energy seed photons which are up-scattered by said electrons with the inverse Compton effect in leptonic models or from high energy photons emitted from pion decay in hadronic models. These emission processes will be discussed further in Sect. 1.3.

BL Lac objects and to an extent FSRQs show a trend between the luminosity and the location of the peak frequencies in the SED. Namely, more luminous objects feature lower frequency peaks than less luminous ones. This is because there is a balance between

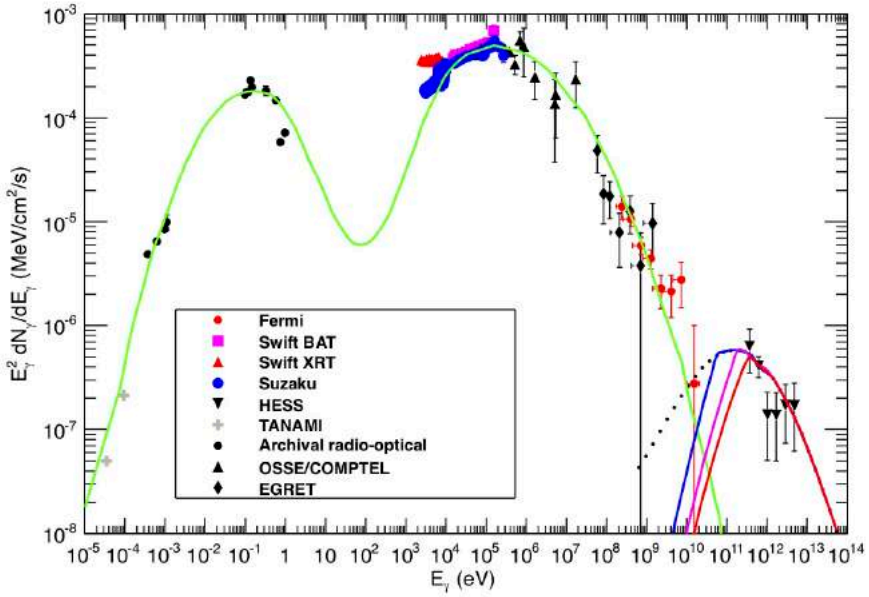

Figure 1.1.: Spectral energy distribution of the radio galaxy Centaurus A, which interestingly features a very BL Lac-like SED. The data obtained from several observations are fitted with synchrotron emission for the lower peak and inverse Compton for the higher one. However, the TeV photons need an additional model component. Image taken from Sahu, Zhang, and Fraija (2012).

radiative cooling of electrons and their acceleration (Ghisellini 1999). The process of radiative cooling is less efficient in less luminous objects, leading to the observed higher peak frequencies. This trend is known as the blazar sequence and is illustrated in Fig. 1.2.

Based on the position of the synchrotron peak frequency ν_{sp}, Padovani and Giommi (1995) introduced a further classification of BL Lac objects into low frequency peaked (LBL), intermediate frequency peaked (IBL) and high frequency peaked BL Lacs (HBL). This was extended in Abdo et al. (2010b) to all Blazars. According to this classification, low synchrotron peaked blazars (LSP), are those with $\nu_{\mathrm{sp}} < 10^{14}\,\mathrm{Hz}$, high synchrotron peaked (HSB) those with $\nu_{\mathrm{sp}} > 10^{15}\,\mathrm{Hz}$ and intermediate synchrotron peaked (ISB) those in between. HBLs are the focus of this thesis, since four out of five sources are classified as this type of blazar. According to the blazar sequence, HBLs are less luminous than LBLs. Additionally, HBLs are less variable than the other subclasses of BL Lacs. HBLs are mostly found in X-ray studies due to the location of their lower peak. This also means that they are more difficult to observe in radio frequencies due to their low luminosity in this regime. However, they also reach very high energies in the range of TeV.

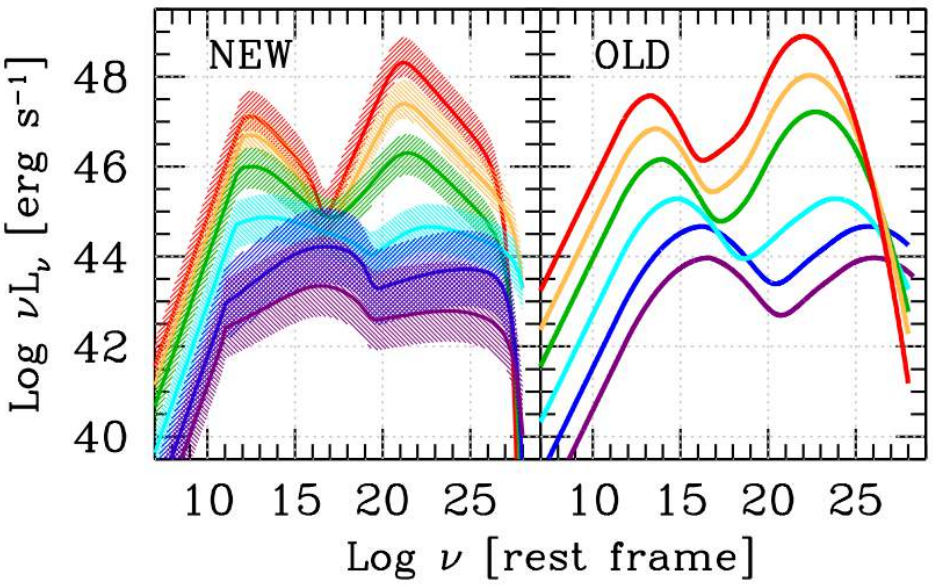

Figure 1.2.: Old (right) and new (left) blazar sequence by Ghisellini et al. 2017 for both BL Lac and FSRQs combined. Less luminous objects feature higher peak frequencies.

1.1.2. Radio Galaxies

Radio galaxies are radio-loud AGN which can be considered as the counterpart to the radio-quiet Seyfert Galaxies (Seyfert 1943). Accordingly, they feature both broad and narrow emission lines in their optical spectrum and can therefore be divided into Narrow Line and Broad Line Radio Galaxies (NLRG/BLRG). Being radio-loud these AGN are accompanied by powerful radio jets. This leads to a different approach to subdivide this group, which was introduced by Fanaroff and Riley (1974). This classification is a morphological one.

AGN of the class Fanaroff-Riley (FR) 1 show a luminous core with bright jets extending to both sides. They end in large radio plumes, which are less luminous than the main jet. Figure 1.3 shows an exemplary FR 1 galaxy, 3C 449, taken from a VLA observation at 1.4 GHz.

On the other hand, AGN of the type FR 2 are in total more luminous than FR 1 galaxies and feature a bright center, but weaker jets which end in bright lobes with dominating hot spots. Figure 1.4 shows a VLA map of an exemplary FR 2 quasar, 3C47, at 4.9 GHz. This source in particular only features one jet, but no jet in the opposite direction, i.e. the counter-jet. The luminosity of FR 2 type objects is restricted by $L(178\,\mathrm{MHz}) \gtrsim 2 \times 10^{25} h_{100}^{-2}\,\mathrm{W\,Hz^{-1}\,str^{-1}}$ (Kembhavi and Narlika 1999), although this boundary is not very sharp and dependent of the frequency and the spectral index. This leads to an overlap in luminosity between the two classes, especially at higher frequencies.

Figure 1.3.: VLA contour map of the FR 1 type AGN 3C449 at 1.4 GHz. It features a bright core and two bright jets ending in weaker radio plumes. Adapted from Perley, Willis, and Scott (1979).

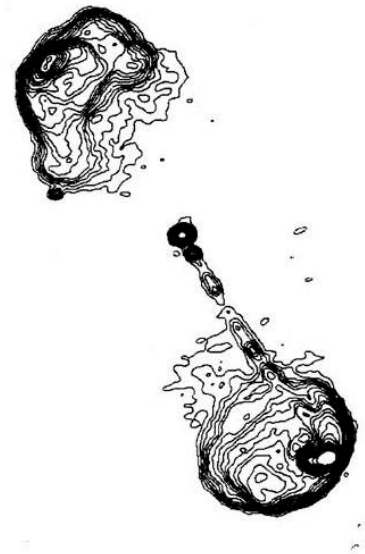

Figure 1.4.: VLA contour map of the FR 2 quasar 3C47 at 4.9 GHz. It features a bright core, one weak jet and two bright hot spots. Adapted from Bridle et al. (1994).

1.2. Model of Unification

Due to the many similarities as well as distinctions witnessed in all classes of AGN, it is reasonable to assume that these different types can be unified under one physically sound model. The unification scheme states that all types of AGN are only witnessed due to changes in two parameters, namely the (radio) luminosity and the inclination angle, i.e. the observation angle. The following section will summarize this model which can be found in further detail in Urry and Padovani (1995) and Antonucci (1993).

Figure 1.5 provides a sketch of the main statements of the unification model. The innermost region consists of a supermassive black hole surrounded by an accretion disk. The broad line emission region (BLR) is the accretion disk itself or rather very close to it. In order to understand the formation of the disk, it is useful to understand some of black hole physics first. The innermost stable circular orbit (ISCO) (or the radius of marginal stability) of an object gravitationally bound by a Kerr black hole with gravitational

radius $r_g = M$ (in natural units) is given by Camenzind (2007):

$$r_{\mathrm{ISCO}} = 2M \pm a + 2\sqrt{M^2 \pm aM}, \tag{1.2.1}$$

where a is the Kerr parameter which is a measurement for the spin of the black hole. Depending on the black hole spin, three different limiting values of r_{ISCO} arise:

$$r_{\mathrm{ISCO}} = \begin{cases} 6M & \text{for } a = 0 \\ M(1 + [4\delta]^{1/3}) & \text{for } a = M(1-\delta) \\ 9M & \text{for } a = -M \end{cases} \tag{1.2.2}$$

In this context, $a = 0$ is a non-spinning black hole, $a = M(1-\delta)$ is a hole spinning with the accretion disk, where δ is an infinitesimal displacement to prevent $r_{\mathrm{ISCO}} = M$, and $a = -M$ is a black hole spinning opposite to the accretion disk. In general, the binding energy of such an orbit is given by an expression dependent on the Kerr parameter a, $E_{\mathrm{bind}} = 1 - E(a)$. In the case $a \to M$ the binding energy is $E_{\mathrm{bind}} = 1 - 1/\sqrt{3} = 70\,\%$ of the rest mass (see Camenzind (2007)). In the process of accretion, half of this energy can be liberated as radiation from the disk around the black hole.

Furthermore, the model states that for a gravitational radius of $r_g \sim 10^{11}\,\mathrm{m} \approx 3.2 \times 10^{-6}\,\mathrm{pc}$ the hot accretion disk is located within a distance d of $r_g < d \leq 30 r_g$ or $d \sim 10^{-3}\,\mathrm{pc}$. The accretion disk itself is surrounded by a cold torus of dust, providing the material necessary to maintain the accretion. It is located at a distance of about $d \sim 1 - 10\,\mathrm{pc}$. In the radio-loud case, streams of highly energetic charged particles, the jets, are propagating out of the center perpendicular to the plane of the accretion disk. Along the direction of the jets close to the accretion disk, at a distance of about $d \sim 0.01 - 0.1\,\mathrm{pc}$ clouds responsible for broad emission lines can be found, building the broad line region (BLR). It consists of a dense ($n \sim 10^{10}\,\mathrm{cm}^{-3}$) and fast-rotating medium. Thus, due to the large velocity of the radiating particles, the effect of Doppler broadening is large for the emission lines witnessed from this region. Further outside at about $d \sim 100 - 1000\,\mathrm{pc}$ (see Fig. 1.5), the material becomes less dense ($n \sim 10^3 - 10^6\,\mathrm{cm}^{-3}$). Here, the emitting material is colder and the Doppler broadening is not as effective as in the BLR, only creating narrow emission lines. This region is hence called narrow line region (NLR).

The already established differentiation of radio-loud and radio-quiet AGN is directly governed by the parameter of luminosity, where radio-quiet galaxies are less luminous and do not feature a jet. If these types of galaxies are observed under a sufficently small inclination angle, both broad and narrow emission lines are visible, creating the class of Seyfert 1 galaxies. If the galaxy is observed almost edge-on to the plane of the accretion disk, the broad emission lines are obstructed by the dust torus, leaving only the narrow emission lines. These AGN are then classified as Seyfert 2 galaxies. More luminous objects are classified as QSO Type 1 and 2 correspondingly.

This classification can then be applied to the radio-loud AGN, where the corresponding class to Seyfert 1 are called broad line radio galaxies (BLRG), while narrow line radio

galaxies (NLRG) are the radio-loud counterpart to Seyfert 2 galaxies. Both these classes are morphologically classified by the Fanaroff Riley scheme. Finally, if the inclination angle is even lower, i.e. if the observer looks almost directly into the jet, the galaxy is of the blazar class, which is subdivided into quasars and BL Lac objects.

Since the only difference between radio galaxies and blazars is the inclination angle, it is apparent to assume that they are simply rotated counterparts to each other, where the drastical differences mainly stem from beaming effects present for blazars (see Sect. 1.3). If the FR scheme is taken into account, then Urry, Padovani, and Stickel (1991) argues that BL Lac objects are rotated FR 1 galaxies, while FSRQs correspond to FR 2 galaxies.

The different AGN types and properties mentioned in the context of this model are summarized in Table 1.1.

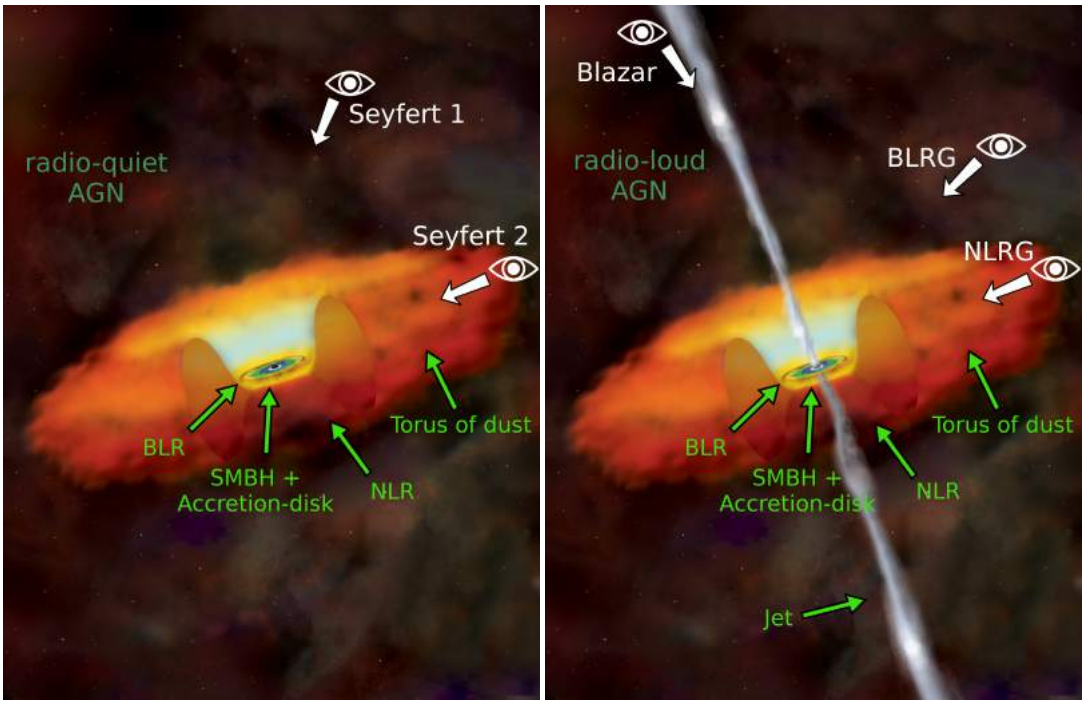

Figure 1.5.: Artist's impression containing all important components of the unified model: A supermassive black hole with an accretion disk in the center surrounded by a large dust torus. The narrow and broad line emission regions are indicated as well. The left image features a radio-quiet AGN due to the absence of a jet. Seyfert 1 galaxies are observed from a low inclination angle, while Seyfert 2 galaxies can be seen under a large angle, where broad emission lines are obstructed by the dust torus. The right image is that of a radio-loud AGN since it features a jet. Narrow and broad line radio galaxies are observed correspondingly to Seyfert 1 and 2 galaxies, while Blazars are seen under an even lower inclination angle, looking almost directly into the jet. Adapted from: NASA/CXC/M.Weiss

Table 1.1.: Overview of the unification model. Adapted from: Matthias Kadler

Type	RL[a]	Emission Lines	Luminosity	Jets	RM[b]
Seyfert 1	quiet	broad + narrow	low	no	none
Seyfert 2	quiet	narrow	low	no	none
QSO (Type 1)	quiet	broad + narrow	high	no	none
QSO (Type 2)	quiet	narrow	high	no	none
BLRG	loud	broad + narrow	low	yes	FR 1
	loud	broad + narrow	high	yes	FR 2
NLRG	loud	narrow	low	yes	FR 1
	loud	narrow	high	yes	FR 2
BL Lac	loud	none	low	yes	compact
FSRQ	loud	broad + narrow	high	yes	compact

Note: [(a)] Radio Loudness [(b)] Radio Morphology

1.3. Emission processes

As previously mentioned, the blazar SED features a double hump structure which can only be sufficiently modeled with two distinct emission processes. Namely, the synchrotron emission of accelerated electrons as well as high energy photons, which are up-scattered by the inverse Compton effect. In addition to that, jets in blazars are subject to relativistic beaming effects, since their relativistic motion is aligned almost directly to the observer. The following section aims at explaining these processes.

1.3.1. Synchrotron emission and beaming effects

The equations in this section are based on the derivations by Rybicki and Lightman (1979). This section acts as a summary and may not be given in the same detail as there.

To start out, the relativistic motion of a particle with charge q and mass m in a magnetic field $\mathbf{B}$ is governed by two differential equations:

$$\frac{\mathrm{d}}{\mathrm{d}t}(\gamma m \mathbf{v}) = \frac{q}{c}\mathbf{v} \times \mathbf{B} \tag{1.3.1}$$

$$\frac{\mathrm{d}}{\mathrm{d}t}(\gamma m c^2) = q\mathbf{v} \cdot \mathbf{E} = 0, \tag{1.3.2}$$

where $\gamma = (1 - v^2/c^2)^{-1/2}$ denotes the particle's Lorentz factor, $\mathbf{E}$ the electric field and $\mathbf{v}$ the particle velocity. The second equation implies that $\gamma = \text{const.}$ and $|\mathbf{v}| = \text{const.}$,

which means that the entire problem can be summarized to

$$m\gamma\frac{\mathrm{d}}{\mathrm{d}t}\mathbf{v} = \frac{q}{c}\mathbf{v}\times\mathbf{B}. \tag{1.3.3}$$

The velocity can be separated into a component parallel to the magnetic field $\mathbf{v}_\parallel$ and a component perpendicular to it $\mathbf{v}_\perp$, resulting in

$$\frac{\mathrm{d}}{\mathrm{d}t}\mathbf{v}_\parallel = 0, \quad \frac{\mathrm{d}}{\mathrm{d}t}\mathbf{v}_\perp = \frac{q}{\gamma mc}\mathbf{v}_\perp\times\mathbf{B}. \tag{1.3.4}$$

Since $|\mathbf{v}| = \text{const.}$, this means that $|\mathbf{v}_\perp| = \text{const.}$, as well as $\mathbf{v}_\parallel = \text{const.}$. The acceleration a is therefore perpendicular to the velocity at all times. On a projected plane perpendicular to the magnetic field the motion is circular. If $\mathbf{v}_\parallel \neq 0$, the resulting motion is helical around the magnetic field. Such a motion has a gyration frequency of $\omega_B = \frac{qB}{\gamma mc}$ and an acceleration of $a_\perp = \omega_B v_\perp$ and $a_\parallel = 0$. The total emitted radiation power is then given by

$$P = \frac{2q^2}{3c^3}\gamma^4(a_\perp^2 + \gamma^2 a_\parallel^2) = \frac{2q^2}{3c^3}\gamma^4\frac{q^2B^2}{\gamma^2m^2c^2}v_\perp^2 \tag{1.3.5}$$

$$= \frac{2}{3}r_0^2 c\beta_\perp^2\gamma^2B^2, \tag{1.3.6}$$

where $\beta_\perp = \frac{v_\perp}{c}$ and $r_0 = \frac{q^2}{mc^2}$ were used in the last step. β is simply the velocity in units of c and r_0 is the classical radius of a charged particle. In order to obtain an isotropic distribution of velocities, Eq. 1.3.5 needs to be averaged over all angles for a given speed β. If θ is the pitch angle, i.e. the angle between field and velocity, one obtains

$$\left\langle\beta_\perp^2\right\rangle = \frac{\beta^2}{4\pi}\int\sin^2(\theta)\mathrm{d}\Omega = \frac{2\beta^2}{3}, \tag{1.3.7}$$

and the resulting power is

$$\langle P\rangle = \frac{4}{9}r_0^2 c\beta^2\gamma^2B^2 \tag{1.3.8}$$

$$= \frac{4}{3}\sigma_T c\beta^2\gamma^2U_B \tag{1.3.9}$$

with the Thompson cross section $\sigma_T = 8\pi r_0^2/3$ and the magnetic energy density $U_B = B^2/8\pi$. The main contribution of synchrotron emission stems from electrons, since the σ_T scales with m^{-2} and the emission of particles with larger masses is negligible. The power spectrum of a single electron is given by

$$P_\nu = \frac{4}{3}\sigma_T c\beta^2\gamma^2U_B\phi_\nu(\gamma), \tag{1.3.10}$$

where $\phi_\nu(\gamma)$ is the spectral shape. In order to compute the expected power spectrum of a distribution of electrons, we consider a given electron energy density $n(\gamma)$, which scales as a power law with slope p in the case of non-thermal synchrotron emission as $n(\gamma)\mathrm{d}\gamma = n_0\gamma^{-p}\mathrm{d}\gamma$. The spectral shape is normed by $\int \phi_\nu(\gamma)\mathrm{d}\nu = 1$ and is well approximated by a Dirac δ distribution $\phi_\nu(\gamma) = \delta(\nu - \gamma^2 n u_L)$, where it is assumed that an electron of energy E only emits at a peak frequency of $\gamma^2\nu_L$ with ν_L being the Larmor frequency. The total power spectrum is then computed as a superposition of the power spectrum of each single electron weighted by their energy distribution $n(\gamma)$:

$$P_\nu = \int_1^\infty P_\nu(\gamma)n(\gamma)\mathrm{d}\gamma = \frac{4}{3}\sigma_T\beta^2\gamma^2 U_B n_0 \int_1^\infty \gamma^{2-p}\delta(\nu - \nu_L\gamma^2)\mathrm{d}\gamma \tag{1.3.11}$$

By substituting $\nu_L\gamma^2 = \nu' \Rightarrow$, leading to $\mathrm{d}\gamma = \frac{\mathrm{d}\nu'}{2\gamma\nu_L}$ and $\gamma = \left(\frac{\nu'}{\nu_L}\right)$, the integral simplifies to

$$P_\nu = \frac{4}{3}\sigma_T\beta^2\gamma^2 U_B n_0 \frac{1}{\nu_L}\int_{\nu_L}^\infty \left(\frac{\nu'}{\nu_L}\right)^{\frac{1-p}{2}} \delta(\nu - \nu')\mathrm{d}\nu' \tag{1.3.12}$$

$$= \frac{2}{3\nu_L}\sigma_T\beta^2\gamma^2 U_B n_0 \left(\frac{\nu}{\nu_L}\right)^{\frac{1-p}{2}}. \tag{1.3.13}$$

$\alpha = \frac{1-p}{2}$ is called the *spectral index* of this power spectrum. This means that the superposition of power-law distributed electrons with δ-peaked spectral shapes results in a power law spectrum. However, this statement only holds for a medium where the electrons are very unlikely to interact with the emitted synchrotron photons. This is the case, if the optical depth $\tau_\nu < 1$, which is defined as

$$\tau_\nu(s) = \int_{s_0}^s = \alpha_\nu(s')\mathrm{d}s', \tag{1.3.14}$$

with the absorption coefficient α_ν and the travel distance s through the medium. If $\tau_\nu < 1$, the medium is called optically thin, whereas it is referred to as optically thick or opaque for $\tau_\nu > 1$. Within the opaque region, the electrons undergo the process of synchrotron self absorption (SSA), which means that the electrons re-absorb the synchrotron photons emitted by them. The power spectrum is in this case scales with $P_\nu \propto \nu^{5/2}$ (see Rybicki and Lightman 1979), which is independent of the energy density power-law index p. SSA occurs only below a critical frequency, where $\tau_\nu = 1$, which is where a medium changes from being opaque to being optically thin. This turning point allows one to determine the size of an emission region, since $\tau \propto R$, where R is the size of the emitting region. The VLBI core is the innermost unresolved region and usually the $\tau_\nu = 1$-region.

Particularly in the case of blazars, where the observer is looking almost directly into the jet, the relativistic velocity causes the spectrum and flux density of the jet to be

Doppler boosted. The cause of this effect is that relativistic particles do not radiate spherically, but rather in a cone in the direction of their movement with an opening angle of γ^{-1}. The Doppler factor D, defined as the ratio between observed ν_{obs} and emitted frequency ν_{emit} can be computed as

$$D = \frac{\nu_{\mathrm{obs}}}{nu_{\mathrm{emit}}} = \frac{\sqrt{1-\beta^2}}{1-\beta\cos(\phi)} = \frac{1}{\gamma\,(1-\beta\cos(\phi))}, \tag{1.3.15}$$

where ϕ is the angle to the line of sight. In Rybicki and Lightman (1979) it is shown, that $S_\nu \nu^{-3}$ is invariant under Lorentz transformation, with the flux density S_ν. Therefore, the luminosity $L(\nu)$ for a jet with a power law spectrum $L(\nu) \propto \nu^\alpha$ the effect of boosting results in

$$L(\nu_{\mathrm{obs}}) = D^{3-\alpha} L(\nu_{\mathrm{emit}}). \tag{1.3.16}$$

In principle, the radiation is affected in two ways: Its luminosity is increased and the spectrum is shifted to higher frequencies. This is illustrated in Fig. 1.6, where the previously established dependencies are also marked. This is the case for a single emission region with a fixed turnover peak at $\tau_\nu = 0$. Generally a jet consists of several regions which emit synchrotron radiation, each with their own turnover frequency. When looking directly at a jet, all of these regions are superimposed during observation, leading to a flat spectrum. More extended emission on kpc scales is cooled and slowed down, resulting in optically thin, unbeamed low frequency emission and a steep spectrum (see Fig. 1.7)

Doppler boosting works in both ways, meaning that while the jet towards the obsever is boosted in luminosity, the counter-jet, going in the opposite direction, is de-boosted and less luminous. Using the ratio R of both of the jets' flux densities, one gains the equation

$$R = \frac{F_{\mathrm{jet}}}{F_{\mathrm{counter}}} = \left(\frac{1+\beta\cos(\phi)}{1-\beta\cos(\phi)}\right)^{i-\alpha}. \tag{1.3.17}$$

If only one component of the jet, i.e. one "radio blob", is observed, it is $i = 3$ and if the jet can be described as a series of components, it has to be $i = 2$ since the number of spherical emission components scales with the Doppler factor. The inclination angle ϕ can be determined if the flux density ratio and the jet speed are known. In many cases only the jet is visible, so no definitive flux density can be determined for the counter-jet. In such cases, the counter-jet flux density can be approximated by the noise level and at least a limit to ϕ can be computed.

1.3.2. High energy emission

While the low frequency emission is clearly described by the model of synchrotron emission, the high energy spectrum is not completely understood. There are two fundamentally different approaches to explain the high energy bump.

In purely leptonic models (see e.g. Blandford and Königl 1979, Königl 1981), the

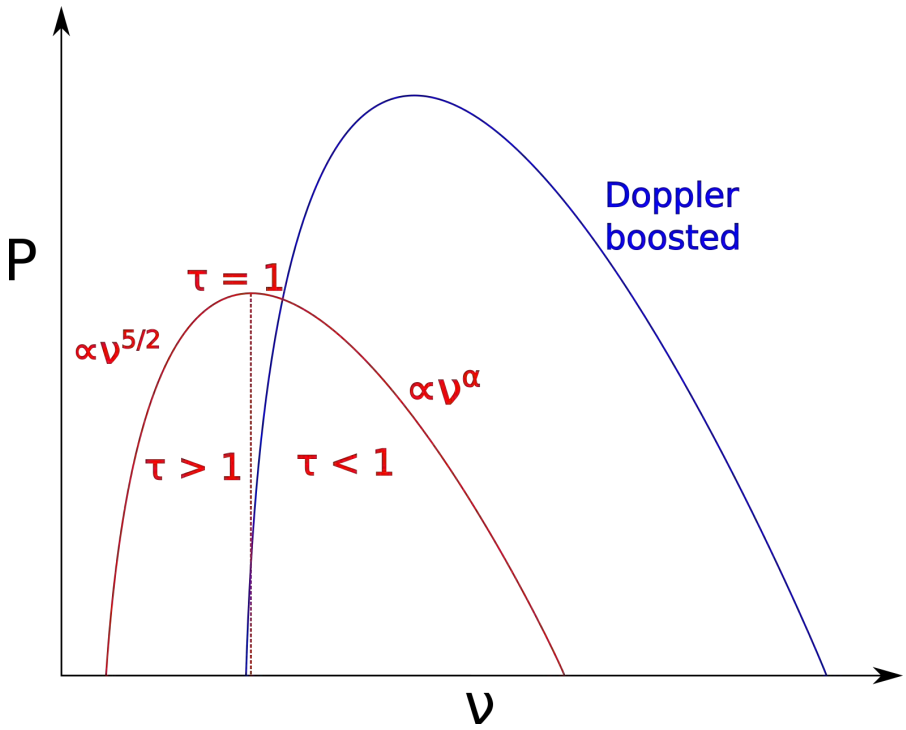

Figure 1.6.: Example plot of an unbeamed (red) and beamed (blue) synchrotron power spectrum of an electron distribution. The opaque section ($\tau_\nu > 1$) follows a $\propto \nu^{5/2}$ dependency due to synchrotron self absorption, while the optically thin ($\tau_\nu < 1$) region depends on $\propto \nu^{\alpha}$. Doppler boosting leads to an increase in power as well as a shift to higher frequencies.

key process to reach these energies is inverse Compton scattering. During this process, low energy seed photons are elevated to higher energies by inelastic scattering with ultrarelativistic electrons, leading to an energy loss for the electron and an energy gain for the photon, contrary to regular Compton scattering. There are two possibilities for the origin of these seed photons: If they originate from external sources, e.g. the other regions of the AGN like the accretion disk, the process is named External Compton, whereas it is called Synchrotron Self-Compton (SSC), if they stem from the synchrotron radiation responsible for the low-energy peak of the spectrum. Thermal comptonization is the process of electrons cooling down due to the energy transferred to the photons. This effect can lead to the Compton catastrophe, which is a rapid cooling process of the electrons, yielding limits to the temperature.

Hadronic models on the other hand (Mannheim 1993), while keeping the synchrotron model for the lower energy hump, assume a particle cascade of pion decay to be the source of the highly energetic photons. During such a cascade, very high energy neutrinos are also emitted. Recent campaigns, such as Kadler et al. (2016), are suggesting blazars to be likely candidates for VHE neutrinos detected by e.g. the Icecube detector (Aartsen,

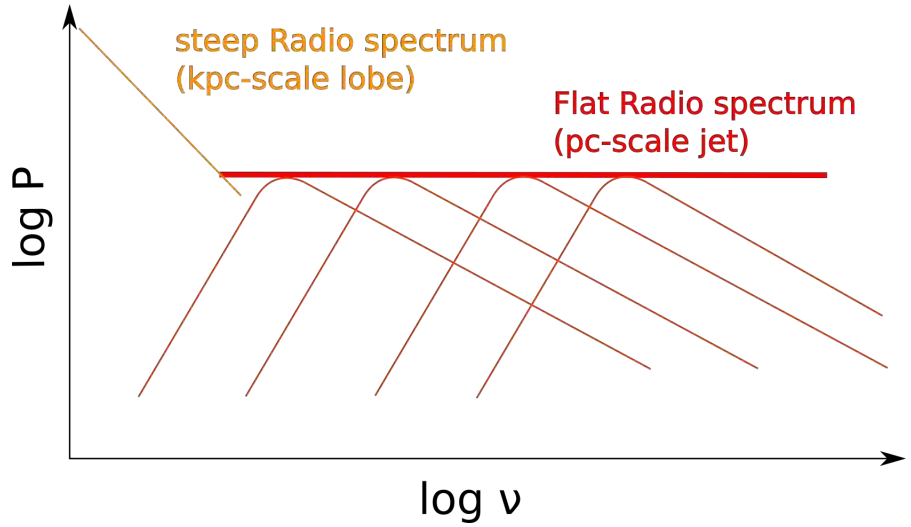

Figure 1.7.: Sketch of a logarithmically scaled radio power spectrum of a jet. Since there are several synchrotron emitting regions, the spectrum is a superposition of several beamed synchrotron spectra with different turnover frequencies, resulting in a flat spectrum of a pc-scaled jet. The lower frequency part is steeper due to unbeamed emission of a slowed-down kpc-scale lobe.

Abraham, and Ackermann 2016), supporting such hadronic models.

1.4. Apparent Superluminal motion of jets

As stated before, the apparent, i.e. projected, motion of AGN jets can, especially in the case of blazars, reach speeds several times higher than the speed of light c (Piner et al. 2006). This seems to contradict general relativistics at first, but can be easily explained by a projectional effect.

The motion of a moving component is illustrated in Fig. 1.8. The apparent speed v_{app} observed is simply given by

$$v_{\mathrm{app}} = \frac{\Delta x_{\mathrm{app}}}{\Delta t}, \tag{1.4.1}$$

with the apparent distance Δx_{app} and the observed travel time Δt.

At both times T_1 and T_2 and corresponding points x_1 and x_2 a signal is emitted by the component, but reaches the observer at times t_1 and t_2. The time it takes for the component to travel between x_1 and x_2 is given by $\Delta T = T_2 - T_1$. Due to the relativistic speeds, the travel distance of the emitted photons needs to be considered. The signal emitted at x_2 needs the time $t_{d'} = \frac{d'}{c}$ to reach the observer, while the signal at x_1 travels the longer amount of time $t_d + t'_d = \frac{d+d'}{c}$. This means, that the signals have the difference

$t_d = \frac{d}{c} = \frac{\Delta x_{\text{int}} \cos(\phi)}{c} = \frac{v_{\text{int}} \Delta T \cos(\phi)}{c}$ in travel time. The difference between both signals for the observer is simply $\Delta t = t_2 - t_1$. Plugging in the intrinsic information into the observer times results in

$$\left.\begin{aligned} t_1 &= T_1 + t_d + t_{d'} \\ t_2 &= T_2 + t_{d'} = T_1 + \Delta T + t_{d'} \end{aligned}\right\} \rightarrow \Delta t = t_2 - t_1 = \Delta T - t_d = \Delta T \left(1 - \frac{v_{\text{int}} \cos(\phi)}{c}\right). \tag{1.4.2}$$

The apparent distance Δx_{app} is related to the intrinsic distance Δx_{int} by the geometric relation

$$\Delta x_{\text{app}} = \Delta x_{\text{int}} \sin(\phi). \tag{1.4.3}$$

Inserting the equations 1.4.3 and 1.4.2 into Eq. 1.4.1 yields an equation independent of the observer values:

$$v_{\text{app}} = \frac{\Delta x_{\text{int}} \sin(\phi)}{\Delta T \left(1 - \frac{v_{\text{int}} \cos(\phi)}{c}\right)} = v_{\text{int}} \frac{\sin(\phi)}{1 - \beta_{\text{int}} \cos(\phi)}, \tag{1.4.4}$$

where $v_{\text{int}} = \frac{\Delta x_{\text{int}}}{\Delta T}$ and $\beta_{\text{int}} = \frac{v_{\text{int}}}{c}$ were used. Finally, expressing the apparent speed in units of c, we gain:

$$\beta_{\text{app}} = \frac{\beta_{\text{int}} \sin(\phi)}{1 - \beta_{\text{int}} \cos(\phi)} \quad \text{or} \quad \beta_{\text{int}} = \frac{\beta_{\text{app}}}{\beta_{\text{app}} \cos(\phi) + \sin(\phi)}. \tag{1.4.5}$$

Plotting β_{app} for different values of β_{int} shows, that for $\beta_{\text{int}} \rightarrow 1$, β_{app} quickly becomes larger than c at low angles ϕ, i.e. it shows superluminal motion. However, for very low values of ϕ, β_{app} decreases rapidly.

1.5. The Doppler Crisis

Of particular interest in AGN studies are sources emitting at the highest observable energies, namely the TeV-energies at 10^{12} eV. They are observed by ground-based telescopes, such as MAGIC, H.E.S.S. and VERITAS utilizing Cherenkov emission from particle cascades. Over 175 TeV-sources[1] have been cataloged so far, where over one third of them are extragalactic. 48 of these sources are classified as HBLs. They are, however, difficult to observe in the typical radio regime due to their extreme faintness, going down to a few tens of mJy. This section will summarize the most important studies in both the γ-rays and the radio regime based on the summary paper of Piner and Edwards (2016).

Some HBLs can display very bright flares in the γ-rays, like the source PKS 2155−304. Its flaring state during July 2006 obsereved by H.E.S.S: showed a flux density which was

[1] http://tevcat.unichicago.edu/

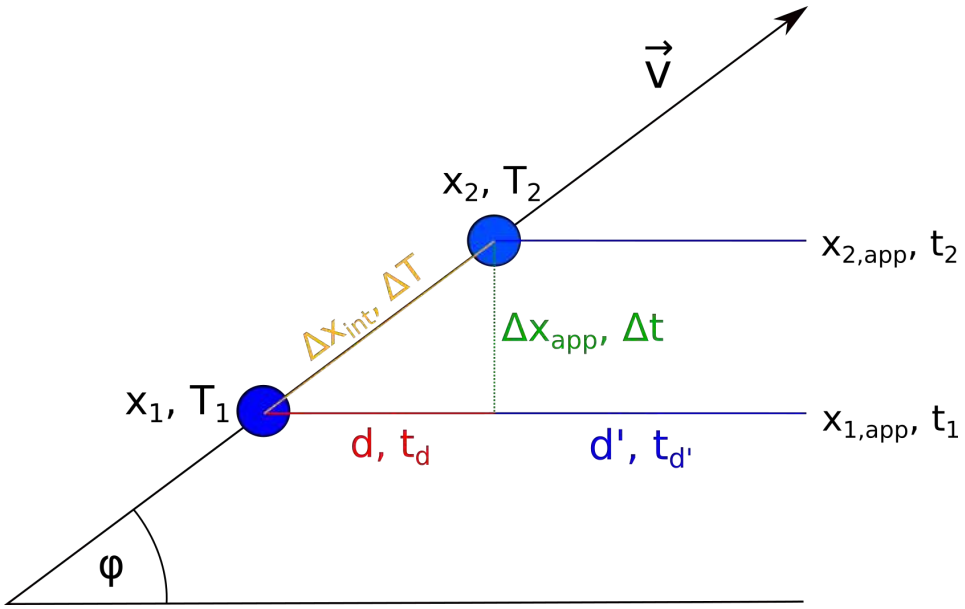

Figure 1.8.: Sketch of a jet component moving at relativistic speed towards the observer under the angle ϕ. Signals are emitted at positions $x_{1,2}$ and at times $T_{1,2}$ for the component. They reach the observer at later times $t_{1,2}$ due to the photon travel distance d and d' with corresponding times t_d and $t_{d'}$.

on average ten times higher than its typical values (Aharonian et al. 2007) and around 7 times as much as the Crab Nebula flux density (a standard candle in γ-ray astronomy). Additionally, it featured short-term variability of $\sim 600\,\mathrm{s}$. Earlier observations of flares of other sources are also present, such as 1ES 1959+650 (Krawczynski et al. 2004). While accompanying X-ray flares were also observed, the flux density in the radio frequencies stayed constant within their uncertainties. Other studies, such as Begelman, Fabian, and Rees (2008) and Ghisellini and Tavecchio (2008), investigate the rapid variability of such sources, in this case PKS 2155−304 and Mrk 401, where the flux density can change by a factor of 2 in only 3 - 5 minutes. They conclude that such short-term variability must stem from compact emission regions with an outflowing jet and are possibly caused by instabilities within the jet or dissipation at the base of the outflow. Furthermore, the bulk Lorentz factors in the jets must be $\gtrsim 50$, possibly up to 100.

Studies in the radio regime have been mainly done by Piner and Edwards for these kind of sources. Their works include several studies of the parsec-scale properties of both Mrk 501 (Giroletti et al. 2004, Edwards and Piner 2002) and Mrk 421 (Piner et al. 1999, Piner and Edwards 2005), which span over several epochs and different frequencies. All detected components appear to be either stationary or move at apparent subluminal speeds and no new components are detected. Both of these findings are in stark contrast to their highly variable and flaring activity in the TeV-range. Both feature limb-brightnened structures, which could be explained by velocity gradients starting at

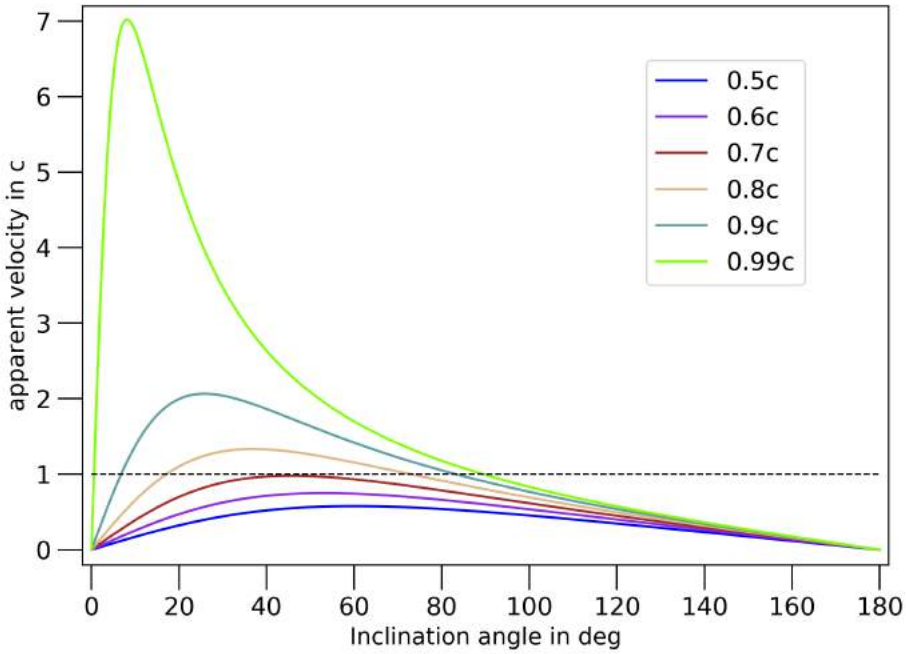

Figure 1.9.: Plotting the apparent velocity in c, β_{app}, against the inclination angle ϕ for different intrinsic values of β (see legend) shows, that for $\beta \to 1$ the apparent speed quickly rises above $1c$, indicated by the dotted line, for most values of ϕ, i.e. the motion seems superluminal. β_{app} has a maximum at low angles, but decreases rapidly for $\phi \to 0$.

the base of the jet. The limb-brightening in Mrk 501 (Piner et al. 2009) suggest an angle to the line of sight of $\sim 15\,^{\circ}$, while Mrk 421 has a very low angle of $\sim 1\,^{\circ}$ (Piner and Edwards 2005). Other sources also feature such slow moving jets as shown in Piner and Edwards (2004) and Piner, Pant, and Edwards (2008), where most of the components are stationary or subluminal, with only H1426+428 being at $\sim 2c$. More recent studies, such as Tiet, Piner, and Edwards (2012) and Piner and Edwards (2014), extend the amount of TeV sources with similar properties in VLBI data. Piner and Edwards (2016) provides a histogram, summarizing the peak apparent jet velocities derived in different samples. Figure 1.10 is a reproduction of the histogram presented there. Only two sources reach high apparent superluminal motion. Additionally, PKS 2155−304 features a high degree of jet-bending in the inner mas (Piner, Pant, and Edwards 2010), which established jet-bending as a common feature of TeV-blazars. All these sources possess modest brightness temperatures and apparent jet component motion that is sub-luminal or only slightly superluminal. This phenomenon is known as the "Doppler Crisis" (Tavecchio 2006) or "bulk Lorentz factor crisis" (Henri and Saugé 2006).

By combining the slow apparent speeds derived from VLBI data with the high Doppler

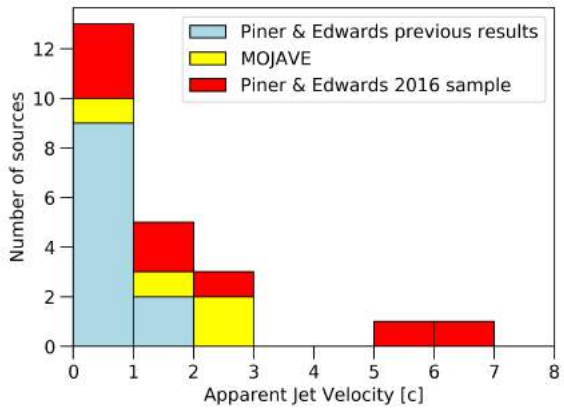

Figure 1.10.: Histogram of the peak apparent jet velocities prior to this thesis. Reproduced from Piner and Edwards (2016).

factors from TeV observations, the intrinsic Lorentz factors and inclination angles can be derived. This would result in unreasonably small viewing angles of $\phi << 1^\circ$ (Piner and Edwards 2016), which would imply tiny jet opening angles and huge linear sizes. By assuming larger inclination angles, the Lorentz and Doppler factors in the radio regime are more modest, contrary to the TeV data. However, the Doppler factor cannot be arbitrarily low since no counterjets have been detected in any of the TeV HBLs so far. The conclusion is that the radio emission and γ-rays cannot stem from the same emitting region, meaning that the previous one-zone jet models are no longer applicable here. There are several different models which try to expain the discrepancy between these emittion regimes. One of these models (Georganopoulos and Kazanas 2003) suggests a decelaration along the length of the jet. Here, the large Doppler factors $\delta \gtrsim 50$ needed to produce the high energy emission become obsolete. Instead, the model utilizes upstream Compton scattering. The upstream energetic electrons from the fast base of the flow see the synchrotron photons, which are produced in the slow part of the jet, as relativistically boosted and hence blueshifted, leading to the production of the TeV peak energies. Ghisellini, Tavecchio, and Chiaberge (2005) suggest a transverse velocity structure consisting of a fast moving inner structure, the spine, and a slow moving outer layer, the sheath. Here, one component sees the beamed radiation produced by the other, leading to an enhanced Compton emission of both regions. The slow component would, in this case, dominate the lower bump of the SED even with a smaller Lorentz factor. Evidence for such a structure is, for instance, the previously mentioned limb-brightening of a number of HBLs, such as Mrk 501 and 421. There are more models with different approaches, such as one, where the emission is caused by minijets from magnetic reconnection events (Giannios 2013), or one where the SED is modeled with multiple moving blobs (Tavecchio et al. 2011). Marscher (2014) proposes a single-zone model, in which the variations of flux density and polarization are rather caused by turbulences within the jet.

Since the work on radio data for TeV sources has been done by mainly one group, the motivation for this thesis is to perform an independent study with data from the

TANAMI (see Sect. 2.5) sample and investigate, whether slow moving radio jets can be detected here.

2. Radio Observations

Most sources in the sky appear as unresolved point sources if they are observed by conventional single-dish telescopes. If one wants to study, for instance, the origins of jets or more precisely kinematic parameters, much higher resolutions are necessary. The smallest resolvable angle θ, i.e. its angular resolution, of a lens with aperture diameter D at the wavelength λ is given by the Rayleigh criterion and translates to (see e.g. Born and Wolf 1999):

$$\theta \approx 1.22\frac{\lambda}{D}, \quad [\theta] = 1\,\mathrm{rad} \tag{2.0.1}$$

where the 1.22 is $\frac{x}{\pi}$ with $J_1(x) = 0$ and $J_1(x)$ being the order-one Bessel function of the first kind at x being its first zero. The factor is derived from the position of the first vanishing of the diffraction pattern. This translates well to the angular resolution of a telescope, where $\theta = \frac{\lambda}{D}$ is a good approximation with D being the telescope's diameter. As an example, let the diameter be $D = 100\,\mathrm{m}$, which is the diameter of the largest steerable telescope in Europe, the Effelsberg telescope. Assuming a wavelength of $\lambda = 3.5\,\mathrm{cm}$, approximately corresponding to $8.4\,\mathrm{GHz}$, a common radio observation wavelength, yields an angular resolution of $\theta \approx 1.2\,\mathrm{arcmin}$. This is not nearly enough to resolve the kpc-scale jets, where θ in the range of arcsec or less is required. For observations of pc-scale jets, even higher resolutions in the mas-scales are necessary. By combining several telescopes to an interferometer, these resolutions can be achieved. Very Long Baseline Interferometry (VLBI) utilizes an array of interferometers, each consisting of two telescopes, to achieve the desired mas-scale resolutions. In principle, the response of an interferometer to an extended source corresponds to determining a value of the Fourier transform of the source's brightness distribution. The simplest VLBI array consists of just two telescops, resulting in a two-element interferometer, which the next section will focus on before moving on to large arrays. The derivations shown here are mostly based on Burke and Graham-Smith (2010), but Thompson, Moran, and Swenson (2001) also provides good insight on this topic.

2.1. The Two-element interferometer

Figure 2.1 illustrates the basic geometry of a two-element interferometer. It consists of two telescopes with a certain distance, which is called the baseline b. To be more precise, the baseline vector $\mathbf{b}$ connects the phase center of the two antennas. The unit vector $\mathbf{s}$ is pointing at the radio source. The signal reaches one of the instruments with the

geometrical time delay $\tau_g = \mathbf{b}\cdot\mathbf{s}/c$, which may or may not be adjusted by an instrumental time delay τ_i, which is set to 0 for now. The two observed signals need to be processed using the cross-correlation $R_{xy}(\tau)$, which is just the time-averaged product of the two amplitudes $x(t)$ and $y(t)$ with delay τ: $R_{xy}(\tau) = \langle x(t)y(t-\tau)\rangle$ This product can be more conveniently derived by changing to frequency domain using its Fourier transform known as the cross-spectrum power density

$$S_{xy}(\nu) = X(\nu)Y^*(\nu), \tag{2.1.1}$$

where the convolution theorem for Fourier transforms has been used. This product will be proportional to the effective antenna area $A(\mathbf{s})$. For two monochromatic signals the Fourier transform will be two delta-peaks, one at frequency ν and one with a phase shift of $2\pi\nu\tau_g$. This results in

$$S_{xy}(\nu) = A(\mathbf{s})S\exp(i2\pi\nu\tau_g) = A(\mathbf{s})S\exp(i2\pi\mathbf{b}_\lambda\cdot\mathbf{s}), \tag{2.1.2}$$

with the source flux density S and the wavelength-dependent form of the baseline $\mathbf{b}_\lambda = \mathbf{b}/\lambda$.

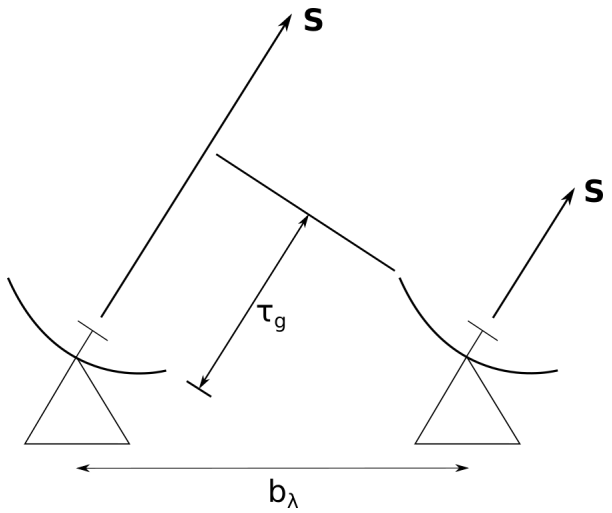

Figure 2.1.: Geometrical sketch of a two-element interferometer. One of the two telescopes has a geometrical time delay τ_g which may or may not be compensated by the instrumental delay τ_i. **S** marks the source direction and b_λ is the wavelength-dependent baseline.

Interferometers are systems with finite bandwidths $\mathcal{B}$, which has an effect on the cross-spectrum power density S_{xy}. The bandwidth is described by a square bandpass $G(\nu)$, which is centered over a certain center frequency ν_0 and becomes 0 beyond $\mathcal{B}/2$ in both directions. A good assumption is that the effective area and the flux density are constant

across the bandpass and by incorporating an instrumental delay τ_i, S_{xy} becomes

$$S_{xy}(\mathbf{s}) = A(\nu_0, \mathbf{s}) S(\nu_0) \operatorname{sinc}[\mathcal{B}(\tau_g - \tau_i)] \exp[-2\pi\nu_0(\tau_g - \tau_i)]. \tag{2.1.3}$$

The received signals generally feature an oscillatory shape with maxima and minima due to the interferometry. These oscillations are described by $\exp[-2\pi\nu_0(\tau_g - \tau_i)]$ and the signals are named fringes. The primary beam of a system provides information about its sensitivity and is filled out by the fringes for small bandwidths. For finite bandwidths however the fringe amplitudes are decreased by the narrower delay beam, as evident by $\operatorname{sinc}[\mathcal{B}(\tau_g - \tau_i)]$. The effects of the bandwidth can be summed up within the relative antenna area $\mathcal{A}(\sigma)$ as a modification of the effective area $A(\mathbf{s})$.

Up to this point, only the flux density of a point source was considered. Extended objects feature a brightness distribution $B_\nu(\mathbf{s})$, which then replaces the flux density $S(\nu)$. It is useful to define a phase tracking center s_0 with $\tau_g = \tau_i$, so every source direction can be given relative to this center with $\mathbf{s} = \mathbf{s_0} + \sigma$. Several approximations are now taken: The size of the source is assumed to be small compared to the response pattern of the delay beam, meaning that bandwidth effects can be neglected and $\nu = \nu_0$ is the defining frequency, provided that the width of the field of view $\theta \ll (\nu/\mathcal{B})(1/b_\lambda)$. The total output is then the cross-spectral density integrated over the entire radio source:

$$S_{xy}(\mathbf{s_0}) = \int \mathcal{A}(\sigma) B_\nu(\sigma) \exp i2\pi[\mathbf{b}_\lambda \cdot (\mathbf{s}_0 + \sigma) - \nu\tau_i] \mathrm{d}\Omega \tag{2.1.4}$$

An array of telescopes consists of several two-element interferometers with baselines $\mathbf{b}_{ij}$ if the i-th and j-th telescope. The complex visibility V_{ij} is then defined as

$$V_{ij} = S_{xy}(\mathbf{b}_{ij} \cdot \mathbf{s}_0) = \nu\tau_i, \tag{2.1.5}$$

finally leading to the fundamental equation for a practical interferometer:

$$V_{ij} = \int \mathcal{A}(\sigma) B_\nu(\sigma) \exp(i2\pi \mathbf{b}_{ij,\lambda} \cdot \sigma) \mathrm{d}\Omega \tag{2.1.6}$$

It is useful to switch to a coordinate system with a plane perpendicular to the source direction. These coordinates are conventionally labelled as (u, v, w), where $\mathbf{s}_0$ defines the direction of w and the (u, v)-plane is then parallel to the offset vector σ. The coordinates in Eq. 2.1.6 are expressed by the direction cosines of the unit vector $\mathbf{s}$, (l, m, n). Since $\mathbf{s}_0$ is perpendicular to the (u, v)-plane, we can set $w = 0$. The infinitisemal solid angle then becomes $\mathrm{d}\Omega = \frac{\mathrm{d}l\,\mathrm{d}m}{\sqrt{1-l^2-m^2}}$, resulting in the form

$$V_{ij} = \int_{4\pi} \mathcal{A}(l, m) B_\nu(l, m) \exp[i2\pi(ul + vm)] \frac{\mathrm{d}l\,\mathrm{d}m}{\sqrt{1 - l^2 - m^2}}. \tag{2.1.7}$$

Most of the time, the observed sources will be very small, so the offset angle σ will be

very small as well, meaning that x and y are parallel to u and v. In particular they are the spatial frequencies $u = \nu \cdot b\cos(\zeta)/c$ and $v = \nu \cdot b\sin(\zeta)/c$. The equation can then be rewritten by utilizing a small angle approximation:

$$V(u,v) \approx \int \mathcal{A}(x,y)B(x,y)\exp[i2\pi(ux+vy)]\mathrm{d}x\mathrm{d}y \tag{2.1.8}$$

Figure 2.2 illustrates the geometrical structure of the telescopes pointing at the source combined with the (u,v)-plane. The result implies that the complex visibility function received by the telescope antennas in (u,v)-domain is simply the Fourier transform of the source's brightness distribution in (x,y)-domain, modified by the relative antenna area $\mathcal{A}$. Hence, it is a convolution of the beam described by $\mathcal{A}$ and the intrinsic brightness distribution. However, a single measurement by one two-element interferometer amounts only to a particular value in the source's visibility function. By utilizing large arrays consisting of several interferometers, the (u,v)-plane can be sampled. The various techniques for large arrays and the necessary relations are the focus of the next section.

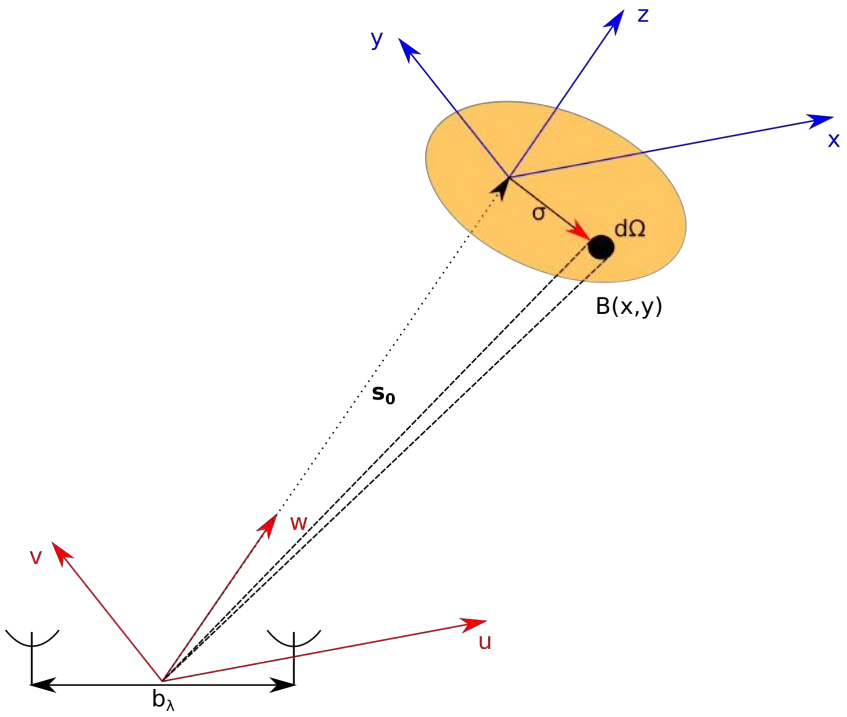

Figure 2.2.: Geometrical illustration of the (u,v)-plane and the interferometer. The interferometer with baseline b_λ is pointing at the fraction $\mathrm{d}\Omega$ of the brightness distribution $B(x,y)$ of a celestial source. Due to low angles, the direction cosines are approximated by x, y and z. Parallel to this coordinate system are the (u,v)-plane and w, which is parallel to the source phase center direction s_0. $\mathrm{d}\Omega$ is shifted by the amount σ from the center.

2.2. Interferometry with arrays

A signal is characterized by its amplitude and phase. Since the telescope responses are not perfect, they need corrections relative to each set of telescopes, which are provided by previous calibration steps. This leads to a lot of redundancy and a big data load. However, the problem can be solved by computing values which are independent of the telescope. These values are called the closure phase and amplitude and the equations to compute them are known as closure relations. The derivations presented here are based on Cornwell and Fomalont (1999) and Cornwell (1989). In order to gain the telescope independent closure phase, a set of at least three telescopes is required. The phase ϕ_{ij} between the i-th and j-th telescope possesses the errors δ_i and δ_j caused by electronic and atmospheric effects and can be written as

$$\phi_{ij} = \bar{\phi}_{ij} + \delta_i - \delta_j, \tag{2.2.1}$$

where $\bar{\phi}_{ij}$ is the true coherence phase between the two telescopes. For a set of three telescopes, looping over the full phase ϕ_{ijk} then results in

$$\begin{aligned} \phi_{ijk} &= \phi_{ij} + \phi_{jk} + \phi_{ki} && (2.2.2)\\ &= \bar{\phi}_{ij} + \delta_i - \delta_j + \bar{\phi}_{jk} + \delta_j - \delta_k + \bar{\phi}_{ki} + \delta_k - \delta_i && (2.2.3)\\ &= \bar{\phi}_{ij} + \bar{\phi}_{jk} + \bar{\phi}_{ki} = \bar{\phi}_{ijk}. && (2.2.4) \end{aligned}$$

This shows, that for a set of at least three telescopes, a closure phase can be computed, which is independent of the telescope specific errors δ_i. Similarly, the closure amplitude relation can be derived. For the closure amplitude, at least four different telescopes are required, leading to the closure relation

$$A_{ijkl} = \frac{|\bar{V}_{ij}||\bar{V}_{kl}|}{|\bar{V}_{ik}||\bar{V}_{jl}|}. \tag{2.2.5}$$

The fractions of recovered information of phase f_ϕ and amplitude f_A can be expressed dependent on the number of telescopes N and are given by $f_\phi = \frac{N-2}{N}$ and $f_A = \frac{N-3}{N-1}$.

As mentioned previously, the detector response corresponds to a certain value of the visibility function $V(u, v)$. Visualized on the (u, v)-plane, this value shows up as two points opposite to each other with a distance to the origin which is equal to the baseline. It is two points, since one two-element interferometer possesses two anti-parallel baseline vectors. In order to sample as many values of the visibility function as possible, large arrays consisting of several telescopes are used. The sampling of the visibility function is conventionally referred to as the (u, v)-coverage. Due to the rotation of the Earth, the orientation of the telescopes relative to the source changes with time, enabling them to sample different values of the (u, v)-plane with longer observations. This was first appropriately labeled as *Earth rotation synthesis*, but later shortened to *aperture synthesis*.

The synthesis effect is strongest on the two poles at a declination $\delta = \pm 90\,^\circ$, leading to circles on the (u, v)-plane, and weakest at the equator with $\delta = 0\,^\circ$. For values in between, the resulting coverage features ellipses. The effect is illustrated in Fig. 2.3 for different declinations.

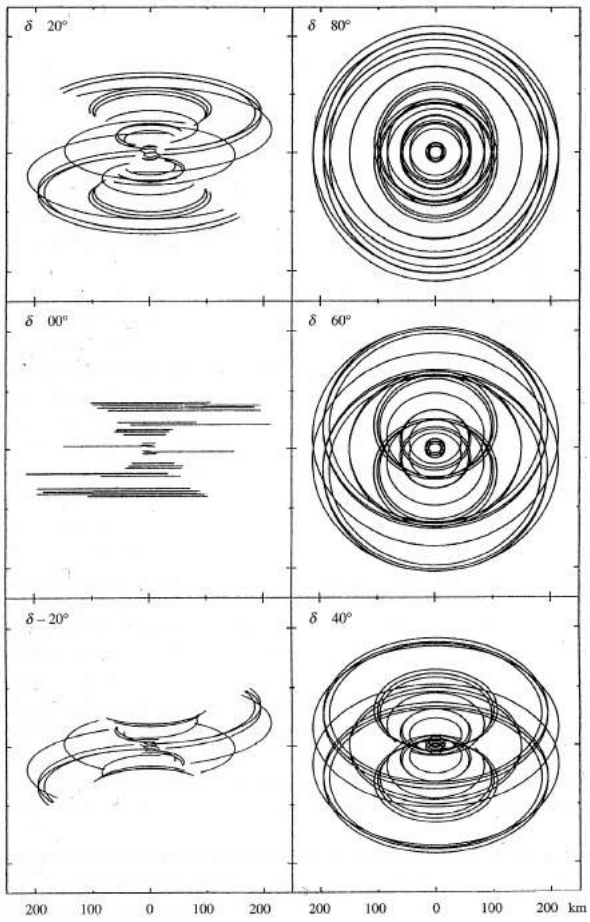

Figure 2.3.: (u, v)-coverage of the MERLIN interferometer at six different declinations for an 8-hour tracking observation. The coverage is more circular towards larger declinations. Taken from: Burke and Graham-Smith 2010

The array can only gather a limited amount of information from the (u, v)-plane, resulting in gaps within the coverage. The intrinsic brightness distribution $B(x, y)$ can be computed from the full complex visibility function $V(u, v)$ by means of inverse Fourier transform. Observations only deliver sampled information of the (u, v)-plane. This limited coverage is expressed by the spectral sensitivity function $W(u, v)$. In principle, it is the interferometers response to a two-dimensional point source $\delta(x, y)$, i.e. its Fourier transform. This pattern is also known as the synthesis beam or the dirty beam since prior to calibration and data reduction the response pattern contains many artifacts and influences outside of the primary beam, i.e. the *side lobes*. The measured visibility can

then be expressed as

$$V_{\text{measured}}(u,v) = w(u,v)W(u,v)V(u,v), \tag{2.2.6}$$

which, due to the convolution theorem, simply corresponds to the convolution of the brightness distribution with the intrinsic array parameters described by its relative antenna area. A weighting factor $w(u,v)$ can be added to address more compact or extended sources. This will be further discussed in the next section.

2.3. Deconvolution with CLEAN and Self-Calibration

In order to regain the intrinsic brightness distribution, the measured visibility needs to be inversely Fourier transformed as well as be deconvolved from the beam. Due to the gaps in information present in the (u,v)-coverage, algorithms utilizing interpolation are necessary. For this, Högbom (1974) developed the CLEAN algorithm, of which different variants were developed over the years. The procedures presented here are discussed in Cornwell, Braun, and Briggs (1999). The principle of the algorithm is to describe the brightness distribution by point sources, where the positions and strengths of these points are computed iteratively. The final image, known as the CLEAN image, is then a convolution of the sum of the point sources with the CLEAN beam, which is a Gaussian fit to the primary beam without the side lobes.

The original algorithm by Högbom (1974) can be summarized by these steps:

1. The position of the brightest peak in the dirty image needs to be found and its strength computed. This can be improved by specifying areas for the search using CLEAN windows.

2. At the position of the peak, the dirty beam B multiplied by the peak strength and the damping factor known as the loop gain $\gamma \leq 1$ is subtracted from the dirty image. The computed vales are saved.

3. Steps 1 and 2 are repeated until the remaining peaks are below a level specified by the user, leaving only the residuals in the dirty image.

4. The point source model gained from the previous steps is convolved with the previously described CLEAN beam.

5. Finally, the remaining residuals are added to the CLEAN image from 5.

Another algorithm is the one by Clark (1980), which is based on Fast Fourier Transform (FFT). It was developed since the CLEAN algorithm is essentially the deconvolution, so a 2D-FFT may perform the CLEAN more efficiently. Here, the approximate positions and strengths of the peaks are found by using only a small section of the dirty

beam. The procedure consists of a major and a minor cycle. The minor cycle goes as follows:

1. A section of the beam is chosen so that it contains the exterior side lobe with the highest intensity

2. All points of the dirty beam with an intensity higher than a fraction of the intensity of the determined exterior side lobe are selected.

3. Using the section of the beam and the selected points from the dirty image, the Högbom CLEAN algorithm is performed.

The major cycle starts by performing a FFT on the point source model from the minor cycle. It is then multiplied by the inverse transform of the beam, which is just the weighted sampling function. Finally, it is transformed back and subtracted from the dirty image. Subsequent minor cycles are performed to diminish any errors caused by the approximation of using only a section of the beam.

There are even more variations of the algorithms, such as the Cotton-Schwab algorithm described in Schwab (1984), but not all are listed here.

The absolute limits of mapping are determined by the system noise fluctuations. However, by only using CLEAN algorithms, the residual phase and amplitude errors are still the largest limiting factor. The process known as *self-calibration* helps to diminish these errors by utilizing the over-determined information given by the array. Each element within the array possesses a residual error in phase and amplitude. With N elements, where one telescope is chosen as a reference element, there are $2N-2$ error parameters and $N(N-1)$ observed quantities, meaning that the system is over-determined. The procedure by Schwab (1980) is a common approach to dealing with the over-determined system. In principle, the approach minimizes the sum of squares of residuals S by adjusting the element gains g_i and g_j and the model intensity distribution $\hat{I}$:

$$S = \sum_k \sum_{i,j} w_{ij}(t_k) \left| V_{ij}^{\mathrm{cal}} - g_i(t_k) g_j^*(t_k) V_{ij}^{\mathrm{mod}}(t_k) \right|^2 , \tag{2.3.1}$$

where V_{ij}^{cal} are the observed, calibrated visibilities and V_{ij}^{mod} are the model visibilities from an initial model obtained by a previous procedure. $w_{ij}(t_k)$ is a weighting function which can be chosen to favour baselines with good signal-to-noise ratios. Since it requires an initial model, selfcal cannot be used alone as a tool for imaging, but can only compute the phase errors of each telescope. There are procedures of selfcal which incorporate the closure relations shown in Sect. 2.2 in order to minimize the redundant information. The approach developed by Readhead and Wilkinson (1978) provides the following steps:

1. Obtain an initial model using a previously established method, in this case the CLEAN algorithm.

2. Estimate the true phases on two baselines for all independent closure phases using the model. The phases of the other baselines are derived in the loop from the observed closure phase.

3. Using the observed visibility amplitudes as well as the predicted visibility phases, a new CLEAN model has to be made.

4. Go to step 2, unless the model is sufficiently good.

The combination of both the CLEAN algorithm and the self-calibration is known as hybrid imaging.

2.4. Data analysis in DIFMAP

The two algorithms discussed previously are implemented in DIFMAP (Shepherd 1997), which was the program used to image the data provided for this thesis. Within DIFMAP, there are two essential forms of weighting, natural weighting and uniform weighting. In natural weighting, the weighting factor applied is inversely proportional to the noise variance of a visibility. This means that a constant weight to all visibilities is applied. Hence, natural weighting optimizes the point-source sensitivity and reduces noise. However, it sacrifices resolution since the resulting CLEAN beam and the sidelobe levels are rather poor. Instead, uniform weighting applies a weight which is proportional to the sampling density function, i.e. the number of visibilities. This method in return, offers a higher resolution and better sidelobe levels, but increases the noise level by up to a factor of 2 compared to natural weighting. Natural weighting was used for all images presented in this thesis.

DIFMAP is only used for the imaging process, whereas the necessary calibrations can be performed using AIPS (Astronomical Image Processing System, Greisen 2003). These calibratory steps were not performed in the course of this thesis, but rather externally prior to it.

The procedure of producing images in DIFMAP is as follows: First, the data are averaged using a time interval of 32 s, following the conventional approach of the MOJAVE program. By placing CLEAN windows and looping the dirty image with several CLEAN steps, each followed by a phase selfcal, the best possible model with the given amplitudes is found and bad data are flagged. Then, an amplitude selfcal across the entire observation time is performed and the correction factors for each telescope are noted. With this procedure, the noise level is reduced and more regions of the radio source can be identified. A new, more refined CLEAN model is formed and an amplitude selfcal with a time interval of 180 s is performed. The entire procedure is repeated with ever decreasing amplitude selfcal time intervals of $60, 20, 5, 1$ and 0 s to reach the lowest possible level of noise. Finally, a deep clean of the entire map is performed to receive the CLEAN image.

Up to this point, the source is only described by a point source model to gain a good image of its morphology. For kinematic analyses, several observations at different times, called *epochs* need to be taken. Within these contour images, different peaks of higher intensity can be spotted, so the jet can be described by a series of radio components. These components are modelfitted with elliptical Gaussians. The important modelfit parameters of these Gaussians are the positional coordinates relative to the core, the flux density, the full width at half maximum (FWHM) given by a major and minor axis as well as their position angle. Finally, it is useful to define the brightness temperature T_b, which is the assumed temperature of the component, if it were radiating thermally as a black body. It is given by Kovalev (2005) as

$$T_b = \frac{2\ln 2}{\pi k_B} \frac{S_c \lambda^2 (1+z)}{\theta_{\mathrm{maj}} \theta_{\mathrm{min}}}, \tag{2.4.1}$$

where S_c is the flux density of the component, $\theta_{\mathrm{maj/min}}$ its major and minor axis, λ the emission frequency, z the redshift and k_B the Boltzmann constant. The brightness temperature can provide a good limit for the physical soundness of a model component, since there are two limiting values. One limit is the inverse Compton limit of $10^{12}\,\mathrm{K}$ given by the Compton catastrophe of electron cooling mentioned in Sect. 1.3.2. The other limit is the equipartition value of $10^{11}\,\mathrm{K}$. The initial brightness temperatures of model components can be higher than these two limits due to boosting effects, however the intrinsic values need to be below.

During fitting it can occour that a component is unresolved along one axis, which is only possible for elliptical components, or in its entirety, i.e. the fit diverges to a point source. This leads to unreasonably high values of the brightness temperature. Kovalev (2005) provides a method to compute the lowest resolvable size θ_{lim} of a Gaussian component which is given by

$$\theta_{\mathrm{lim}} = b_\phi \sqrt{\frac{4\ln(2)}{\pi} \ln\left(\frac{\mathrm{SNR}}{\mathrm{SNR}-1}\right)}, \tag{2.4.2}$$

where b_ψ is the FWHM beam size measured along an abritrary osition angle ψ, SNR is the signal-to-noise ratio. It is given by $\mathrm{SNR} = \frac{S_{\mathrm{core}}}{\sigma_{\mathrm{core}}}$, where S_{core} is the fitted flux density of the core component and σ_{core} is the RMS measured in the region of the core. If the beam size is measured along the position angles corresponding to θ_{maj} and θ_{min}, upper limits to these parameters can be computed. Whenever the modeled axes are smaller then their lower limits, the component can be considered to be unresolved.

2.5. TANAMI

The *Tracking Active galactic Nuclei with Austral Milliarcsecond Interferometry* (TANAMI) program (see Kadler, Ojha, and TANAMI Collaboration 2015 and Ojha et al. 2010b) is a multiwavelength program observing and monitoring AGN below a declination of $-30\,^{\circ}$. The core program consists of VLBI observations examining the parsec-scale structures of mainly blazars and radio galaxies, but also other types of AGN. Additionally, it includes radio spectral and light-curve monitoring programs as well as higher-energy multiwavelength observations.

TANAMI investigates the connection between the parsec-scale properties of jets and their high energy $\gamma-ray$ emission and aims at understanding the emission and formation mechanisms of jets. The VLBI observations provide kinematic jet properties, such as the jet speed, inclination and opening angles and information about the morphology. TANAMI is able to observe at two radio frequencies, namely 8.4 GHz and 22 GHz, which enables the computation of spatial spectral index distributions. These results can then be combined with simultaneous broadband observations to answer some key questions about AGN. These questions include establishing a connection between high energy flares and the ejection of new radio components of a jet, locating the regions, where high energy photons are produced, what the jets of blazars and radio galaxies are made of and whether the γ-rays are beamed by the same Lorentz factors as the radio jets indicate with their apparent speed.

The VLBI observations are performed with the Australian Long Baseline Array (LBA) in combination with telescopes scattered across the Southern hemisphere. All telescopes of the array are listed in Tab. 2.1 and shown in Fig. 2.4. The longest baselines are achieved with transoceanic telescopes, such as Hartebeesthoek and O'Higgins. With this, resolutions of a few mas and below can be achieved. The only problem is the lack of real intermediate baselines, which can, however, be overcome with careful calibration during imaging (Ojha, Fey, and Charlot 2005).

The initial TANAMI sample (Ojha et al. 2010a) was defined as a hybrid sample of AGN south of $30\,^{\circ}$ consisting of a flux-density limited radio selected subsample and a γ-ray selected subsample of γ-ray sources detected by EGRET. The radio-selected subsample was selected to have a radio flux density of $S_{5\,\mathrm{GHz}} > 2\,\mathrm{Jy}$ and a flat radio spectrum ($\alpha > -0.5$) between 2.7 GHz and 5 GHz. The γ-ray subsample consists of all γ-ray blazars detected by EGRET, south of $-30\,^{\circ}$. The sample was then extended in Müller et al. (2017) to contain radio-loud sources with a correlated VLBI flux density of $\gtrsim 100\,\mathrm{mJy}$ combined with an association with significantly detected γ-ray sources. It now includes the 22 brightest γ-loud AGN from the third *Fermi*/LAT catalog (Ackermann 2015a). As of 2017, the TANAMI sample consists of 88 AGN, divided into 46 quasars, 16 BL Lacs, 17 radio galaxies and 9 unclassified AGN.

Table 2.1.: Telescopes belonging to the TANAMI array
(Adapted from Müller 2014)

Telescope	Diameter (meters)	Location
Parkes[a]	64	Parkes, New South Wales, Australia
ATCA[a]	5 × 22	Narrabri, New South Wales, Australia
Mopra[a]	22	Coonabarabran, New South Wales, Australia
Hobart[a]	26	Mt. Pleasant, Tasmania, Australia
Ceduna[a]	30	Ceduna, South Australia, Australia
Hartebeesthoek[b]	26	Hartebeesthoek, South Africa
DSS43[c]	70	Tidbinbilla, ACT, Australia
DSS45[c]	34	Tidbinbilla, ACT, Australia
O'Higgins[d]	9	O'Higgins, Antarctica
TIGO[d]	6	Concepcion, Chile
Warkworth	12	Aukland, New Zealand
Katherine	12	Nothern Territory, Australia
Yarragadee	12	Western Australia
ASKAP	36 × 12	Murchinson, Western Australia

Note: [(a)] Part of the LBA
[(b)] Unavailable between Sept. 2008 and Sept. 2010
[(c)] Operated by the Deep Space Network of the National Aeronautics and Space Administration.
[(d)] Operated by the Bundesamt für Kartographie und Geodsie (BKG)

Figure 2.4.: World view of the distributions of telescopes from the TANAMI array. The telescopes focused in Australia allow for a good coverage of short baselines. The transoceanic ones scattered across the Southern hemisphere provide data on long baselines. Credit: TANAMI/J. Wilms/M. Kadler

3. Determining the Velocities of TeV blazars from the TANAMI sample

The Doppler Crisis introduced in Sect. 1.5 is not fully understood yet, so any new data can infer new insights on the problem. Recent TANAMI VLBI data provide new information on previously not well known sources due to their Southern location as well as give new restrictions to jet velocities for well known sources. The first section of this chapter will introduce the sample, while the second and third sections show the morphology based on the images as well as explain how the Gaussian components are chosen to fit the jet before listing the results of the kinematic analysis in the fourth section.

3.1. Introduction of the Sample

The sample was chosen to contain all radio-loud AGN within the TANAMI sample, i.e. with a declination of $\delta < 30\,^\circ$, which are detectable with VLBI and listed as TeV sources in TeVCat[1]. This gives us a sample consisting of the HBLs PKS 1440−389, PKS 0447−439, PKS 2005−489, PKS 2155−304 and the FR 1 galaxies PKS 0625−354, although the classification is ambiguous in this case, and Centaurus A. Cen A is ultimately not included in the sample, since it was already thoroughly investigated in works such as Müller (2014), Abdo, Ackermann, and Ajello (2010a) and Müller et al. (2011). All other AGN sources south of 30 ° which are listed in TeVCat, but are not included in this sample, are not luminous enough in the radio frequencies to be sufficiently observable.

PKS 1440−389

PKS 1440−389 is classified as a BL Lac object with a position of RA = 14 h43 m57.2 s and $\delta = -39\,^\circ 08\,' 40\,''$. Its redshift was previously given by a tentative value of $z = 0.065454$ in Jones et al. (2009), but it is not included in the final release due to poor spectral quality. The best known constraint is given by $0.14 < z < 2.2$ (Shaw et al. 2013). The source is associated with the γ-ray source J1444.0-3907 of the third Fermi catalog (3FGL) (Ackermann, Ajello, and Atwood 2015b). It is listed there as a bright and steady extragalactic source with a hard spectrum and is therefore also included in

[1] http://tevcat.uchicago.edu/

the second Fermi Hard LAT sources catalog (Ackermann et al. 2016). According to Böck et al. (2016), PKS 1440−389 has a spectral index of 1.83 ± 0.08 in the range of $0.1 - 100\,\mathrm{GeV}$ with a flux density of $(2.3 \pm 0.5) \times 10^{-8}\,\mathrm{ph\,cm^{-2}\,s^{-1}}$. Its radio properties are listed as well with a radio core flux density at 8.4 GHz of $S_{\mathrm{core}} = (0.09 \pm 0.02)\,\mathrm{Jy}$ and a brightness temperature of $T_b = 8.8 \times 10^9\,\mathrm{K}$. The source was observed with H.E.S.S. between February and May 2012 and was confirmed to be a VHE emitter in Prokoph, Becherini, and Böttcher (2015) Its VHE spectrum shows a photon index of $\Gamma = 3.61 \pm 0.34$. The integral flux density above 220 GeV corresponds to 3 % of the Crab Nebula flux density. The excess flux density was fitted well with a single Gaussian, i.e. a point-like source and no variability in flux density was identified. Its SED is provided by Krauß et al. (2016) and was fitted well with two logarithmic parabolas and a blackbody spectrum where needed. It is shown in Fig. 3.1 and confirms the classification of the source as an HBL.

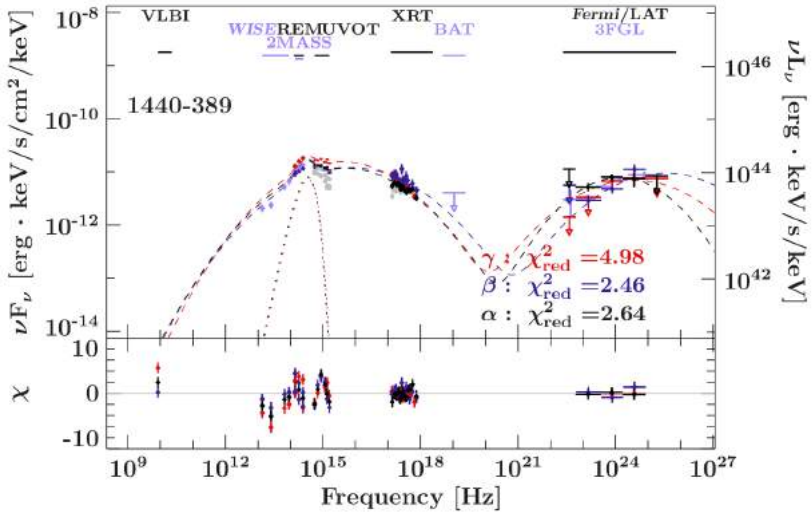

Figure 3.1.: Spectral energy distribution of the source PKS 1440−389. The SED was fitted with two logarithmic parabolas and a blackbody spectrum at the dotted lines. The color coding and greek letters correspond to datasets in the light curves with sufficient data coverage. Credit: Krauß et al. 2016

Its most recent light curve in the range of $0.1 - 300\,\mathrm{GeV}$ in the time frame of the current VLBI data are shown in Fig. 3.2 and shows no clearly isolated flares. Its radio structure is presented in Müller et al. (2017) as a first epoch VLBI image at 8.4 GHz and is shown in Fig. 3.3. Much like its VHE structure in the H.E.S.S. sky map, it appears to be mostly point-like with a slight extension to the south-west. Further south-west another, less luminous structure can be seen. However, with only three contour lines and a single epoch it can very well simply be an artifact. The total integrated flux density is $S_{\mathrm{total}} = 0.096\,\mathrm{Jy}$.

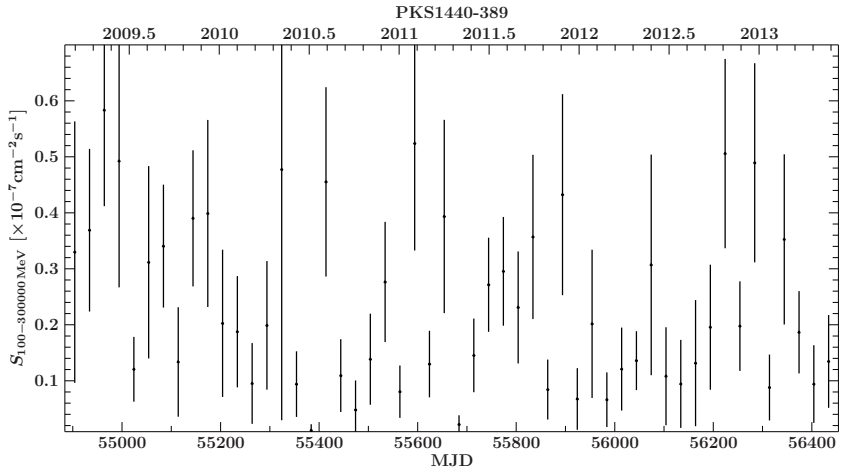

Figure 3.2.: Fermi light curve of PKS 1440−389 during the time of the current VLBI epochs in the energy range of $0.1 - 300$ GeV with a time binning of 30 d. No variability is seen during the observed time period. Credit: Michael Kreter

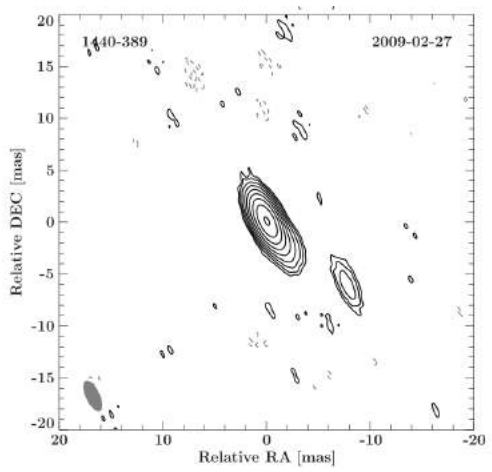

Figure 3.3.: First epoch image of the source PKS 1440−389 at 8.4 GHz from Müller et al. (2017). The black contours indicate the flux density level (dashed gray contours are negative), scaled logarithmically and separated by a factor of 2, with the lowest level set to the 3 σ noise level. The gray ellipse in the lower left corner is the size of the restoring beam.

PKS 0447−439

PKS 0447−439 is a BL Lac type object located at RA = 04 h49 m24 s and $\delta = -43\,°50\,'08\,''$ (Wierzcholska et al. 2015). The source is associated with the γ-source J0449.4-4350 in the 3FGL catalog and is one of the brightest hard-spectrum blazars in the Fermi catalog, leading to an inclusion in the 2FHL catalog. It was first misidentified as a Seyfert I galaxy by Craig and Fruscione (1997), but classified as a BL Lac in Perlman et al. (1998) and later as a HBL by Landt and Bignall (2008). Its basic γ-ray and radio properties are summarized in Böck et al. (2016), which yields a photon index of $\Gamma = 1.95 \pm 0.04$ with a flux density of $(9.7 \pm 0.7) \times 10^{-8}\,\mathrm{ph\,cm^{-2}\,s^{-1}}$ in the high energy range of $0.1 - 100$ GeV. Its radio core flux density at 8.4 GHz is given by $S_{\mathrm{core}} = (0.09 \pm 0.02)$ Jy with a brightness temperature of $T_b = 4.7 \times 10^{10}$ K. The VHE

energy emission of PKS 0447−439 was first discovered by H.E.S.S. during observations from December 2009 to January 2010 (Zech et al. 2011). It features very strong emission with a significance of 15.2σ, as shown in H.E.S.S. Collaboration et al. (2013). Its flux density above 250 GeV corresponds to $\sim 3\,\%$ of the Crab Nebula flux density above the same energy threshold and its spectrum is derived to be very soft with a photon index of $\Gamma = 3.89 \pm 0.37$ (with a systematic error of ± 0.22). This VHE detection triggered observations in the X-ray with the Swift and RXTE telescopes, which showed a flare in the hard X-ray band ($2 - 10\,\mathrm{keV}$) as well as rapid variability on nightly timescales as reported in H.E.S.S. Collaboration et al. (2013). The Fermi light curve, on the other hand, showed no clear flares during this time frame, but some variability with rising and decaying phases, which can also be seen in the recently produced light curve in Fig. 3.4.

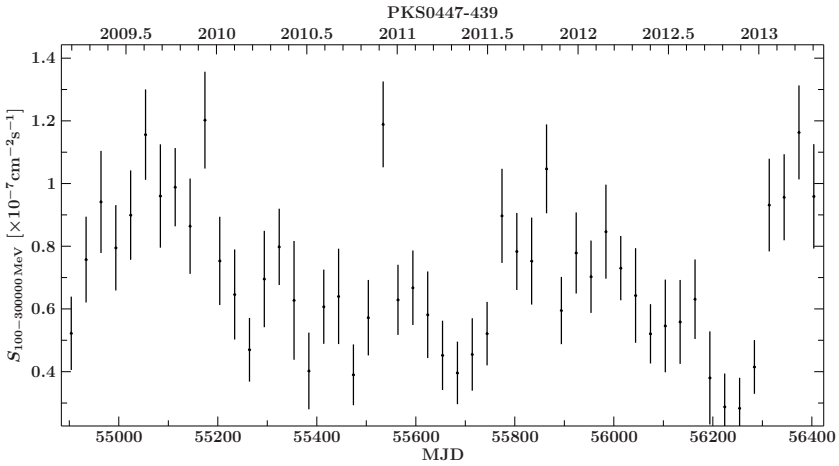

Figure 3.4.: Light curve of PKS 0447−439 in the energy range of $0.1 - 300\,\mathrm{GeV}$ during the time frame of the provided TANAMI VLBI data with a time binning of 30 d. During this time frame, the source shows no flares, but phases of rising and decaying flux density. Credit: Michael Kreter

With the multiwavelength data, the SED was fitted in there using a simple one-zone SSC model which is valid for $z \lesssim 0.4$. Additionally, an upper limit to the redshift of $z < 0.59$ is derived from the combined Fermi and H.E.S.S. data. Its most recent SED by Krauß et al. (2016), fitted with two logarithmic parabolas, is shown in Fig. 3.5 up to the high energy spectrum, which sets its synchrotron peak high enough to classify it as an HBL.

Müller et al. (2017) provides a first epoch TANAMI VLBI image of PKS 0447−439 at 8.4 GHz, with and without suppressing the longer baselines for higher sensitivity (taper). Both images are shown in Fig. 3.6. The source has a bright core with a total integrated flux density of $S_{\mathrm{total}} = 0.097\,\mathrm{Jy}$ (or 0.11 Jy for the tapered image) and an extension in the northwestern direction. A more prominent component is clearly visible close to the core at about 2.5 mas distance and fainter features of only two contours in roughly the same direction. These features are more prominent in the tapered image.

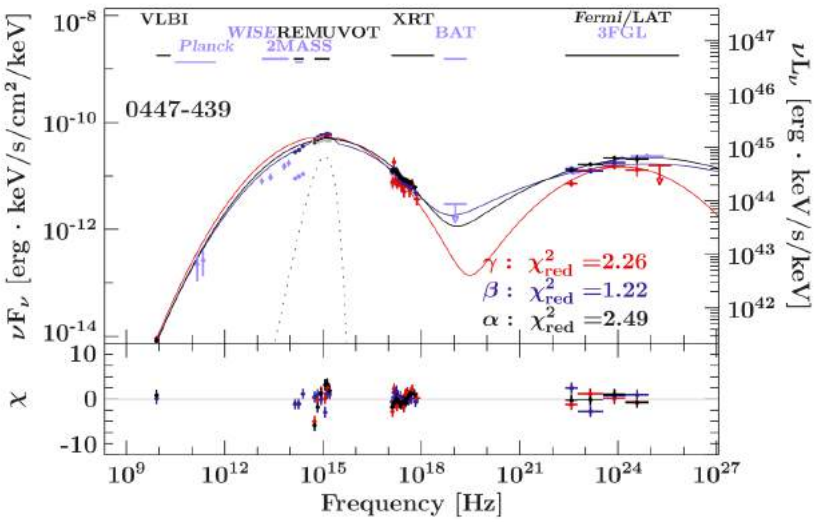

Figure 3.5.: Spectral energy distribution of the source PKS 0447−439. The SED was fitted with two logarithmic parabolas and a blackbody spectrum at the dotted lines. The color coding and greek letters correspond to datasets in the light curves with sufficient data coverage. Credit: Krauß et al. 2016

The source's redshift was first determined to be $z = 0.107$ in Craig and Fruscione (1997), but Perlman et al. (1998) find a value of $z = 0.205$ instead, where both values were widley used. Landt (2012) proposes a lower limit of $z \gtrsim 1.246$ from optical spectroscopy, which would contradict to both the previously known values and the current paradigm which states that VHE γ-rays cannot freely propagate for $z \gtrsim 1$ (Fumagalli et al. 2012). Rovero et al. (2013) could not reproduce the lower limit of 1.246 from further spectroscopy, reaching the conclusion that the observed emission line originated from the Earth's atmosphere, and Prandini, Bonnoli, and Tavecchio (2012) computed it from combined Fermi and H.E.S.S. data to be at $z = 0.20 \pm 0.05$. Finally, Landt and Bignall (2008) provide a lower limit of $z > 0.176$ based on a photometric method applied on a featureless spectrum. However, a recent study by Muriel et al. (2015) searched for a group of galaxies in the field of PKS 0447−439 in which it is likely to find the source's host galaxy. The resulting group has a redshift of $z = 0.343 \pm 0.002$ and the probability that the source galaxy of PKS 0447−439 is contained within is $\gtrsim 97\,\%$.

PKS 2005−489

PKS 2005−489 is a BL Lac object located at RA = 20 h09 m25 s and $\delta = -48\,°49\,'53\,''$ (Wierzcholska et al. 2015). Its redshift was determined in Falomo et al. (1987) to be $z = 0.071$ from optical emission lines. While it was during a faint state of the source, no further measurements deviating from this result were performed. The source has been investigated for a long time and was characterized as one of the brightest BL Lac objects

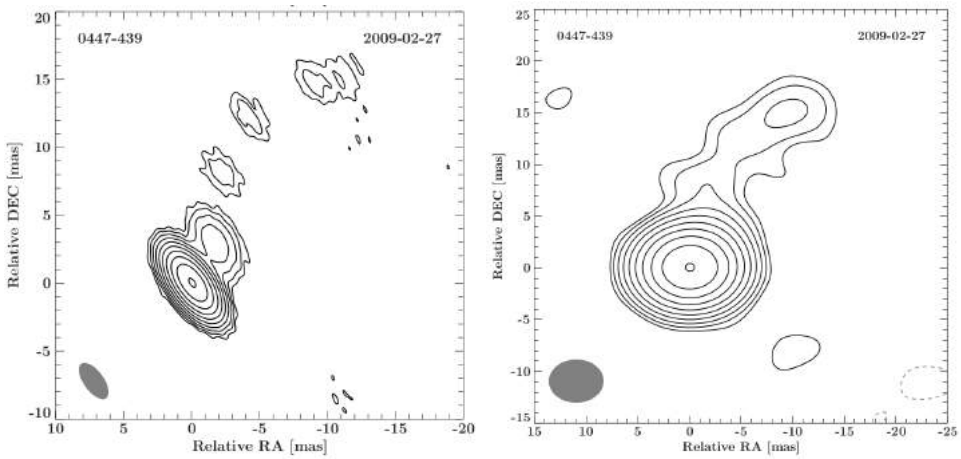

Figure 3.6.: First epoch images of PKS 0447−439 from Müller et al. (2017), with the untapered image on the left and the tapered one on the right. The black contours indicate the flux density level (dashed gray contours are negative), scaled logarithmically and separated by a factor of 2, with the lowest level set to the 3 σ noise level. The gray ellipse in the lower left corner is the size of the restoring beam.

in early observations due to the optical and UV brightness of the galaxy identified with PKS 2005−489 as well as its steep X-ray spectrum (Wall et al. 1986b, Wall et al. 1986a). Long-term variability was detected in all the mentioned spectra. Perlman et al. (1999) observed a very bright X-ray flare during a monitoring between October and December 1998. The source was 30 times brighter than during quiescence. They argue that this flare is likely due to particle injecction or in situ particle acceleration with synchrotron cooling causing a steepening of the spectrum. The synchrotron peak did not shift during this flare. Its synchrotron peak is located at either $\approx 10^{16}$ Hz (Sambruna et al. 1995) or, more precisely, between 10^{15} and 2.5×10^{16} Hz, as evident from the sources X-ray spectrum during an active state (Tagliaferri et al. 2001), classifying it as a HBL, which is also apparent in its most recent SED shown in Fig. 3.7. Sambruna et al. (1995) argues, that the observed variability of the source could be due to a variable electron energy and density. Optical observations show both short-term variability on timescales of minutes (Dominici, Abraham, and Galo 2006), where a scenario of shock wave production in the jet is proposed, as well as days (Dominici et al. 2004). Rector and Perlman (2003) argue that due to the correlation between X-ray and optical flares simple particle injection events are insufficient to explain the variability.

The source has been detected in the γ-rays with EGRET (Lin, Bertsch, and Bloom 1997) and is included in both the 3FGL and 2FHL catalogs as J2009.4-4849. Its high energy flux density in $0.1 - 100$ GeV is $(3.9 \pm 0.5) \times 10^{-8}\,\mathrm{ph\,cm^{-2}\,s^{-1}}$ with a photon index of 1.90 ± 0.07 (Böck et al. 2016). It was detected as one of the bright γ-ray sources in the first three months of operations of Fermi. The source was discovered to be an

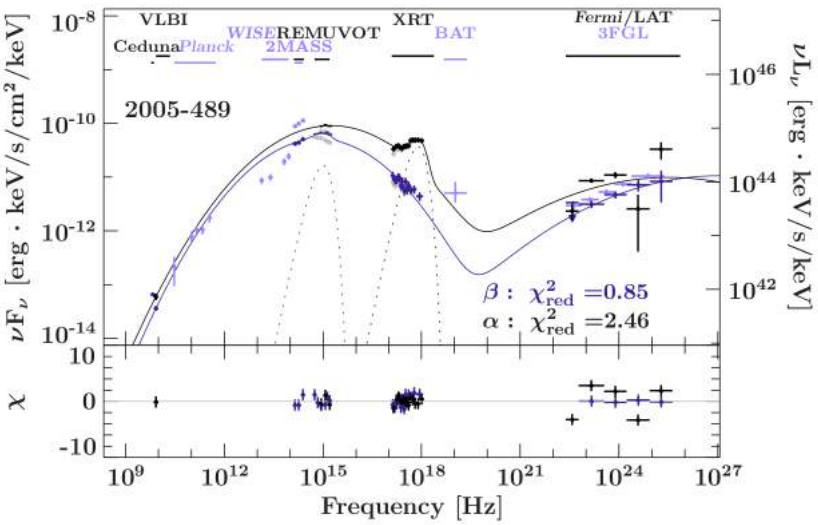

Figure 3.7.: Spectral energy distribution of the source PKS 2005−489. The SED was fitted with two logarithmic parabolas and a blackbody spectrum at the dotted lines. The color coding and greek letters correspond to datasets in the light curves with sufficient data coverage. Credit: Krauß et al. 2016

emitter of VHE photons by H.E.S.S. in Aharonian, Akhperjanian, and Aye (2005) and has a flux density above 200 GeV of $\sim 2.5\,\%$ of the Crab Nebula flux density as well as one of the softest energy spectrum with a power law photon index of $\Gamma = 4.0 \pm 0.4$. Monitoring campaigns (H.E.S.S. Collaboration et al. 2010a) as well as simultaneous multiwavelength campaigns (H.E.S.S. Collaboration et al. 2011, Costamante et al. 2008) feature no significant variability in the VHE regime, contrary to the flaring behaviour in the X-rays. The variability in the synchrotron regime and the lack of the same in the inverse Compton area does not justify the usage of a single-zone SSC model to fit the SED. Both Costamante et al. (2008) and H.E.S.S. Collaboration et al. (2010a) suggest the emergence of a new jet component which does not see the photons of the synchrotron peak and is responsible for the harder emission. Its lightcurve (see Fig. 3.8) in the range of $0.1 - 300$ GeV shows a repeating gradual increase and decrease in flux density over a timescale of about 2 years.

Its radio morphology was first investigated in Shen et al. (1998) and showed only a compact core. Ojha, Fey, and Charlot (2005) discovered a component at about 3 mas distance to the core in southwestern direction. Böck et al. (2016) provides a core flux density of (0.76 ± 0.12) Jy at 8.4 GHz with a corresponding brightness temperature of $T_b = 2.5 \times 10^{10}$ K. Ojha et al. (2010a) provides both tapered and untapered first-epoch VLBI images. The source extends further in the southwestern direction with a fainter jet than the previously discovered component with the faintest components being about 40 mas away from the core. According to these images, the jet features a large opening angle. The integrated flux density is $S_{\text{total}} = 0.65$ Jy, or 0.64 Jy for the tapered image.

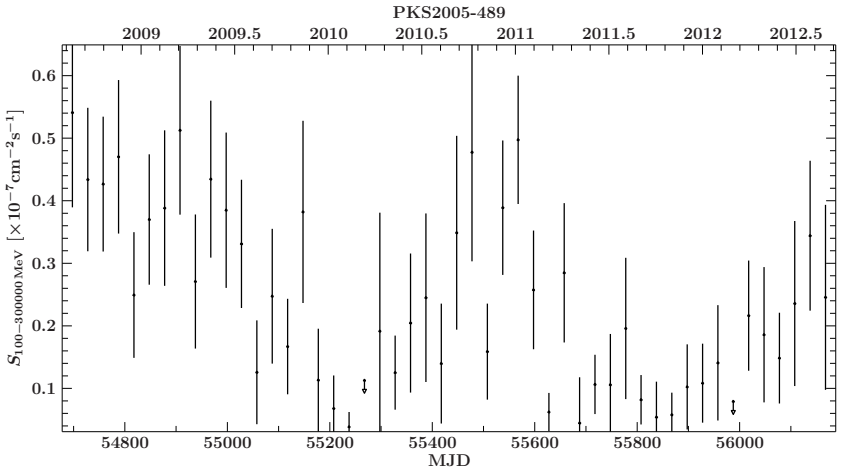

Figure 3.8.: Light curve of PKS 2005−489 in the energy range of 0.1 − 300 GeV during the time frame of the provided TANAMI VLBI data with a time binning of 30 d. The source shows signs of gradual increase and decrease of flux density on a time scale of about 2 years. Credit: Michael Kreter

PKS 2155−304

PKS 2155−304 is classified as a HBL (Giommi et al. 2005) with a position of RA = 21 h58 m52.1 s and $\delta = -30\,°13\,'32.1\,''$ (Zacharias et al. 1999) and a redshift of $z = 0.116$ as determined through absorption features in surrounding nebulosity by Falomo, Pesce, and Treves (1993). Brodie et al. (1983) state that the source is the brightest BL Lac object at that redshift and is one of the brightest extragalactic X-ray sources in the sky. Early studies on the source focussed mainly on its optical and X-ray properties, where short-term variability down to minutes was detected in both wavelengths (e.g. Tagliaferri et al. (1991) and Carini and Miller (1992)). Zhang et al. (2006) observe different timescales for different epochs of the source and argue that different modes of variability are operating on different timescales in the source. Zhang et al. (2002) provide four years of monitoring data and model the variability with a internal shock wave scenario within the jet.

PKS 2155−304 was first detected in the γ-rays with EGRET in Vestrand, Stacy, and Sreekumar (1995) in the 30 MeV to 10 GeV range with a hard spectrum. Today it is included in both the 3FGL and 2FHL catalogs as J2158.8-3013 and is one of the brightest γ-ray sources with a flux density in 0.1 − 100 GeV of $(21.4 \pm 0.8) \times 10^{-8}\,\mathrm{ph\,cm^{-2}\,s^{-1}}$ and a photon index of 1.92 ± 0.02 (Böck et al. 2016). Its Fermi light curve is shown in Fig. 3.10 in the energy range of 0.1 − 300 GeV and during the time of the VLBI epochs presented here. It shows some flux density variations with a peak in 2011, but constant, low flux density afterwards. It was detected in the VHE range for the first time by Chadwick et al. (1999), with evidence for correlation between the VHE and X-ray flux densities, however later observations during a low state found correlations

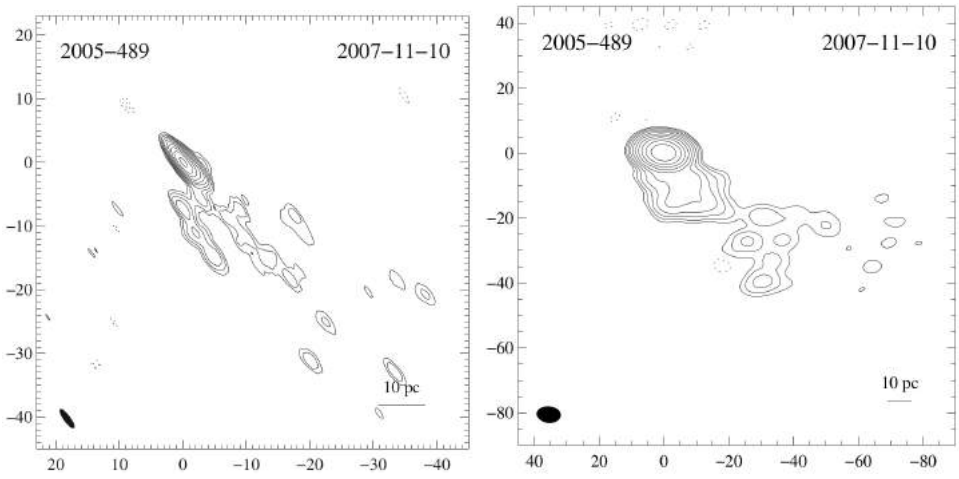

Figure 3.9.: First epoch images of PKS 2005−489 from Ojha et al. (2010a), with the untapered image on the left and the tapered one on the right. The black contours indicate the flux density level. The hatched ellipse in the lower left corner is the size of the restoring beam.

with the optical emission instead (Aharonian et al. 2009). It was detected by H.E.S.S. in Aharonian, Akhperjanian, and Aye (2005) at $> 160\,\mathrm{GeV}$ with variabilities on time scales of months, days and hours. It is the brightest VHE emitter in the sample with a flux density varying between 10 % and 60 % of the Crab Nebula flux density above 300 GeV with a steep photon index of $\Gamma = 3.32 \pm 0.06$. Aharonian et al. (2007) report on an exceptionally high flare of the source in 2006, reaching an average flux density of ~ 7 times of the Crab Nebula flux density. Further analysis of quiescent states and the flare show that low-level γ-ray emission could have a different origin than the outbursts (H.E.S.S. Collaboration et al. 2010b). The source shows rapid TeV flux density variability on timescales of $3 - 5\,\mathrm{min}$, which implies bulk Lorentz factors of ~ 50 (Ghisellini and Tavecchio 2008) and a similar relativistic Doppler factor. This would require very low viewing angles of $\lesssim 1\,^\circ$. Its SED up to GeV energies is shown in Fig. 3.11 with two log-parabolas, which was also done in H.E.S.S. Collaboration et al. (2017). They show that the 1-SSC model is not sufficient to explain the anticorrelation between the VHE and X-ray emission. Furthermore, they derive that the source should have a sharp break at $\approx 100\,\mathrm{GeV}$, suggesting the region responsible for the flares to be different from the quiescent emitting regions. The arc second radio structure of PKS 2155−304 taken with the VLA shows a bright core with two diffuse components to the east and west (Ulvestad, Johnston, and Weiler 1983). More recent low-frequency images taken with the GMRT (Pandey-Pommier et al. 2016) confirm this structure and identify the diffuse components as FR 1-like lobe structures to the east and west of the core with the western lobe being brighter. Contrary to the higher wavelengths, no variability was seen in their low-frequency radio observations. On the other hand, the parsec-scale structure

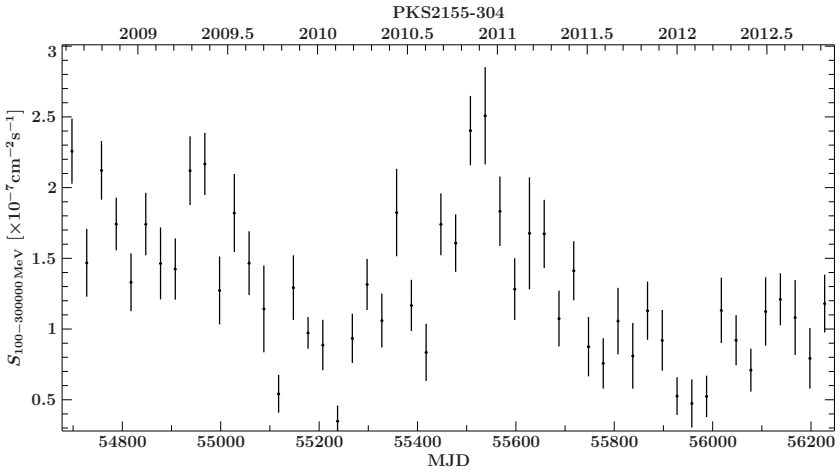

Figure 3.10.: Light curve of PKS 2155−304 in the energy range of $0.1 - 300$ GeV during the time frame of the provided TANAMI VLBI data with a time binning of 30 d. The flux density is variable until a peak in 2011, after which it lowers and stays at the same level. Credit: Michael Kreter

taken with the VLBA at 43 GHz (Piner and Edwards 2004) shows en extension with one component south east of the core at about 1.5 mas distance to the core. Piner, Pant, and Edwards (2008) measured the low apparent speed of the component to be $(0.93 \pm 0.31)c$. Piner, Pant, and Edwards (2010) were able to identify two more component closer to the core. They describe the morphology of the jet with a bending model, where the jet starts out southwest with a position angle of $-125\,°$, then quickly bends south to the core and finally approaches the 15 GHz position angle of $160\,°$, however the observed regions are quite diffuse. The first epoch image in Ojha et al. (2010a) at 8.4 GHz (see Fig. 3.12) shows a similar structure, but at a higher dynamical range, with a component at ~ 5 mas southeast of the core and a $\sim 15\sigma$ component at the same position angle as the inner one, with a total integrated flux density of 0.51 Jy. Böck et al. (2016) lists its radio core flux density to be $S_{\mathrm{core}} = (0.38 \pm 0.06)$ Jy with a brightness temperature of $T_b = 7.7 \times 10^{10}$ K.

PKS 0625−354

PKS 0625−354, often referred to as PKS 0625−35 (Kuehr et al. 1981), was first detected by Bolton, Clarke, and Ekers (1965) and later identified in the optical by Prestage and Peacock (1983) and is a bright extragalactic source at low radio frequencies (Wall and Peacock 1985). It is located at a position of RA = 06 h25 m20.23 s and $\delta = -35\,°27'21.8''$ (Prestage and Peacock 1983) and at a redshift of $z = 0.055$ (Jones et al. 2009). Its optical counterpart is located at the center of the Abell 3392 cluster and is a giant elliptical galaxy with a strong point source in its nucleus (Govoni et al. 2000).

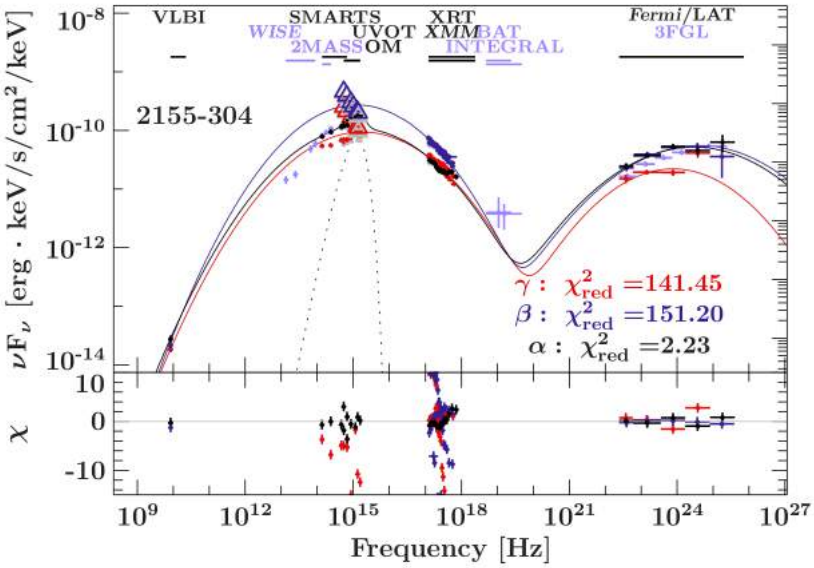

Figure 3.11.: Spectral energy distribution of the source PKS 2155−304. The SED was fitted with two logarithmic parabolas and a blackbody spectrum at the dotted lines. The color coding and greek letters correspond to datasets in the light curves with sufficient data coverage. Credit: Krauß et al. 2016

The source is often classified as a FR 1 radio galaxy due to its morphology, which features a core and distorted, diffuse lobes (Morganti, Killeen, and Tadhunter 1993). Early observations of its parsec-scale structure with the VLBA (Fomalont et al. 2000) feature a bright core with a faint jet component directly southeast of the core. Venturi et al. (2000) provide an image at 2.3 GHz which shows a more distant jet component located at about ~ 200 mas to the south east of the core. The first epoch TANAMI images from Ojha et al. (2010a) (tapered and untapered) feature a similar structure with a steady jet propagating to a length of ~ 95 mas away from the core (see Fig. 3.13). They list a total integrated flux density of $S_{\text{total}} = 0.36$ Jy for both images. Böck et al. (2016) provides a core flux density of $S_{\text{core}} = (0.35 \pm 0.06)$ Jy and a brightness temperature of $T_b = 1.2 \times 10^{11}$ K. However, the spectrum of the source suggests a classification as a BL Lac object instead, since Wills et al. (2004) can only fit the spectrum by using a power law. Additionally, non-thermal emission in the hard X-rays has been detected by Trussoni et al. (1999).

The source has been detected in the γ-rays first with EGRET in Fichtel et al. (1994) and is listed in the 3FGL and 2FHL catalogs as J0267.0-3529 and J0626.9-3528 respectively. Furthermore, the source shows small variability in the near-infrared and γ-rays (Nesci et al. 2013), favoring a classification as a BL Lac. Its Fermi light curve in the energy range of $0.1 - 300$ GeV presented in Fig. 3.14 shows no sign of flares and only low variability. Böck et al. (2016) lists its flux density as $(0.7 \pm 0.4) \times 10^{-8}$ ph cm^{-2} s^{-1} with a hard spectrum with a photon index of 1.86 ± 0.18 in the energy range of $0.1 - 100$ GeV.

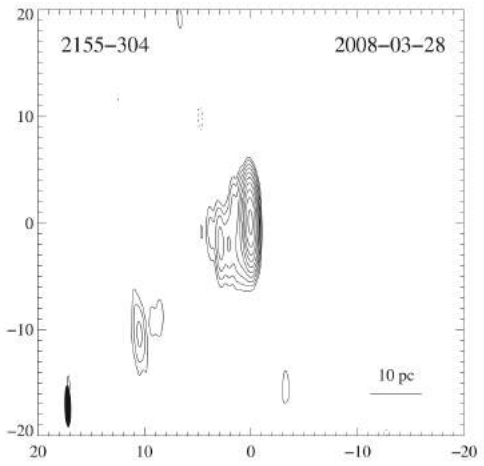

Figure 3.12.: First epoch image of the source PKS 2155−304 at 8.4 GHz from Müller et al. (2017). The black contours indicate the flux density level. The hatched ellipse in the lower left corner is the size of the restoring beam..

Finally, the source was detected with H.E.S.S. in the VHE range by Dyrda et al. (2015) with a significance of $\sim 6\sigma$ above an energy threshold of 250 GeV. The data are fitted well with a power law with a photon index of $\Gamma = 2.8 \pm 0.5$. The unified model predicts that BL Lac objects are simply FR 1 radio galaxies, which are boosted due to a low viewing angle. Bai and Lee (2001) suggests two subclasses of FR 1 radio galaxies, namely the HBL-like and LBL-like ones. PKS 0625−354 could very well be an object with an intermediate inclination angle, setting it somewhere between the classification as a BL Lac and a FR 1 radio galaxy.

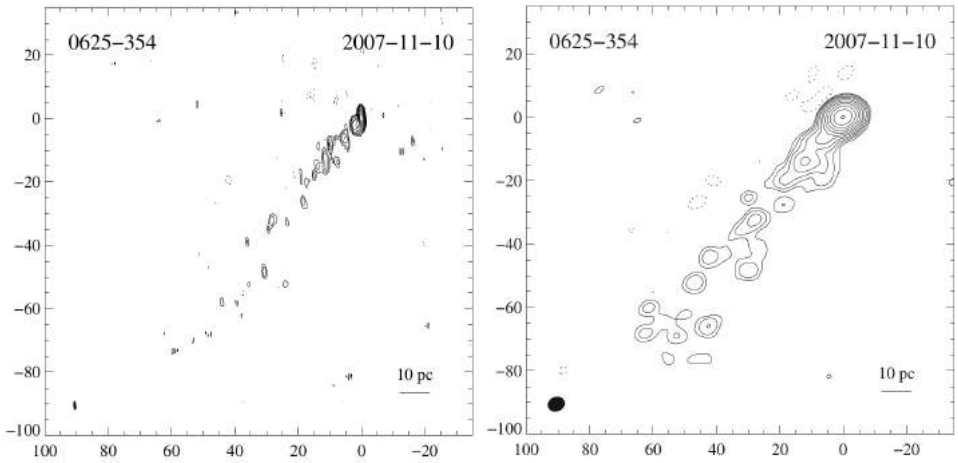

Figure 3.13.: First epoch images of PKS 0625−354 from Ojha et al. (2010a), with the untapered image on the left and the tapered one on the right. The black contours indicate the flux density level. The hatched ellipse in the lower left corner is the size of the restoring beam.

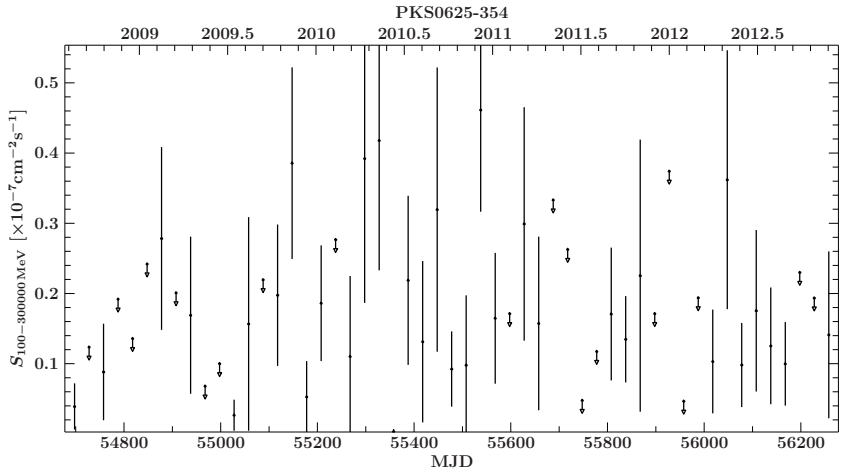

Figure 3.14.: Light curve of PKS 0625−354 in the energy range of $0.1 - 300$ GeV during the time frame of the provided TANAMI VLBI data with a time binning of 30 d. The source shows only low variability. Credit: Michael Kreter

3.2. Imaging and Morphology

This section will focus on showing the images obtained from the inverse Fourier transformation and deconvolution performed with DIFMAP on each of the five sources of the sample. All observations presented here have been performed at 8.4 GHz.

(u, v)-coverage and telescope configurations

Due to new telescopes being included in the TANAMI array, antennas sometimes being unusable due to various problems as well as differing observation schedules, the (u, v)-coverage varies from epoch to epoch. In order to get a basic idea of the data being dealt with, Fig. 3.15 compares a good (u, v)-coverage up to long baselines with one, where only short baselines are present. In Appendix A the (u, v)-coverages for every source in their most recent epoch are shown. Short baselines cover the inner part of the (u, v)-plane in every epoch in the range of $\sim 0-100\,\mathrm{M}\lambda$. Most of the epochs possess data from longer baselines, covering a range of $\sim 200-300\,\mathrm{M}\lambda$. Some epochs only have data from the shorter baselines, resulting in bigger beams and hence a smaller resolution. As is characteristic for TANAMI data, none of the epochs cover the intermediate baselines due to the lack of telescopes at these distances. The (u, v)-coverage improved with each successing epoch. The different telescope configurations for each observation epoch are listed in Tab. 3.1.

PKS 1440−389

Data of six TANAMI VLBI epochs from February 2009 to March 2013 have been analyzed for the source PKS 1440−389. All of the contour maps produced with DIFMAP are shown in Fig. 3.16 and additional information regarding the image parameters is listed in Tab. B.1.

The structure of the source appears to be very compact with a feature extending to the southwest at a distance of about ~ 2 mas to the core at a position angle of roughly $\sim -120\,°$. The first epoch image on 27 February, 2009 is not exactly the same as the one presented in Müller et al. (2017). The overall structure is the same, but the southeastern feature extends further to the south and the east, which can likely be attributed to differently placed windows during the cleaning. The original image shows a feature with three contour lines further southeast at roughly 13 mas distance to the core, which is not present in the image shown here. Instead, several two-contour-line features appear south and north of the source in this epoch and others appear at different positions in the remaining epochs. It is possible that these are simply artifacts created by noise and can be stressed in imaging through respective placement of windows. When imaging only one epoch, such features can be misinterpreted as real components of the jet, most prominently weak features of only two or three contour lines. However, the approach taken with multi-epoch-imaging is to compare the images at different epochs and only

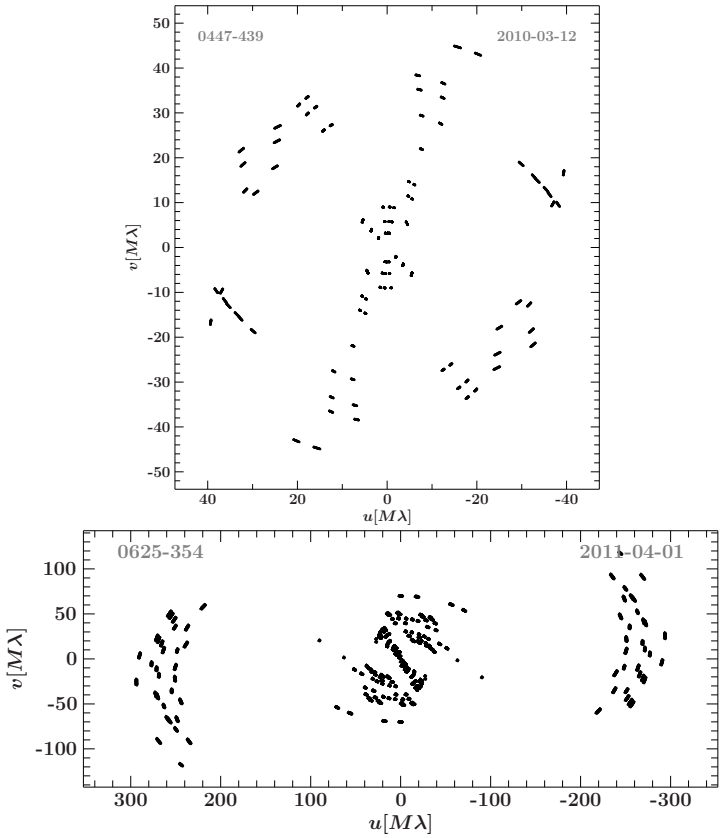

Figure 3.15.: Exemplary $(u-v)$-coverages of PKS 0447−439 (top) and PKS 0625−354 (bottom). The top image shows a small coverage, where only the short, inner baselines are present, whereas the bottom image features baselines of up to 300 Mλ.

keep components which appear in either several epochs or the epoch with the best data. So, while some epochs showed residual flux density further down southwest, but with differing peak positions, while other epochs showed no such residual flux density. To reach a definitive answer, data from future observations are needed.

Throughout the other epochs, the structure does not change significantly, with the feature always appearing southwest of the core at roughly the same distance. The source appears to have some extension directly south of the core in 27 April, 2012 in addition to the southwestern feature. It does not appear in the following observations and only slightly in the very first epoch, so it could be a result of the bigger beam combined with some badly placed windows. In 14 March, 2013 the source appears slightly more compact to the west and further extended to the south, possibly due to a smaller beam.

The total integrated flux density of this source ranges between values of 0.08 Jy to 0.11 Jy. The conventional error to the flux density is given by Ojha et al. (2010a) to be at $\sim 15-20\,\%$. Within these error margins, the flux density is constant, so all total integrated flux densities can be used to obtain an average value of $S_{\mathrm{tot,avg}} = (0.09 \pm 0.01)$ Jy,

Table 3.1.: Array configurations of the analyzed observations

Epoch	Participating Telescopes
2007 Nov. 10	CATW113, CD, HH, HO, MP, PA
2008 Feb. 07	CATW104, DSS43, HH, HO, MP, PA
2008 Mar. 28	CATW104, CD, DSS43, HH, HO, MP, PA
2008 June 09	CATW109, CD, HH, HO, MP, PA
2008 Aug. 09	CATW104, CD, DSS45, HH, HO, MP, PA
2008 Nov. 27	CATW104, CD, DSS43, HO, MP, PA, OH, TC
2009 Feb. 23	AT, CD, DSS34, DSS45, HO, MP, OH, PA, TC
2009 Feb. 27	AT, CD, DSS45, HO, MP, OH, PA, TC
2009 Sep. 06	AT, CD, DSS43, HO, MP, PA, TC
2009 Dec. 14	AT, CD, HO, MP, PA, TC
2010 Mar. 12	AT, CD, HO, MP, PA, DSS43
2010 May 08	AT, CD, DSS43, HO, MP, PA, TC
2010 July 24	AT, CD, HO, MP, PA, TC, TI
2010 Oct. 28	AT, CD, DSS34, DSS45, HH, HO, MP, OH, PA, TC
2011 Apr. 01	AT, CD, DSS43, HH, HO, MP, PA, TC, WW
2011 July 21	AT, CD, DSS34, DSS43, HH, HO, MP, PA, TC, WW
2011 Aug. 14	AT, CD, DSS43, HH, HO, KE, MP, PA, TC, YG
2011 Nov. 14	AT, CD, DSS34, DSS43, HH, HO, MP, PA, TC, WW
2012 Apr. 27	AK, AT, CD, HH, HO, MP, PA, TC, WW
2012 Sep. 15	AK, AT, CD, DSS43, HH, HO, KE, PA, TC
2012 Sep. 16	AK, AT, CD, DSS34, DSS45, HH, HO, KE, PA, TC
2013 Mar. 14	1: AK, AT, CD, DSS34, DSS43, HO, KE, PA, TC, WW
	2: AK, AT, CD, DSS43, HH, HO, KE, PA, WW

which is in agreement with the value listed in Müller et al. (2017).

PKS 0447−439

The data provided for PKS 0447−439 cover six epochs across the time frame from February 2009 to March 2013, meaning the data is from the same observations as for PKS 1440−389. The contour maps produced with DIFMAP are shown in Fig. 3.17 and image parameters are listed in Tab. B.2.

The source features a bright core with one or more components going off into north-western direction at a position angle of roughly $\sim -50\,^{\circ}$. The first peak, which is present in every epoch, starts out at a distance of ~ 2.5 mas northwest of the core in February 2009 and moves further away throughout the epochs up to a distance of ~ 3.6 mas in March 2013. A second, fainter feature further northwest appears in October 2010 at a distance of roughly ~ 7 mas to the core and is present in July 2011, but disappears

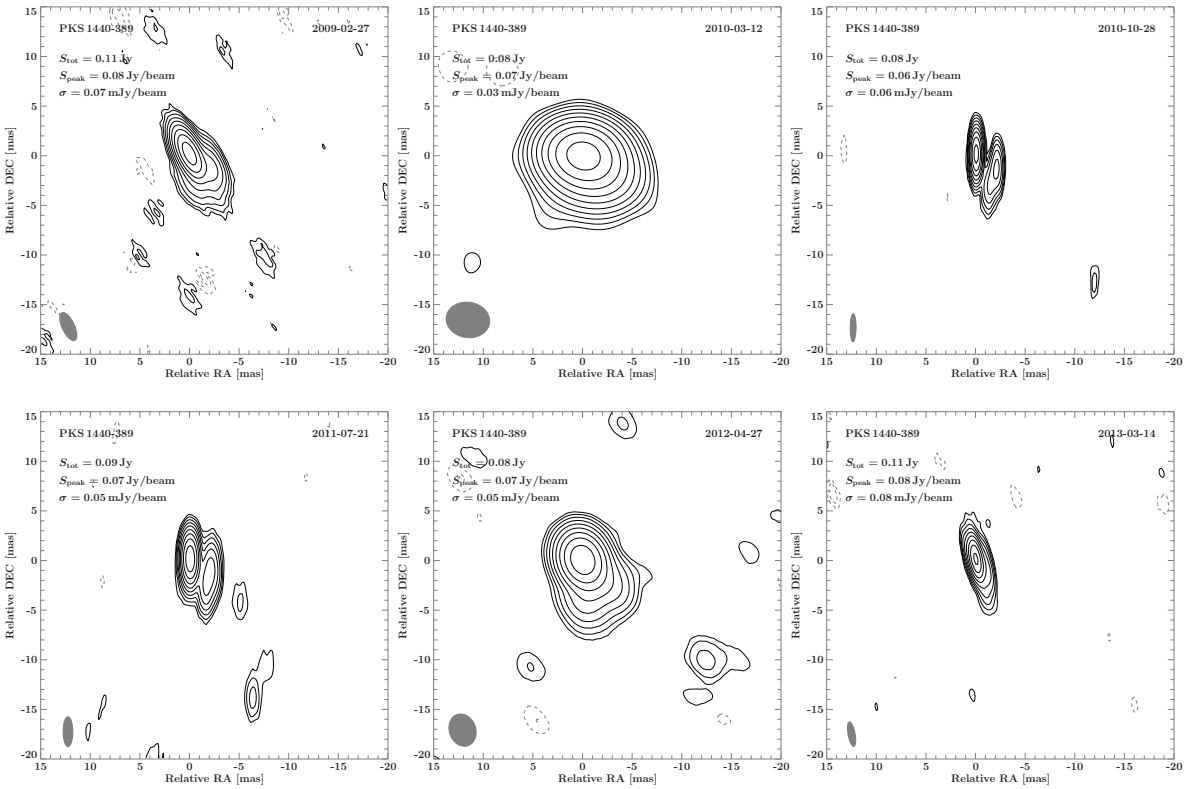

Figure 3.16.: Clean images of the source PKS 1440−389 from VLBI data between February 2009 and March 2013. The observation date is in the upper right corner and the other listed parameters are the total integrated flux density S_{tot}, the highest flux density per beam S_{peak} and the noise σ. The contours scale logarithmically by a factor of 2 and the lowest level is set to the 3σ-noise level. The size of the restoring beam is shown in the lower left corner of each image as a grey ellipse.

afterwards. It seemingly moves closer to the core within those two epochs, but without considering positional uncertainty as well as having it appear in other epochs, no further positional restrictions can be made. It is unlikely however, that this feature is simply an artifact since it shows more than three contour lines in two epochs and when still leaves enough residual flux density at that position when no windows are placed there during imaging. Instead, it can be assumed that the feature is very faint, but slightly variable, becoming only visible in some epochs when its flux density is just high enough to be detected. Finally, there is a feature with three contour lines at a distance of about ~ 18 mas northwest of the core with three contour lines, which however does not reappear to a sufficient extent in the remaining epochs.

When comparing the February 2009 image to the first epoch image by Müller et al. (2017), the inner structure is clearly the same in both images with the bright core and one component directly northwest. In Müller et al. (2017) the source features several

more faint components along the northwestern line. However, these features are both very faint with only two contour lines each and have distorted edges, i.e. the contour lines are not clear ellipses, but rather wavy structures. The only other feature coinciding with the image shown here is the farthest structure at ~ 18 mas, which is assumed to be an artifact. This is another good example of the advantage of multi-epoch imaging, since it is difficult to determine, whether faint features such as these are real or not without comparing the image to other epochs. The tapered image from Müller et al. (2017) shows a clearer, more extended jet in the northwestern direction. Here, the closest component is not visible as well as before since it is likely hidden by the bigger beam, much like in the March 2010 image here, leaving the brightest feature to still be at only three contour lines. However, much like the second feature at 7 mas appearing and disappearing between epochs, it is possible that the distant component at 18 mas became fainter afterwards, so it became undetectable in later epochs.

The overall flux density is constant within the conventional error margins, ranging between values of $0.11-0.13$ Jy. The February 2009 flux density is given by (0.12 ± 0.02) Jy within these uncertainties, which is in agreement with the value shown in Müller et al. (2017). This leads to an average value of $S_{\mathrm{tot,avg}} = (0.13 \pm 0.01)$ Jy.

PKS 2005−489

A total of nine epochs covering the time frame from November 2007 to September 2013 were analyzed for the source PKS 2005−489. The contour maps produced with DIFMAP are presented in Fig. 3.18 and additional information regarding the image parameters is listed in Tab. B.3.

The source features a bright core and a similarly bright component at a distance of about ~ 2 mas southwest of the core and is present in every single epoch. The whole jet has a collimated structure and is propagating to the southwest up to a distance of about ~ 30 mas at a position angle of roughly $\sim -130\,^{\circ}$. However, aside from the closest component, which is well defined in every epoch, the rest of the jet appears as diffuse regions, often with several peaks. Additionally, there is a gap between the inner region and the diffuse part of the jet. This diffuse region changes significantly between epochs and is, for instance, more compact in some epochs, but shows further extension in other epochs. In November 2011 this region appears the most distinct, where it consists of several smaller, disconnected peaks. In three epochs intermediate features are present, i.e. in February 2009, August 2008 and September 2012. It is apparent that the diffuse region must have a complex intrinsic brightness distribution. The imaging process with the CLEAN-algorithm is essentially an inverse Fourier transformation of the complex visibility function combined with a deconvolution of the beam. This includes interpolation since the (u, v)-coverage is limited to the observation times and the telescope baselines at hand. With a complex brightness distribution such as this, small changes in the (u, v)-coverage can lead to drastic changes in the modelled brightness distribution.

As for the imaging process, it should be noted that the August 2008 epoch have a

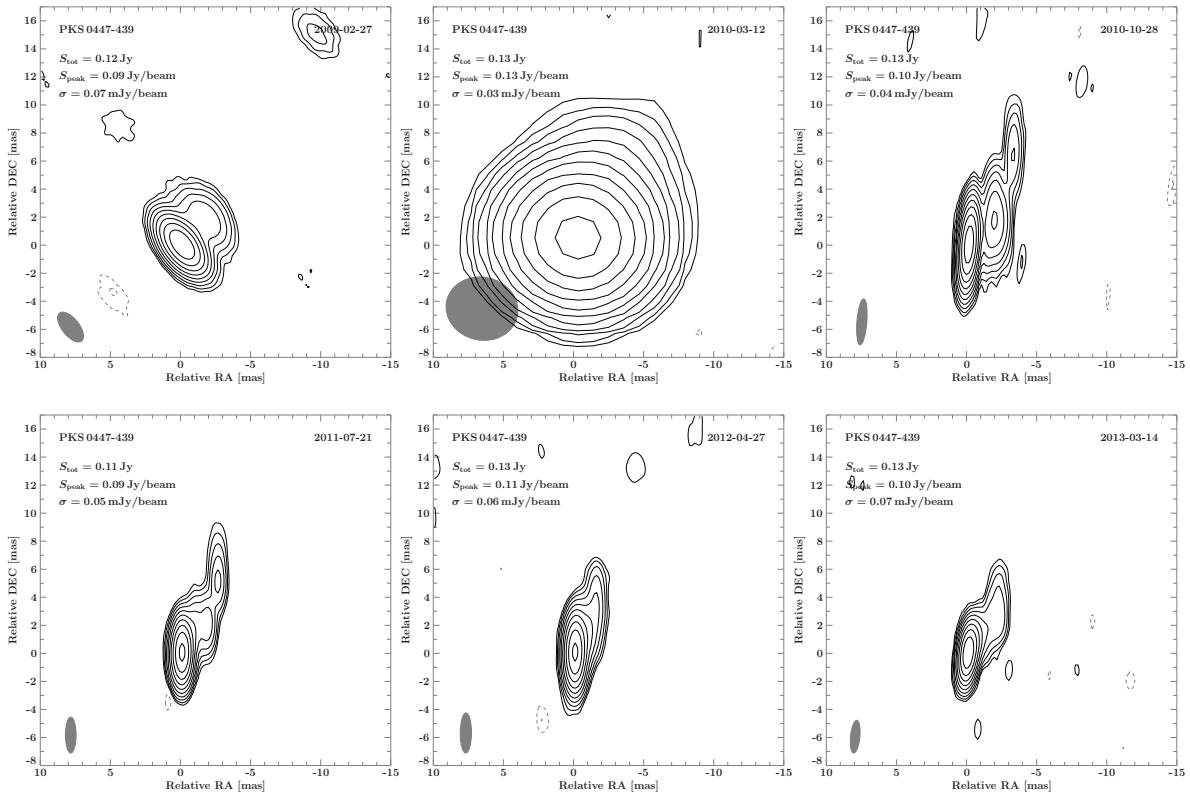

Figure 3.17.: Clean images of the source PKS 0447−439 from VLBI data between February 2009 and March 2013. Source parameters and contours as in Fig. 3.16.

lot of bad data which needed to be flagged. This was especially apparent at the longest baselines, where a lot of the data appeared to be simply noise and no real detection of flux density. Due to this, the beam is larger than it could be and it is likely that this is the reason why the contour map looks more distorted than the rest. Additionally, in both the April 2011 and the November 2011 epoch, a lot of data from the telescope Warkworth were problematic, since the amplitude correction with selfcal lead to an unreasonable increase in flux density for that data. So a lot of the data involving baselines with Warkworth were flagged in those epochs.

Furthermore, the August 2008 epoch appears to feature some contours directly east of the core and there are some very faint one-contour features in March 2008. The latest three epochs can all be modelled to show some emission east of the core which is similar to the bright western component in terms of flux density. Since the object is a Doppler boosted blazar, it is highly unlikely to observe a counter-jet. If future epochs confirm the existence of flux density east of the core, a possibility is that the component identified as the core is actually brighter than the core itself and simply hides the actual core behind it in other epochs. Nonetheless, the images presented here show that neglecting

an extension to the east provides an adequately good model to fit the data.

The November 2007 image presented here features the same inner structure as the image by Ojha, Fey, and Charlot (2005) as well as the first epoch image by Ojha et al. (2010a). However, in the image of the latter the jet has a wider opening angle and extends more to directly south of the core. The diffuse southwestern region is still present, but fainter than in the image of this thesis. Since modelling the intrinsic brightness distribution in DIFMAP is essentially fitting the sampled visibility function with the least squared method, different models can achieve similarly good results. This is true especially for more complex brightness distribution since small changes within the parameters can lead to a different local minimum in the χ^2-plane. Only the comparison with later epochs can lead to a sufficient conclusion on which components are real and which are not.

The other parameters presented in Ojha et al. (2010a), however, are in good agreement with the image parameters here within the uncertainties. The total integrated flux density ranges between values of $0.56 - 0.88$ Jy. Within the conventional uncertainties, the highest and lowest flux density values are not in agreement with (0.88 ± 0.18) Jy and (0.56 ± 0.11) Jy. However, assuming the flux density remains constant throughout all epochs, a deviation of ~ 1.3 times the error is not outside of statistical expectation. This then leads to an average flux density of $S_{\mathrm{tot,avg}} = (0.70 \pm 0.11)$ Jy.

PKS 2155−304

PKS 2155−304 has been observed with the TANAMI array in the time frame from March 2008 to September 2012 for a total of eight epochs. The contour maps produced with DIFMAP are presented in Fig. 3.19 and additional information regarding the image parameters is listed in Tab. B.4.

The structure of the source consists of a bright core and a jet which is, in general, directed toward the southeast with a position angle of approximately $\sim 140\,^\circ$. Essentially, three main features can be identified within the different epochs. The first is located at a distance of about ~ 3 mas southeast of the core and is clearly present in all epochs until May 2010, with differing positions and extensions. The second feature can be found further to the southeast with a gap between the features. In March 2008 it is located at about ~ 13 mas away from the core and appears to be propagating further away, being at a distance of ~ 18 mas. This feature is not present in September 2009, March 2010 as well as September 2012. While the latter epoch generally features a more compact structure compared to the other epochs, the September 2009 contour map appears to be more diffuse closer to the core. Additionally, the long baseline data in this epoch appear to consist mostly of statistical noise. Hence, it is possible that this epoch suffers from some artifacts. As for the March 2010 observation, the total integrated flux density is the lowest out of all observations for this source with $S_{\mathrm{total}} = (0.24 \pm 0.05)$ Jy. If the distant feature behaves like the inner structure and became fainter, it may have simply not been detected by the array. It should also be noted that the August 2008 epoch suffers

from many artifacts and shows structures with more distorted edges in general. This epoch was also present in PKS 2005−489, so the same explanation applies here. Finally, the third feature is an extension directly south of the core up to a distance of ~ 5 mas. While earlier observations showed no signs of a southern extension, it is present in the September 2009 and May 2010 and following epochs. The feature is probably unresolved in March 2010 due to the large beam.

The image from March 2008 is very similar to the first epoch image presented by Ojha et al. (2010a), with the inner structure being morphologically identical. The only difference is the location of distant southeastern feature, which is located at a distance of about ~ 14 mas and at a smaller position angle compared to the image of this thesis. However, this deviation can be accepted within positional uncertainties. Compared to the VLBA images at 43 GHz by Piner, Pant, and Edwards (2010), the structure is largely the same, but at a higher dynamical scale. In Piner, Pant, and Edwards (2010) the jet is extended up to a distance of only ~ 3 mas southeast of the core as opposed to the $13-18$ mas here. Furthermore, they also find an extension directly west of the core which is not present in any of the 8.4 GHz images. Their contours show a bending of the jet, starting west and eventually bending toward the southeast. Furthermore, jet-bending between pc- and kpc-scales towards the northwest was proposed by Seeg (2017). With the changing morphology within the epochs produced here, it is difficult to determine whether jet-bending is observed here as well.

The total integrated flux density of the March 2008 observation is given by $S_{\mathrm{tot}} = (0.48 \pm 0.10)$ Jy and is in agreement with the value given in Ojha et al. (2010a). Across the epochs, the flux density ranges from values between $0.24 - 0.48$ Jy, which does not appear to be constant within the conventional error margins and the lowest flux density is almost two standard errors away to be in agreement with the highest flux density value. Considering the drastic changes in morphology throughout the epochs, some degree of flux density variability cannot be ruled out.

PKS 0625−354

The data provided for PKS 0625−354 covers a time frame from November 2007 to September 2012 for a total of nine epochs. The images produced by DIFMAP are shown in Fig. 3.20 and additional information regarding the image parameters is listed in Tab. B.5.

The source structure consists of a bright core and a straight, collimated jet to the southeast at a position angle of about $\sim 150\,^{\circ}$. In most epochs it features three components at distances of about $2-3$ mas, $6-7$ mas and 18 mas to the core. While the inner two components are well defined in almost all epochs, the more distant feature is more complex in most epochs. It appears to actually consist of three components in November 2011 and is more diffuse in April 2011, likely due to the very small beam. However, in the other epochs, this region is mostly unresolved and appears as one structure. Furthermore, in this and the September 2012 observation the jet appears more continuous than

in the other epochs, making a clear distinction of two single components in the inner structure more difficult. In June 2008 only the inner structure of the jet is visible. This is mainly due to the fact that the data on longer baselines is overestimated by a large margin, reaching initially higher flux density values than the shortest baselines, likely due to a calibration error. Through amplitude self-calibration, the data were corrected towards lower values, which were still almost as high as the short baseline flux densities and significantly higher than in the other epochs.

In comparison to the first epoch image by Ojha et al. (2010a), the morphology and direction of the jet are largely the same. However, they detect diffuse emission from the jet up to a distance ~ 95 mas to the core in their tapered image which is not observed in any of the images shown here. If this distant emission exists, it must be very faint since the total integrated flux density from the image for this thesis with $S_{\mathrm{tot}} = (0.37 \pm 0.07)$ Jy is in agreement with the value listed in Ojha et al. (2010a).

The total integrated flux density throughout all epochs ranges between values of $0.37-0.46$ Jy and remains constant within even an uncertainty measure of 15 %. Thus, the flux density can be taken as constant and results in an average value of $S_{\mathrm{tot,avg}} = (0.41 \pm 0.03)$ Jy.

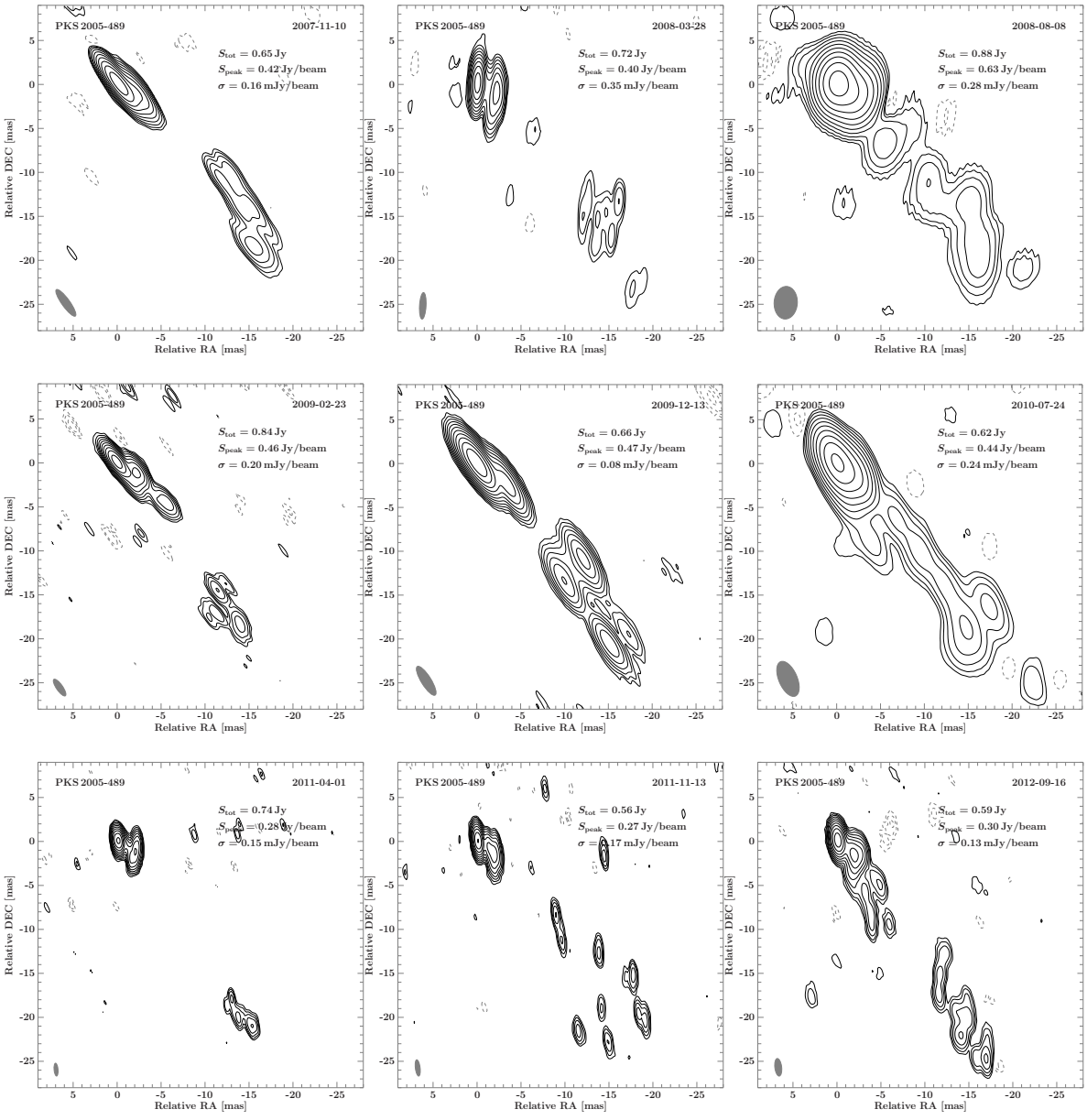

Figure 3.18.: Clean images of the source PKS 2005−489 from VLBI data between November 2007 and September 2012. Source parameters and contours same as in Fig. 3.16.

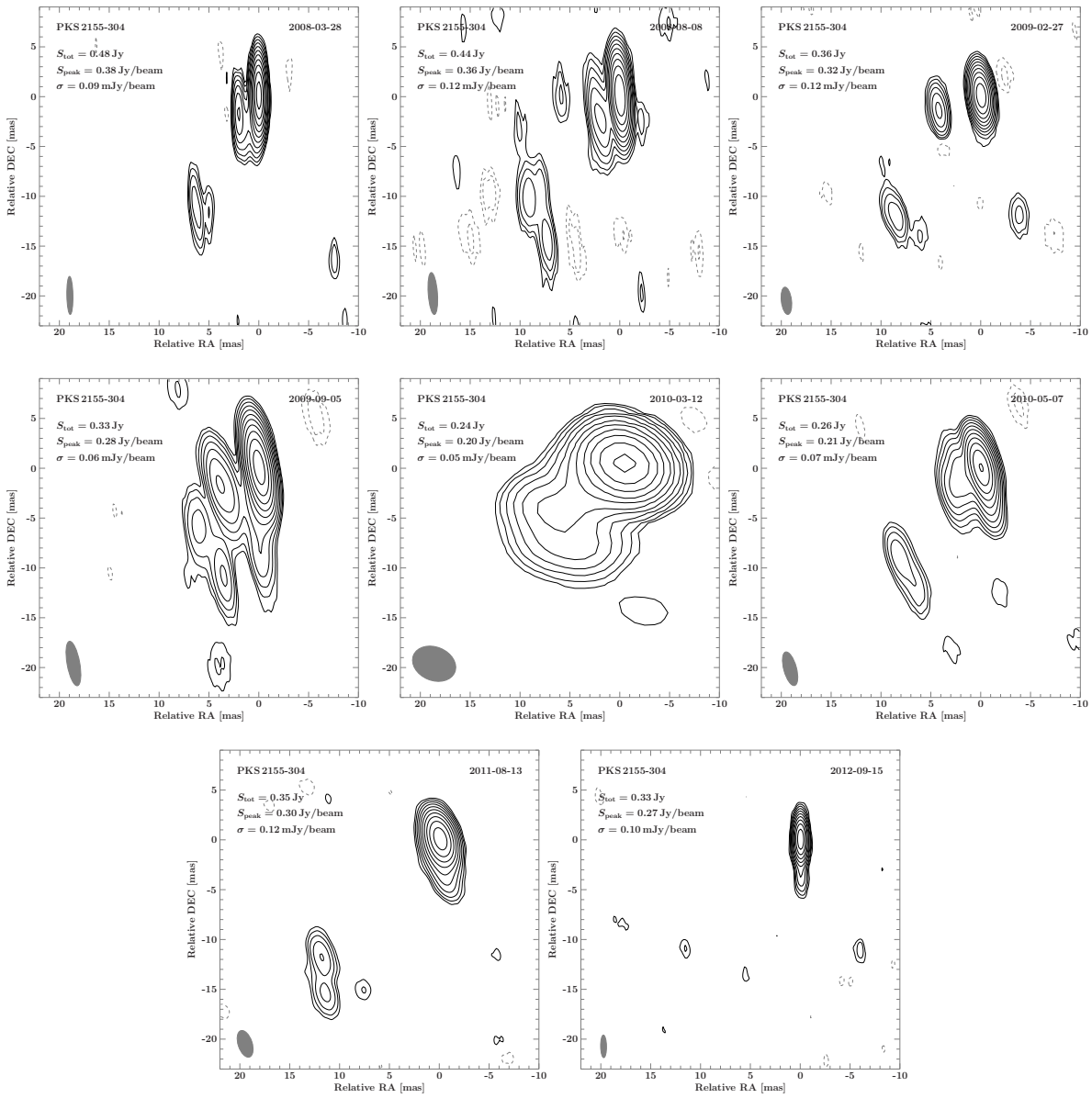

Figure 3.19.: Clean images of the source PKS 2155−304 from VLBI data between November 2007 and September 2012. Source parameters and contours same as in Fig. 3.16.

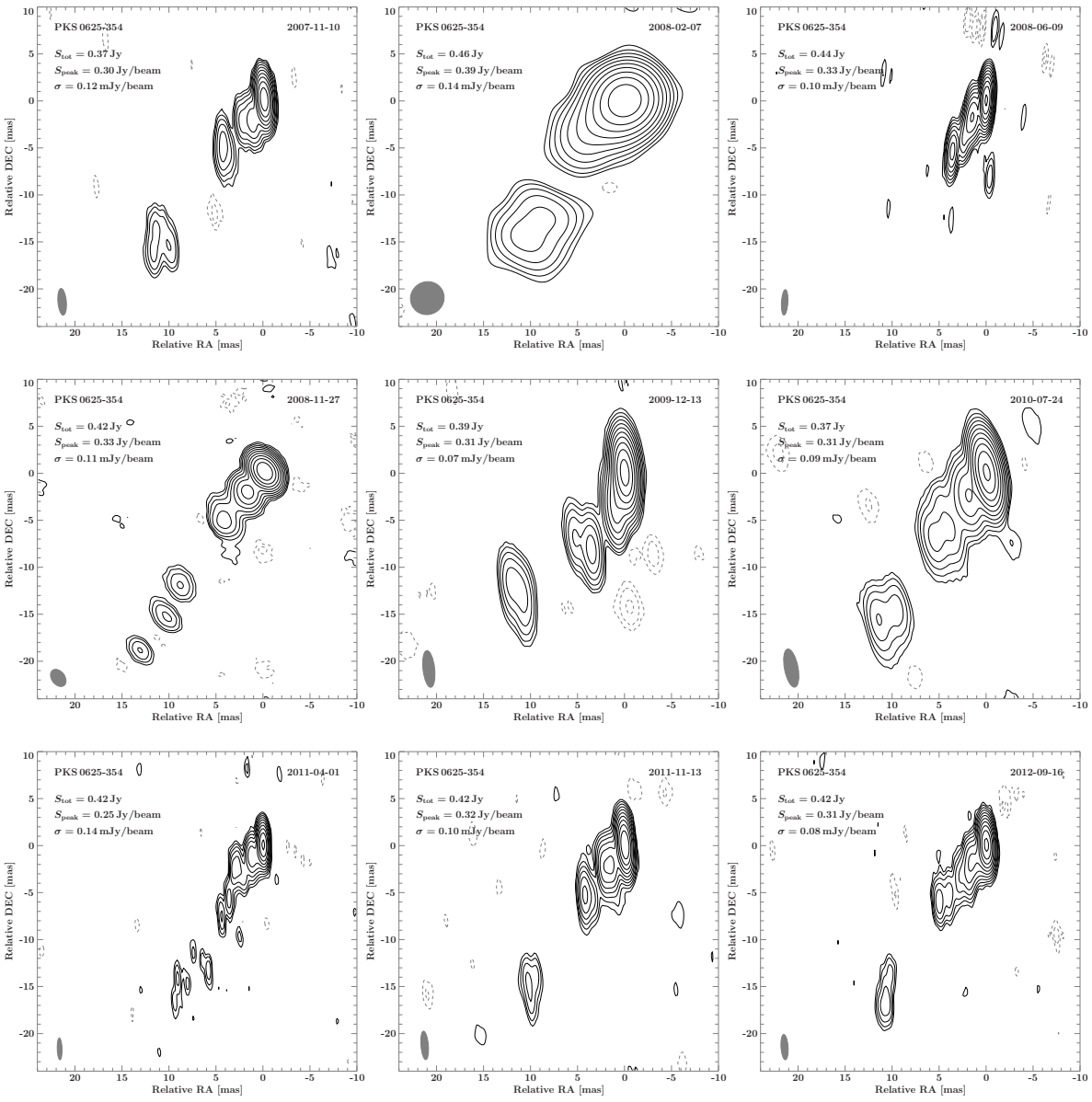

Figure 3.20.: Clean images of the source PKS 0625−354 from VLBI data between November 2007 and September 2012. Source parameters and contours same as in Fig. 3.16.

3.3. Modelfitting

As stated previously, after calibrating the initial data with the CLEAN algorithm and several steps of self-calibration, a properly calibrated remap is created. The calibrated data are then fitted with two-dimensional circular or elliptical Gaussian components in order to track the radio knots visible in the contour maps and thus be able to perform a kinematic analysis. This section will focus on explaining how and why the components were fitted within the model as well as elaborate on problems met during the fitting of the model. The results gained from the kinematic analysis are the focus of the next section.

PKS 1440−389

PKS 1440−389 is fitted with a simple model consisting of the core and a single component southeast of the core. The time-evolution plot is shown in Fig. 3.21 and all model fit parameters are listed in Tab. B.6. The solid lines in Fig. 3.21 represent the reconstructed movement of each component based on the velocity gained by unweighted linear regression of the component distance over time relative to the core. The component is fitted as a circular Gaussian in all instances, whereas the core is fitted as an ellipse when possible. In certain epochs, i.e. March 2010 and April 2012, the core is unresolved along its minor axis, so a circular Gaussian is used instead. This model is consistent throughout all presented epochs, with no further divergences. In April 2012 the southern to southwestern region can also be fitted with two circular Gaussians. However, for the sake of tracking the bulk motion of the entire southwestern jet, only one component is used within this model. In March 2013 the FHWM of the fitted component extends further to the east than the contour lines of the clean image indicate, so it may be possible to image this epoch with additional southwestern extension.

PKS 0447−389

The jet of PKS 0447−439 can be fitted with an elliptical core in all but one epoch, namely in March 2010, likely due to the big, circular beam, so a circular Gaussian is used in this epoch. The time-evolution across all epochs is presented in Fig. 3.22 and the model fit parameters are listed in Tab. B.7. The northwestern jet can be fitted with one to two circular Gaussian components in every epoch. The component C1 appears in every observation, while the more distant component C2 appears only in October 2010 and July 2011. April 2012 and onward show the emergence of a small new component close to the core. Usually the emergence of a new component is expected to be preceded by a flaring state. However, it is very well possible, that such a small component was simply hidden by the core and only became apparent now due to either better resolution, further propagation or both. Since two of the components only appear in two epochs each, an unweighted linear regression is unreasonable, so only a speed for C1 is

determined later.

PKS 2005−489

Due to the diffuse and changing nature of the jet in PKS 2005−489, it is difficult to model the entire jet consistently using simple circular Gaussian components. Hence, only the core and the component closest to the core are modelled properly throughout all epochs. In some epochs, one more component arises. In order to show that there is no merit in modelling the distant diffuse region of the jet, one exemplary component has been fitted to it in each epoch. The time evolution is shown in Fig. 3.23 and the model fit parameters are listed in Tab. B.8.

The core is unresolved in one direction in six out of nine epochs. Only in February 2009 as well as April and November 2011 does an elliptical Gaussian converge for the core. Component C1 is clearly visible and well modelled in all epochs. In December 2009 its position is further away from the core compared to the remaining epochs. In August 2008 and February 2009 a second component, labelled C2, is resolved. It seems that the two components are viewed as a single one in December 2009 due to the big beam along with its high position angle. This would lead to a shifted peak located somewhere between the actual C1 and C2 components, leading to the increased distance of the model component. Additionally, a component identified here as C2 can be fitted in September 2009. However, its position is much closer to the core here than in the other two epochs and appears more diffuse than before. This in addition to C2 appearing in only three epochs means that determining a velocity for C2 is unreasonable.

It is apparent in Fig. 3.23 that the single circular Gaussian component C3 is not enough to model the diffuse region to the far southwest. However, the region contains several peaks in all epochs, which could warrant the placement of many Gaussian components. Since the number and position of these peaks changes significantly between epochs, with the most extreme epoch being the November 2011 observation, performing a kinematic analysis is not feasible for this region.

PKS 2155−304

Within the first few epochs, PKS 2155−304 can be modelled rather consistently and changes its structure towards the end. The southeastern jet can be modelled with two to three circular Gaussians in each epoch and an elliptical core in half of them. The minor axis of the core is unresolved in March and August 2008 as well as March 2010 and August 2011. The resulting time evolution plot is shown in Fig. 3.24 and the model fit parameters are listed in Tab. B.9.

In March 2008 the peak positions of the components are off-centered compared to where the contour lines indicate flux density maxima. It is possible that the core component is not fitted well with enough flux density, leaving residual flux density close to it. Hence, the peak position of C1 lies between the residual flux density from the core

and the close peak in southeastern direction. It should also be noted that in some epochs the image process with point source components allows for some freedom of placement of the windows. This can be the case when two similar models are close by on the plane of parameters, where the fit can potentially happen to "hop" between different local minima. Nonetheless, C1 is well modelled in the remaining epochs up to May 2010 and disappears afterwards. In August 2011 there is a component labelled as C5 at a similar position angle, but much closer to the core, making it unlikely that this is the same component as C1.

The distant, more diffuse component C2 is modelled sufficiently well with a circular Gaussian and can be tracked up to August 2011, but is not present in some epochs in between. The contour lines in March 2010 indicate an extension up to the distance of C2. However, that region cannot be modelled well with two circular Gaussians, indicating that the C1 in this epoch is likely located at an average position between these two components. Component C4 in September 2009 is used to model the diffuse emission southeast of the core. Otherwise, the component directly south of the core, C3, cannot be fitted well due to it being fainter than the diffuse emission. C3 then continues to appear in all subsequent epochs, with the exception of March 2010.

PKS 0625−354

The jet of PKS 0625−354 can be fitted almost exclusively with three circular Gaussian components aside from the core. The time evolution is shown in Fig. 3.25 and the model fit parameters are listed in Tab. B.10.

In February 2008 the core component diverges to a point source even with a circular Gaussian model, leading to an unreasonably high brightness temperature far above the known limits. Eq. 2.4.2 provides an upper limit on an arbitrary axis of the core using its signal-to noise ratio given by the fitted core luminosity and the RMS in the region of the core. With a measured noise of $\sigma = 0.336\,\mathrm{mJy/beam}$ and a flux density of $S_{\mathrm{core}} = 0.355\,\mathrm{Jy}$ this results in a ratio of SNR $= 1.06 \times 10^3$. Since the core component is circular, the minor axis of the beam is used, which is $b_{\mathrm{min}} = 3.47\,\mathrm{mas}$. Plugging these values into Eq. 2.4.2 results in an upper limit of $\theta_{\mathrm{lim}} \leq 0.10\,\mathrm{mas}$, finally leading to a lower limit of the brightness temperature of $T_b \geq 6.48703 \times 10^{11}\,\mathrm{K}$. In five of the eight remaining epochs the core was resolved as an ellipse and hence set as a circle in three epochs.

The two inner components, C1 and C2, are visible in every epoch and can be fitted well to the jet in nearly each. In both November 2008 and December 2009, the component C2 diverges to a point source. In order to restrict its size and brightness temperature, the axis is set to the minor axis of the beam, which is 1.40 mas and 1.24 mas respectively. The jet region desribed by C2 appears to be more complex than a single component could describe, which is especially apparent in April 2011 due to its very small beam and to an extent in September 2009, where the jet in general appears more continuous rather than featuring well defined peaks. C3 is further away from the core and appears

to consist of at least to distinct peaks, as is apparent in November 2008. However, only one component is used to describe these two peaks to stay consistent with the remaining epochs, where they are likely too close to be resolved by their respective beams. In April 2011 this region is too diffuse to be fitted by a Gaussian component. In December 2009 the peak of the component is shifted a lot compared to the peak indicated by the contour map. Perhaps the contour map can be imaged differently to agree with the model fit. Additionally, the most distant component C4 appears in November 2008, but is not present in any other epochs. Only a very faint feature with one contour line is present in November 2011 and at roughly the same position.

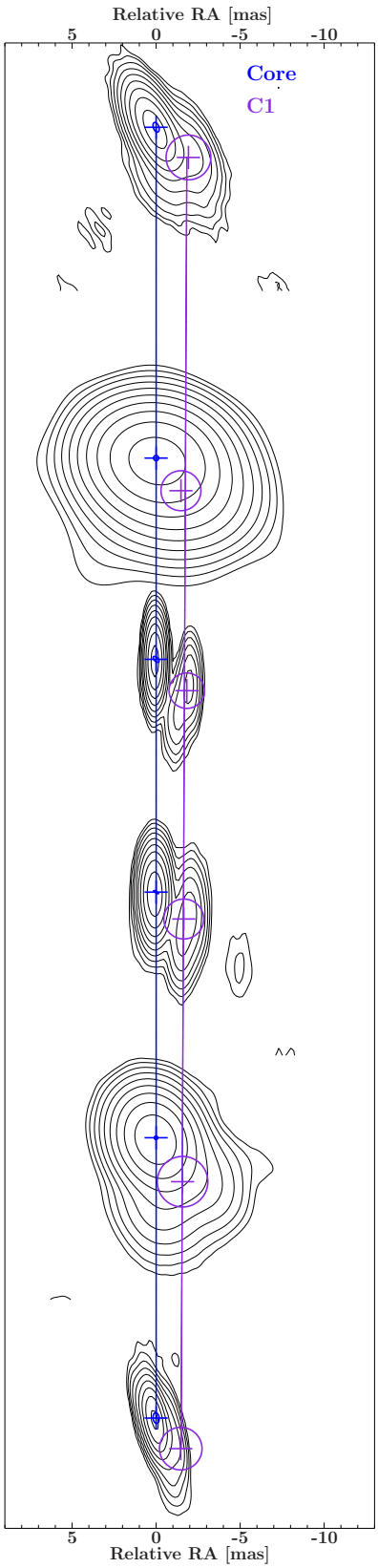

Figure 3.21.: Time evolution plot for PKS 1440−389. The fitted components are plotted over the clean maps. The displacement of the epochs is proportional to the time difference between each epoch. The solid lines represent the movement of the component computed from the parameters gained with unweighted linear regression. Contours are the same as in Fig. 3.16.

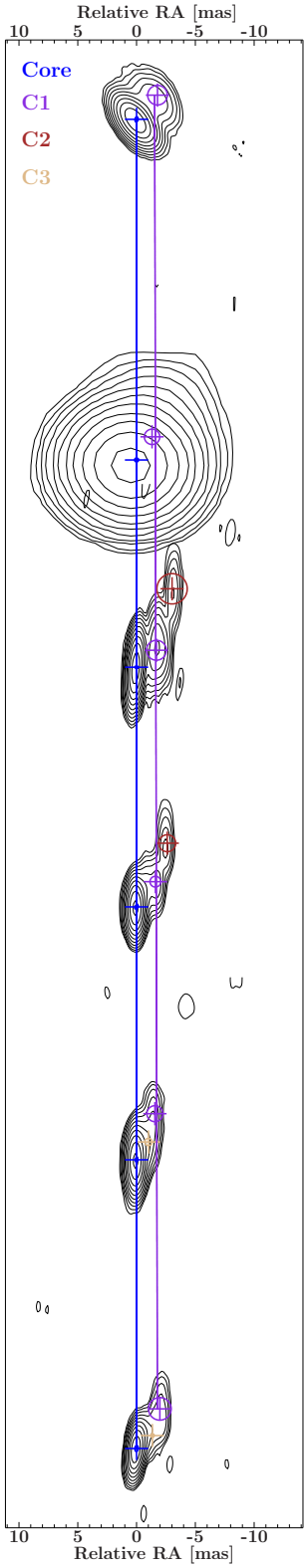

Figure 3.22.: Time evolution plot for PKS 0447−439. The fitted components are plotted over the clean maps. The displacement of the epochs is proportional to the time difference between each epoch. The solid lines represent the movement of the component computed from the parameters gained with unweighted linear regression. Contours are the same as in Fig. 3.16.

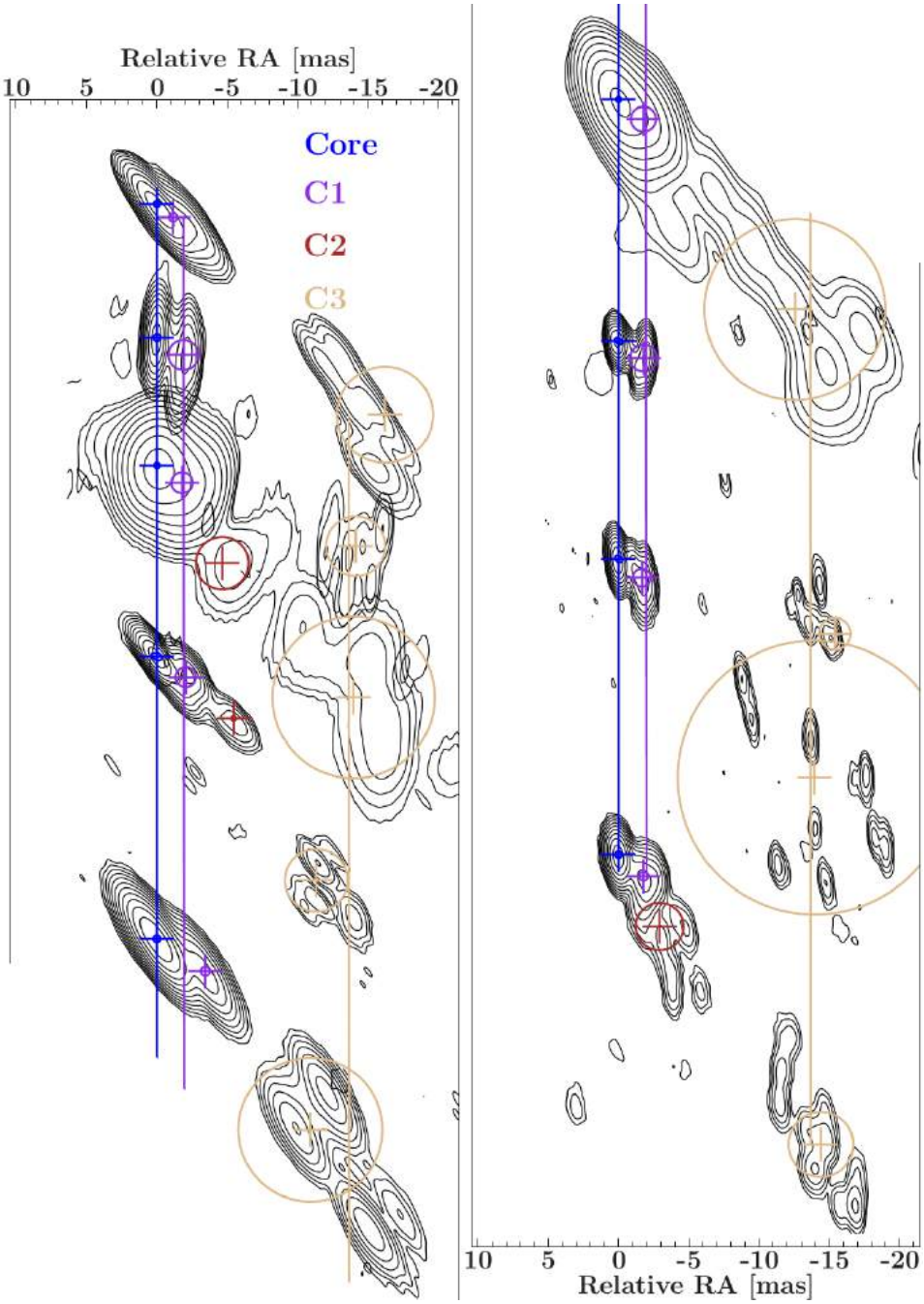

Figure 3.23.: Time evolution plot for PKS 2005−489. The fitted components are plotted over the clean maps. The displacement of the epochs is proportional to the time difference between each epoch. The solid lines represent the movement of the component computed from the parameters gained with unweighted linear regression. Contours are the same as in Fig. 3.16. The image is split in two halves in order to fit the page.

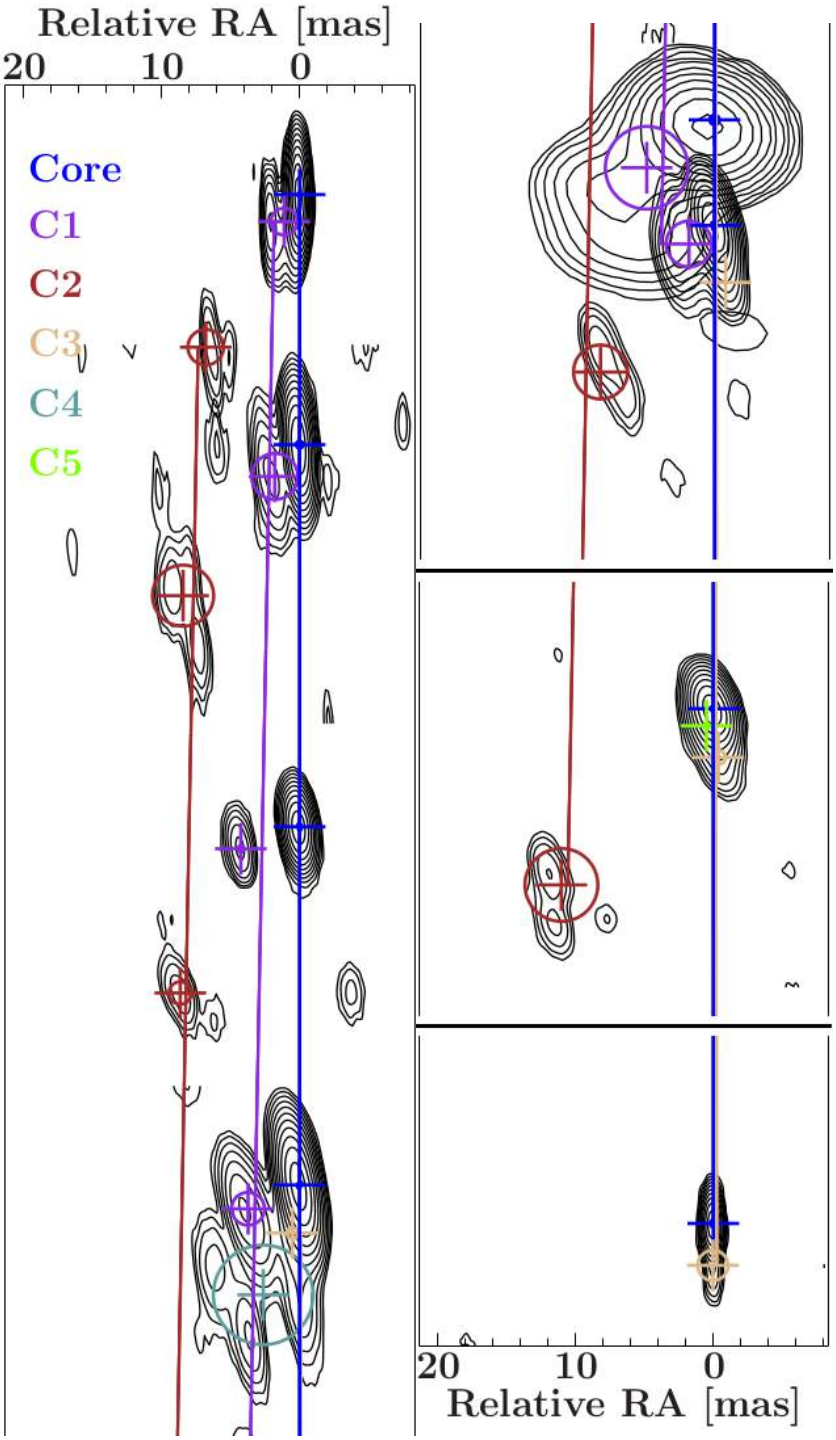

Figure 3.24.: Time evolution plot for PKS 2155−304. The fitted components are plotted over the clean maps. The displacement of the epochs is proportional to the time difference between each epoch. The solid lines represent the movement of the component computed from the parameters gained with unweighted linear regression. Contours are the same as in Fig. 3.16. The image is split in two halves in order to fit the page. The black lines indicate empty portions, which were cut out to fit the image on the page.

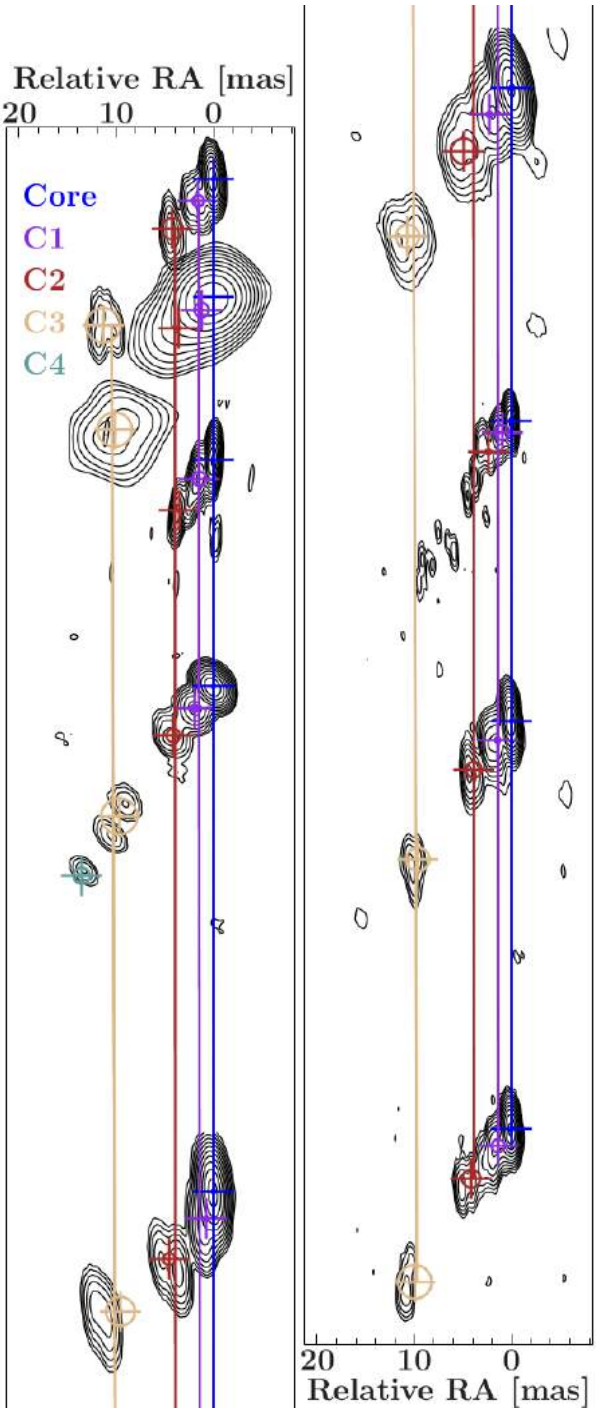

Figure 3.25.: Time evolution plot for PKS 0625−354. The fitted components are plotted over the clean maps. The displacement of the epochs is proportional to the time difference between each epoch. The solid lines represent the movement of the component computed from the parameters gained with unweighted linear regression. Contours are the same as in Fig. 3.16. The image is split in two halves in order to fit the page.

3.4. Results of the Kinematic Analysis

The models fitted in the previous section provide direct information about the position of each component via their radial distance and position angle, their flux density as well as the major and minor axes and hence indirectly about the component velocity and brightness temperature. The following section will present these results for each source and briefly discuss their implications. A more thorough discussion of the jet speeds and properties in comparison to previous results and models as well as especially in the context of the Doppler Crisis will be performed in the next section.

Since no certain redshifts are known for PKS 1440−389 and PKS 0447−439, a redshift of $z = 0.14$ is used for PKS 1440−389 and a value of $z = 0.176$ for PKS 0447−389 respectively. Both values are the lowest known and well computed values since $z = 0.065$ for PKS 1440−389 was gained from bad spectral data and $z = 0.107$ is a remnant of the misclassification of PKS 0447−439 as a Seyfert galaxy.

3.4.1. Flux Density and Brightness Temperature Evolution

In this section the time evolution of the flux density and brightness temperature for each of the source are presented. The flux density error is given by the conventional uncertainty measure and is set to 20 % of the best known value for all sources. All brightness temperatures are computed with Eq. 2.4.1. Since no uncertainties are estimated for the major and minor axes, the brightness temperature error should be at least as high as the flux density error, so it is also set to 20 % of the best known value.

PKS 1440−389

Both the flux density and brightness temperature evolution are shown in Fig. 3.26 for PKS 1440−389. The core is set at a flux density of ~ 0.08 Jy, which is in agreement with the flux density value presented in Böck et al. (2016). The emission is dominated by the core by a factor of roughly 4, since the flux density of component C1 lies around 0.2 Jy. The core emission is constant within the uncertainties, whereas C1 shows a slight decrease in flux density for the last two epochs. This was seen previously in its contour map (Fig. 3.16), since the structure of PKS 1440−389 becomes increasingly more point-like towards later times.

Correspondingly, the brightness temperature of C1 is constant at first at $\sim 6 \times 10^7 - 7 \times 10^7$ K and drops down to $\sim 2 \times 10^7 - 3 \times 10^7$ K in the last two epochs. Since the temperature follows the flux density evolution very well, there must be no variability in the size of the component. The brightness temperature of the core is constant for the most part at $\sim 8 \times 10^9 - 1.5 \times 10^{10}$ K. While the values are in agreement with Böck et al. (2016), a comparison is unreasonable since they used a different redshift. However, in July 2011 and April 2012, the brightness temperature rises to $\sim 5 \times 10^{10} - 6 \times 10^{10}$ K

despite a constant flux density. Hence, this increase can be attributed to smaller sizes of the core component. This is likely due to a combination of a smaller beam and a better SNR, leading to an increased resolution. All temperatures are moderate and are below both the Compton as well as the equipartition limits of 10^{12} K and 10^{11} K respectively.

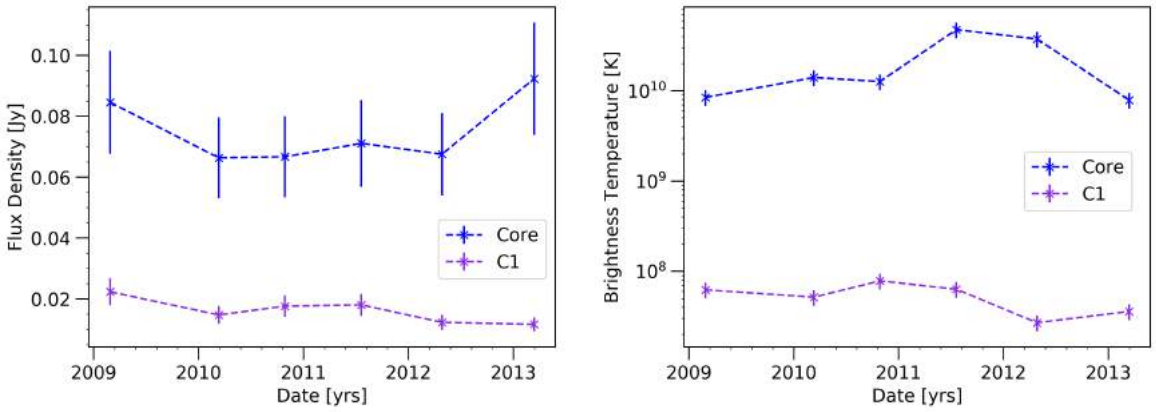

Figure 3.26.: Flux Density (left) and Brightness temperature (right) over time for the source PKS 1440−389. The flux density errors correspond to the conventional TANAMI uncertainty of 20 %. The error of the brightness temperature is set to 20 % as the lowest error, since the uncertainty of the axes is unknown.

PKS 0447−439

The flux density and brightness temperature evolution of PKS 0447−439 are shown in Fig. 3.27. Similar to PKS 1440−389, the emission of PKS 0447−439 stems mainly from the core with a flux density of ~ 0.11 Jy, which is in agreement with Böck et al. (2016) and constant within its errors. All other components feature flux densities below ~ 0.01 Jy, with the exception of C1 in October 2010 with a flux density of 0.019 Jy. The flux density of C1 rises up to this point and decreases to a slightly lower level than before the rise. C2 shows a very low flux density close to 0 in both of its detections. It is possible that this component was only visible twice due to either better sensitivity in the respective observations or due to variability in C2, where it was just bright enough to be detected in October 2010 and July 2011. C3 is slightly brighter in both its epochs than C1, but still very faint compared to the core. The component was most likely too outshined by the core when it was still too close and was far enough just recently to be identified as a component. The flux density bears no correlation to its *Fermi*/LAT-lightcurve in Fig. 3.4, which instead shows increasing and decreasing phases.

The brightness temperature of the core is located in the range of $1.5\times10^{10}-3\times10^{10}$ K and follows the flux density evolution very well. The only exception is in March 2010,

reaching up to 5×10^{10} K and is correspondingly the only epoch, where the core is resolved as a circular component instead of an elliptical one. Despite Böck et al. (2016) computing a lower limit with $z = 0$, their temperature appears to be larger than the one seen here. Perhaps they used a circular and thus smaller component to model the core. Due to its small size, C3 has a significantly higher brightness temperature than the other components, with C2 being the lowest due to its low flux density and large size. the brightness temperature of C1 features a "time lag" of decrease compared to the flux density. Between October 2010 and July 2011 the size varied inversely to the change in flux density, leading to the observed evolution. Additionally, the size of the component correlates with its distance to the core, as predicted by a conical jet model. None of the temperatures are particularly high, however, and are all below both limiting values.

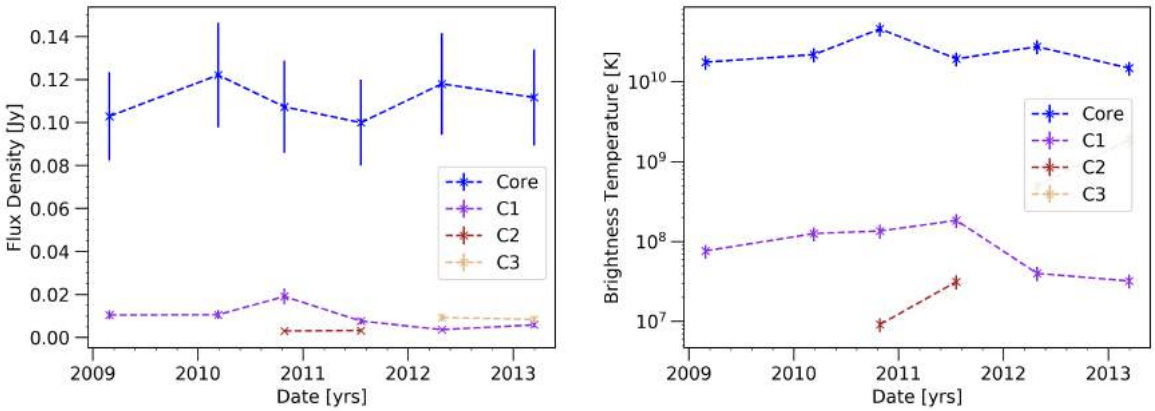

Figure 3.27.: Flux Density (left) and Brightness temperature (right) over time for the source PKS 0447−439. The flux density errors correspond to the conventional TANAMI uncertainty of 20 %. The error of the brightness temperature is set to 20 % as the lowest error, since the uncertainty of the axes is unknown.

PKS 2005−489

Figure 3.28 shows the time evolution of the flux density and brightness temperature for PKS 2005−489. Judging only by the best values, the core flux density shows some variability with increasing and decreasing phases. It shows some similarity to its Fermi light curve in Fig. 3.8, with a higher flux density prior to the drop in mid 2010 and a subsequent rise in 2011, just to decrease again afterwards. However, within its uncertainty, the flux density remains constant for a value of ~ 0.4 Jy. The core flux density given by Böck et al. (2016), which is derived from the first epoch image, is higher than the one from this model. It is possible to model the inner region, i.e. the core together with C1, as a single ellipse, which is however unresolved in one direction. Since this

region is modelled with two circular components here, the sum of the flux densities is (0.577 ± 0.12) Jy, which then agrees with Böck et al. (2016). Compared to the total integrated flux densities from imaging (see Sect. 3.2), it is apparent that a significant amount of flux density is contributed by the closest component, C1. Its flux density is set around ~ 0.2 Jy for most epochs with some exceptions. In November 2007 its flux density is lower than later on possibly due to its close vicinity to the core combined with an unfortunate position angle of the beam, which is close to the position angle of C1 relative to the core, leading to difficulties when determining the exact flux densities during fitting. The other exception is in December 2009, where the flux density of C1 drops significantly. Additionally, this is the only epoch in which its distance to the core varies significantly compared to the other epochs (see Fig. C.1). Previously in Sect. 3.2 it was assumed that the beam lead to C1 and C2 being unresolved, thus making the model set the peak of the model component between C1 and C2. However, the significant decrease in flux density instead indicates that there is a calibration error in this epoch. Finally, the flux density of C1 decreases again for the last two epochs similar to the core, but still remains constant within only $\sim 1.6\sigma$. C2 on the other hand is a very faint component with flux densities close to 0 in all three detections. The flux density variability in C3 is easily explained by the imaging process: Since the visible regions change drastically with changing (u, v)-coverage, the modelled region changes as well and sometimes more or less of the diffuse jet is properly described by the model component. Nonetheless, the resulting flux densities are consistent for most epochs, implying that similar regions are fitted throughout these epochs.

The brightness temperature of the core ranges between values of $\sim 3\times10^{10}-6\times10^{10}$ K. However, its evolution does not follow the flux density as well, hence it is governed by the change in component size, especially in August 2008. Despite a lower flux density of the core than in Böck et al. (2016), the measured brightness temperatures are in good agreement. C1 is shifted by around one magnitude with values at $\sim 1\times10^{9}-3\times10^{9}$ K, but reaches peak values of $\sim 10^{10}$ K in the first and last epoch respectively, showing the variability in the component size. The brightness temperature of C2 is very high in February 2009 due to its small size despite a low flux density, but is very low otherwise. The brightness temperature of C3 remains low, but since the fitted regions of the diffuse jet vary in size and position, it is unreasonable to discuss its brightness temperature. The core temperature comes close to the equipartition limit of 10^{11} K, but is still below, indicating a low degree of Doppler boosting.

PKS 2155−304

PKS 2155−304 is by far the strongest core-dominated source in the sample. Its core features variable emission between $\sim 0.2-0.4$ Jy, starting out at its highest in the first epoch, in agreement with Böck et al. (2016), and constantly decreasing to its lowest flux density in the beginning of 2010. From then on, it seems to rise again to a mid-flux density of ~ 0.3 Jy. This decrease to its lowest point in 2010 is similar to its Fermi

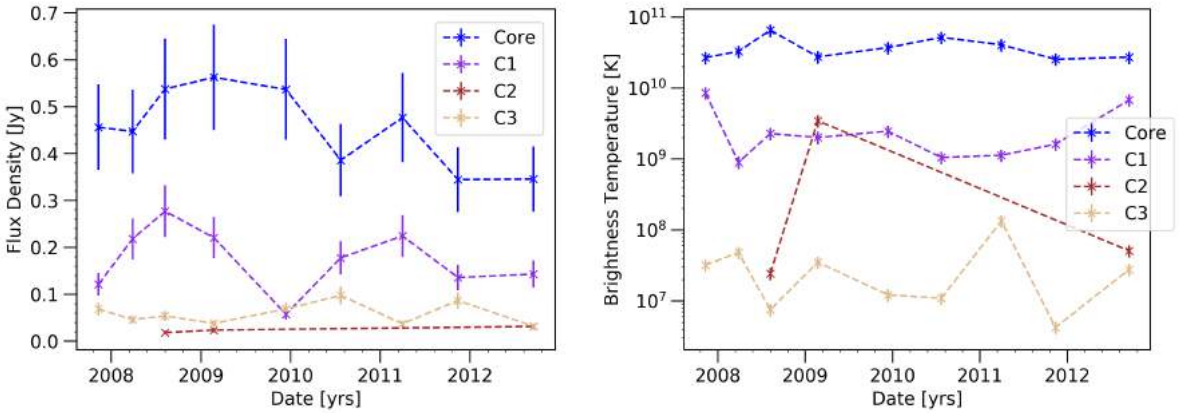

Figure 3.28.: Flux Density (left) and Brightness temperature (right) over time for the source PKS 2005−489. The flux density errors correspond to the conventional TANAMI uncertainty of 20 %. The error of the brightness temperature is set to 20 % as the lowest error, since the uncertainty of the axes is unknown.

light curve in Fig. 3.10. However, the Fermi flux density then reaches a highest peak in 2011, not present in the radio data, just to drop to its lowest state again. However, no data are present in the beginning of 2011 to confirm or deny the existence of a peak in the radio frequencies. But the subsequent flux density does not correspond to a low state. The flux density of the components is almost neglectable and close to 0 without variability for all but C1. This component shows a decrease from ~ 0.05 Jy down to ~ 0.01 Jy in 2009, followed by a increase to the previous flux density in 2010 and appears to be independent of the core in its behaviour. These low component flux densities are an indicator of the drastically changing source morphology seen in the images in Fig. 3.19. Such low flux densities would allow the components to appear and disappear from detection due to being narrowly above or below the sensitivity of the observing array.

The brightness temperature of the core remains largely the same at around $\sim 3\times10^{10}$ K for most epochs. In March 2008 it features its highest temperature at $\sim 1\times10^{11}$ K, higher than the equipartition limit. This value is also slightly higher than the one listed in Böck et al. (2016), but it agrees within its error. Additionally, its error allows the temperature to be below the equipartition limit. Correspondingly, this epoch featured the smallest core size of all epochs. This is due to its good resolution, since this epoch also features the smallest minor axis of all beams. In March 2010 the temperature instead shows a drop to $\sim 1 \times 10^{10}$ K, due to the large beam in this epoch and the resulting big core component size. Unlike the core, however, all components feature rapidly changing brightness temperatures, most notably C1 and C2, which reach up to $\sim 2 \times 10^{9}$ K and $\sim 4 \times 10^{9}$ K respectively. Since the flux densities did not change significantly, this indicates rapid changes in the component sizes throughout all epochs, also reflected by the changes in

the contour lines within each epoch (see Fig. 3.19). The changing sizes could be related to the low flux densities of the components. Since the emission is already very faint and the component size is a measure of the full width at half maximum, the edges of each component could, for some epochs, be below the sensitivity and thus the component appears to be smaller than in previous epochs, where the edges were bright enough to be detected. Additionally, the changing size of C3 could be a problem of it being too close to the core in some epochs, thus leading to difficulties during the fitting process. Aside from one value, which still agrees within its errors, all brightness temperatures are below both limits, again indicating a low degree of Doppler boosting.

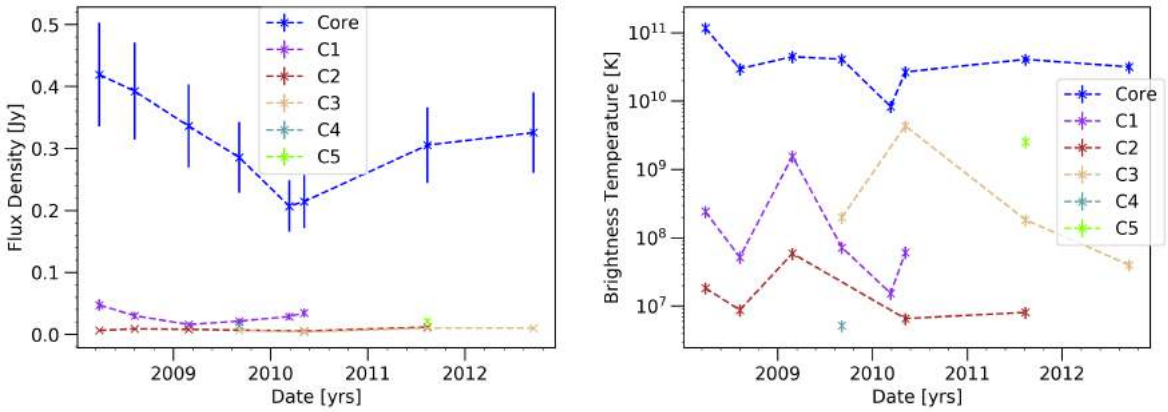

Figure 3.29.: Flux Density (left) and Brightness temperature (right) over time for the source PKS 2155−304. The flux density errors correspond to the conventional TANAMI uncertainty of 20 %. The error of the brightness temperature is set to 20 % as the lowest error, since the uncertainty of the axes is unknown.

PKS 0625−354

The core flux density of PKS 0625−354 shows the least amount of variability from all sources of the sample, with a well defined level at ~ 0.35 Jy, which is also in good agreement with the value given in Böck et al. (2016). Much as the other sources, the emission is largely core-dominated, with all other components being below 0.1 Jy. Both C2 and C3 are mostly close to 0 and show similar flux density values, although C2 shows slightly more emission, going up to ~ 0.02 Jy. C1 features the strongest emission of all components in PKS 0625−354 and some small variability, where some epochs are brighter than others. In total, its flux density is in the range of $\sim 0.02 - 0.08$ Jy. It should be noted that, since the flux density error is simply given by 20 % of its value, the uncertainty of low flux density values is likely underestimated, leaving the possibility that some seemingly variable emission is actually constant within the "real" errors.

The brightness temperature, on the other hand, changes more rapidly for most components. The core temperature is at $\sim 4 \times 10^{10} - 7 \times 10^{10}$ K for all but two epochs. In both February and June 2008 the temperature reaches values of $\sim 6 \times 10^{11}$ K, above the equipartition limit. Furthermore, it is only a lower limit in February 2008 and despite its large beam, this epoch benefits from a good signal-to-noise ratio. The June 2008 epoch should be taken critically, since this epoch suffered from badly calibrated data on long baselines and may not give proper information. Even though the flux density is in good agreement for the first epoch, its brightness temperature is lower than the value listed in Böck et al. (2016). Perhaps they used a different number of components and were able to further restrict the core component size, leading to a higher temperature. Similar to the core, the brightness temperature of C2 is particularly high in the same two epochs of 2008, but also in April 2011. It is assumed that the region of the jet, where C2 is assumed, is actually a more complex structure and becomes more diffuse with better resolution. So a single component may not be enough to describe this region. On the other hand, C1 shows a smaller degree of variability in its temperature, but still enough, to indicate that the component sizes are changing throughout the epochs. With each subsequent epoch, the jet of PKS 0625−354 becomes more continuous in its inner region. Simple circular Gaussian components are then insufficient to describe the form which is devoid of well defined peaks, leading to changing component sizes. C3, on the other hand, shows only minor changes in temperature. The region appears to be more complex in some epoch, but is still unresolved enough to be fitted well with a single Gaussian component. Aside from the two problematic epochs in 2008, all brightness temperatures are clearly below the established limits and even then are the two highest values still below the Compton limit, again indicating a low degree of Doppler boosting.

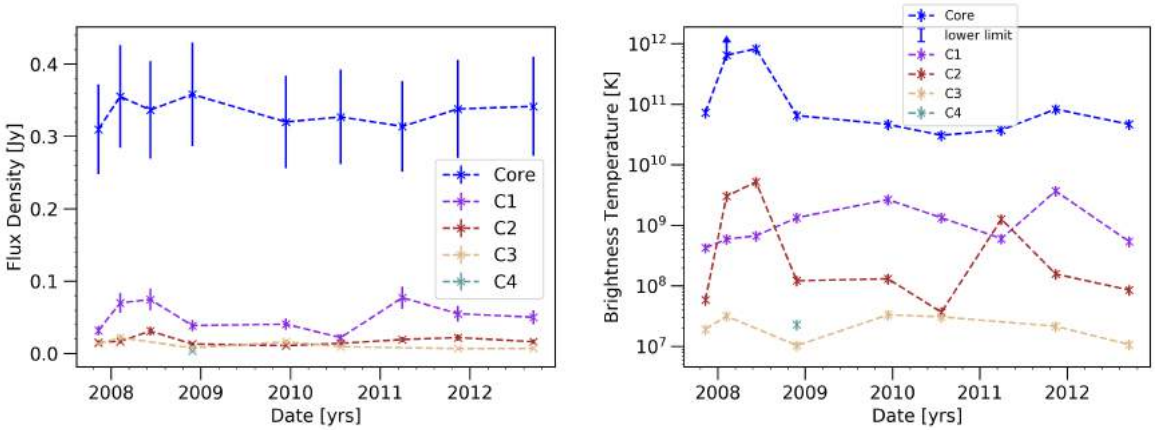

Figure 3.30.: Flux Density (left) and Brightness temperature (right) over time for the source PKS 0625−354. The flux density errors correspond to the conventional TANAMI uncertainty of 20 %. The error of the brightness temperature is set to 20 % as the lowest error, since the uncertainty of the axes is unknown.

To summarize, all sources feature none or only minor variability in their flux density, with PKS 2155−304 featuring the most variable flux density. The emission is usually dominated by the core with mostly faint components. PKS 2005−489 features the brightest jet component, which reaches the highest flux density in comparison to its core out of all the sources. Finally, while some epochs showed variable and particularly high brightness temperatures, almost all values are moderate and below the Compton and equipartition limits for all sources, indicating only minor Doppler boosting.

3.4.2. Apparent Jet Component Velocities

In order to gain a measure of the propagation velocity of a jet, the position of each component can be fitted linearly to compute its apparent velocity. There are two general approaches to determine them:

The first approach is to simply take the radial distance of each component relative to the core and perform a linear regression by assuming constant motion with the core-distance over time. This assumes that the jet performs a constant motion in a straight line away from the core, with no acceleration or jet-bending. With this method, the deviations along particular x- and y- directions are not taken into account. Suppose a circle around the origin (or more precisely a projected sphere) with a radius that is equal to the distance of the component to the core. Deviations between epochs along each of their circles are then not taken into account, since only the radial distance matters. However, with this method it can be easily determined whether a component is moving away or toward the core. A general approach to estimate the uncertainty is to take half of the major axis as an error. However, the major axis is not a measure of the position of a component, but rather of its actual detected size. Additionally, in some sources the component size can change drastically due to, for instance, faintness. This results in either over- or underestimation of the error for certain epochs, leading to them being weighted to heavily or not enough. To compensate for that, the resolution given by half of the minor axis of the beam can be used as $\sigma_{\mathrm{pos}} = \sqrt{(\theta_{\mathrm{maj}}/2)^2 + (b_{\mathrm{min}}/2)^2}$. However, this in return leads to a gross overestimation of the uncertainty, making the errors several times higher than the best values. Instead, only the statistical deviation of the positions is used in an unweighted linear regression here. For sources with less than 4 identifications, no fit is performed since the data coverage is deemed as insufficient. Figure 3.31 shows the fitting result for PKS 0625−354 as an example and the others are shown in Appendix C. The resulting velocities along with the used redshift are all listed in Tab. 3.2.

The second method of determining the apparent velocity is to perform two linear regressions on the x- and y-distances to the core separately, labelled as $v_{\mathrm{app},x}$ and $v_{\mathrm{app},y}$. The total apparent velocity is then simply computed as the norm of the two values as $v_{\mathrm{app}} = \sqrt{v_{\mathrm{app},x}^2 + v_{\mathrm{app},y}^2}$. The advantage here is that the scattering along the x- and y-directions are also taken into account rather then just to focus on radial distance. Furthermore, this method allows for independent movement in these directions instead

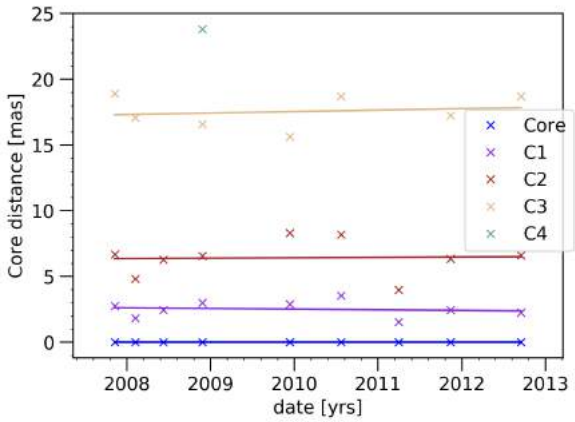

Figure 3.31.: Distance to the core plotted vs time for PKS 0625−354. No uncertainties are given due to the reasons mentioned in the section. The solid lines are computed from unweighted linear regression.

of solely focusing on straight radial motion. On the other hand, since the norm is computed, the apparent velocities are always positive. Thus, no distinction between forward- or backflow can be made from these values alone. Exemplary plots from PKS 0625−354 are shown in Fig. 3.32 and the remaining plots are listed in Appendix C. Table 3.3 lists all computed apparent velocities for each source.

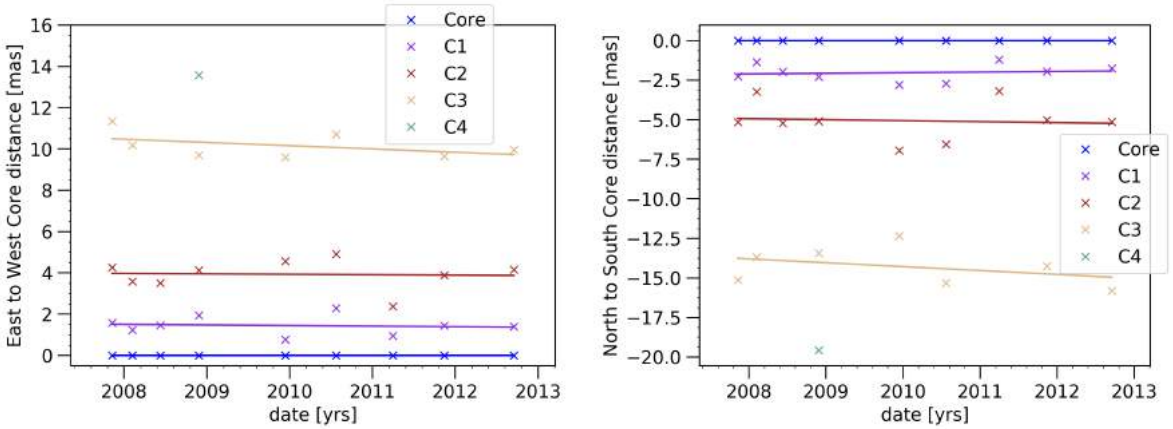

Figure 3.32.: Separate x- and y-distance to the core plotted vs time for PKS 0625−354. No uncertainties are given due to the reasons mentioned in the section. The solid lines are computed from unweighted linear regression.

When comparing the computed values, the vectorial ones are generally higher since they allow for more movement along the non-radial line to the core. However, all of the computed values agree within their respective uncertainties when the modulus is taken for the negative apparent velocities with the radial method. In general, if non-radial movement is allowed within the assumptions, the vectorial method should yield more accurate results. This is especially true for sources like PKS 2155−304, where

Table 3.2.: Apparent jet component velocities from linear regression of the core-distance over time.

Source Name	Label	v_{app}[a] [mas/yr]	β_{app}[a]	z[b]
PKS 1440−389	C1	-0.003 ± 0.095	-0.03 ± 0.87	0.176
PKS 0447−439	C1	0.43 ± 0.19	4.9 ± 2.2	0.14
PKS 2005−489	C1	0.05 ± 0.16	0.26 ± 0.74	0.071
	C3	0.67 ± 0.55	3.2 ± 2.6	0.071
PKS 2155−304	C1	0.75 ± 0.78	5.7 ± 6.0	0.116
	C2	0.86 ± 0.41	6.6 ± 3.1	0.116
	C3	-0.23 ± 0.19	-1.8 ± 1.4	0.116
PKS 0625−354	C1	-0.05 ± 0.13	-0.18 ± 0.49	0.055
	C2	0.03 ± 0.30	0.11 ± 1.1	0.055
	C3	0.11 ± 0.30	0.4 ± 1.1	0.055

Note: [(a)] Apparent velocity given in mas/yr and in units of c.
[(b)] Redshift used for the calculations.

jet-bending can be seen on various wavelengths.

For the radial method, most components are stationary within their given errors and at best only slightly superluminal. The only non-stationary components with superluminal apparent speeds are C1 in PKS 0447−439 with $(4.9 \pm 2.2)c$ and C2 in PKS 2155−304 with (6.7 ± 3.2). C3 in PKS 2155−304 is also superluminal and actually moving towards the core with $(-1.8 \pm 1.4)c$, but is potentially subluminal within its error. In PKS 2005−489, the component C3 appears to be moving at slightly superluminal speed, but since the modelled jet region is very diffuse, this should be interpreted as a very rough approximation to the bulk motion of said region. It should be noted that the errors are very large and indicate a lot of scattering when determining the component positions. The uncertainty can be hopefully restricted in the future with more and better data.

A kinematic analysis on PKS 0625−354 and PKS 2005−489 has been performed previously in Trüstedt (2013). His model for PKS 0625−354 is virtually the same, with two components close to the core and a diffuse region further downstream. The biggest difference lies in this more distant, diffuse feature, which was imaged to be more extended in Trüstedt (2013) compared to this thesis. This leads to generally larger component sizes and varying distances. Additionally, the diffuse region in November 2008 was modelled with only one component in Trüstedt (2013), compared to the two components used here, leading to a more distant position. Despite these only minor differences, the computed apparent speeds are much larger in Trüstedt (2013) and do not agree with the values presented here. This is mainly due to the fact that the last two epochs there, i.e. December 2009 and July 2010, actually seem to be outliers, since their distances to the core are the largest in all epochs. The three new epochs then "pull" the resulting

Table 3.3.: Apparent jet component velocities from separate linear regression of the x- and y-core-distance over time and subsequent norm computation.

Label	$v_{\mathrm{app},x}$ [a] [mas/yr]	$v_{\mathrm{app},y}$ [a] [mas/yr]	v_{app} [a] [mas/yr]	β_{app} [a]	z [b]
PKS 1440−389					
C1	0.085 ± 0.048	-0.07 ± 0.11	0.108 ± 0.080	0.99 ± 0.73	0.176
PKS 0447−439					
C1	-0.055 ± 0.071	0.47 ± 0.22	0.48 ± 0.22	5.4 ± 2.5	0.14
PKS 2005−489					
C1	-0.02 ± 0.14	-0.063 ± 0.080	0.066 ± 0.088	0.31 ± 0.41	0.071
C3	0.02 ± 0.39	-0.90 ± 0.46	0.90 ± 0.46	4.3 ± 2.2	0.071
PKS 2155−304					
C1	0.96 ± 0.78	-0.10 ± 0.44	0.96 ± 0.77	7.4 ± 6.0	0.116
C2	0.94 ± 0.32	-0.37 ± 0.31	1.02 ± 0.32	7.8 ± 2.5	0.116
C3	-0.05 ± 0.29	0.21 ± 0.18	0.22 ± 0.19	1.7 ± 1.4	0.116
PKS 0625−354					
C1	-0.03 ± 0.10	0.04 ± 0.12	0.05 ± 0.11	0.18 ± 0.41	0.055
C2	-0.02 ± 0.16	-0.06 ± 0.27	0.07 ± 0.26	0.24 ± 0.96	0.055
C3	-0.16 ± 0.14	-0.25 ± 0.27	0.29 ± 0.24	1.07 ± 0.89	0.055

Note: [a] Apparent velocities along the x- and y-axes as well as the norm given in mas/yr and the norm additionally given in units of c.
[b] Redshift used for the calculations.

linear fit down to slower apparent speeds. As a comparison, a linear fit was performed for the first six epochs imaged in this thesis and are shown in Fig. 3.33. The computed speeds are then $\beta_{\mathrm{app,C1}} = 1.50 \pm 0.65$, $\beta_{\mathrm{app,C2}} = 3.7 \pm 1.2$ and $\beta_{\mathrm{app,C3}} = -0.7 \pm 2.5$. The apparent speeds for C1 and C2 now agree well with the apparent speeds listed in Trüstedt (2013). The discrepancy for C3 however illustrates the difficulty of precisely modeling diffuse regions, to reach consistent models on independent works since the component positions are the only big differences in the models, while the flux density values are largely the same. In the case of PKS 2005−489 a similar argument can be made, since the diffuse region is modelled with two components mostly, so a comparison is difficult here. However, the apparent speed of the innermost component agrees with the result from Trüstedt (2013) within the uncertainties.

The vectorial method results in generally higher apparent velocities since the motion along both directions is taken into account. This can affect the resulting velocities greatly, since now, for instance, C1 in PKS 1440−389 is non-stationary with an apparent speed of (0.99 ± 0.73), but is still subluminal. This could stem from some jet-bending along the motion of C1, where its distance to the core does not change significantly. This, in turn, implies a very low inclination angle, where the component would cross the

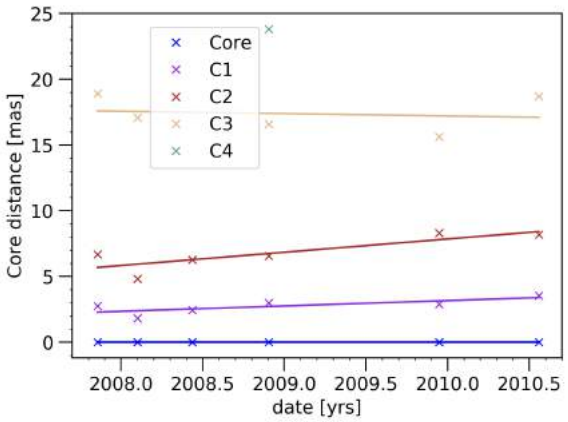

Figure 3.33.: Distance to the core plotted vs time for the first six epochs of PKS 0625−354 as a comparison to citettrüst-edt13. No uncertainties are given due to the reasons given in the text.

line of sight, but appear to have a constant distance to the core. The same applies to C1 in PKS 2155−304 with $(7.4 \pm 6.0)c$, now only allowing down to subluminal motion, and C3 in PKS 0625−354 with $(1.07 \pm 0.89)c$, being slightly superluminal. Additionally, the uncertainty is lowered with this method since the apparent velocity is computed by two fitted values instead of only one linear regression.

3.5. Discussion

3.5.1. Jet-bending in PKS 2155−304

PKS 2155−304 is an interesting object since it features the most rapid variability in upper wavelengths in the entire sample and even shows some clear variability in its radio flux density as the only source in the sample. Furthermore, its radio morphology changes the most throughout all epochs, where the jet is clearly pointed to the southeast for the first few epochs, but is instead propagating south in the last epoch. Unfortunately, the data coverage shows large gaps between the last three epochs, where the change of this jet direction would have been visible. However, the intermediate epochs feature this component, C3, south of the core even despite a southeastern jet. Additionally, the linear fit suggests that C3 is moving towards the core, indicating the possibility of jet-bending at this frequency.

Previous results by Piner, Pant, and Edwards (2010) already featured a high degree of jet-bending in PKS 2155−304 at 43 GHz. The jet started out toward the southwest and bent toward the southeast with a bending angle of $\sim 75\,^\circ$ during its propagation. Since in this paper three out of six of their sources, namely PKS 2155−304, Mrk 501 and 1ES 1959+650, featured jet-bending, they established this as a common property of TeV blazars. Furthermore, the large-scale structure of PKS 2155−304 suggests even more bending, since observations with the GMRT (Pandey-Pommier et al. 2016) show structures toward the northeast and -west. Further GMRT observations were analyzed

in Seeg (2017), where a brighter structure was found to the northwest. In this work jet-bending for PKS 2155−304 was also proposed to explain the discrepancy between the southeastern jet on VLBI-scales and the northwestern feature on larger scales. Furthermore, it was proposed that at different frequencies different sections of the jet are observed, essentially sampling the 3D-morphology of the source's jet.

With all of this taken into account, it seems logical that the jet of PKS 2155−304 would also feature some bending at 8.4 GHz. Two of the components, C1 and C2, are propagating toward the southeast in roughly the same direction, whereas C3 is directed north, toward the core. One possibility would be that the jet starts out south of the core, reaching to the position of C3 with an unknown previous jet, starting out at a position angle of $\sim -178\,^\circ$ and propagating toward the core. At some point close to C1 the jet would then bend to reach the position angle of C1 to roughly $\sim 135\,^\circ$, resulting in a jet-bending angle of $\sim 47\,^\circ$. Since Piner, Pant, and Edwards (2010) featured a higher jet-bending angle, this result is on a reasonable scale. It should be noted that this is the projected bending angle and should be much lower when deprojecting it from a small viewing angle, similar to what was proposed in Seeg (2017).

3.5.2. Inclination of PKS 0625−354

PKS 0625−354 is a peculiar object since its morphology clearly resembles that of a FR 1 radio galaxy with a bright core and jet and diffuse lobes on larger scales, but its power-law spectrum resembles that of a BL Lac object instead (Wills et al. 2004). The unification model suggests a clear connection between BL Lac objects and FR 1 radio galaxies, where they are just rotated counterparts to each other. For BL Lacs, the observer looks directly into the jet under a low inclination angle, but views a FR 1 radio galaxy edge-on instead. So there must clearly be objects with intermediate inclination angles, which could possibly share traits of both classes of AGN. This can be studied in the case of PKS 0625−354, by computing its inclination angle directly using the flux density ratio of its jet and counter-jet as stated in Eq. 1.3.17. Since no counter-jet is visible, the source shows some degree of Doppler boosting and de-boosting, so it can already be stated that this source is not viewed edge-on. The counter-jet is then approximated by 5 times of the noise given in Tab. B.5 for each epoch. The full flux density of the jet is approximated by summing the flux density values fitted for C1 and C2 given in Tab. B.10. C3 is left out since it is a more distant component and since it either does not appear or is not fitted in some epochs. Solving Eq. 1.3.17 for the inclination angle ϕ yields

$$\phi = \arccos\left[\frac{1}{\beta}\frac{\left(\frac{S_{\mathrm{jet}}}{S_{\mathrm{counter}}}\right)^{\frac{1}{3.\alpha}} - 1}{\left(\frac{S_{\mathrm{jet}}}{S_{\mathrm{counter}}}\right)^{\frac{1}{3.\alpha}} + 1}\right]. \tag{3.5.1}$$

By letting $\beta \to 1$, an upper limit for ϕ can be computed. Wills et al. (2004) fitted the optical spectrum of PKS 0625−354 with $\alpha = -1.15$, so this value is used as a rough estimate for the calculations. For each epoch, the upper limit to the inclination angle was computed with the given values and Eq. 3.5.1. Finally, these results were averaged to $\phi_{\max} = 58.37 \pm 0.67\,^\circ$ using standard error, leading to an upper limit of

$$\phi < 59\,^\circ. \tag{3.5.2}$$

Venturi et al. (2000) computed an upper limit using the flux density ratio method, too, and gained an upper limit of 61 °. A different method yielded an even lower limit of 43 °. All these results confirm that PKS 0625−354 is not viewed under an edge-on inclination angle, and is indeed situated at an intermediate position between a BL Lac object and a FR 1 radio galaxy.

3.5.3. Jet Velocities in the context of the Doppler Crisis

Observations of blazars, most notably of high frequency peaked BL Lac objects, in the very high energy regime yield rapid variability on various timescales. The most prominent objects here are, among others, Mrk 421, Mrk 501 and PKS 2155−304, where the latter features variability of down to minutes. Such rapid variability implies a high degree of Doppler boosting, leading to a bulk Lorentz factor of $\Gamma \sim 50$ (Ghisellini and Tavecchio 2008).

On the other hand, kinematic studies with radio VLBI observations yield apparent velocities at mostly subluminal or only slightly superluminal values (Piner and Edwards 2016), leading to even lower, deprojected velocities. For instance, Piner, Pant, and Edwards (2010) find values of $(0.72 \pm 0.05)c$ and $(5.48 \pm 3.59)c$ in the case of PKS 2155−304 at 43 GHz. The Doppler crisis or bulk Lorentz factor crisis is the term used for this discrepancy of velocities at different wavelengths. The radio studies were almost solely performed by this group, so it is reasonable to perform an independent study to check if similar slow apparent velocities can be found. Additionally, the previous studies consist of mostly northern sources of (e.g. from the MOJAVE sample), so an extension to sources on the southern hemisphere is reasonable.

Four of the five investigated sources, PKS 1440−389, PKS 0447−439, PKS 2005−489 and PKS 2155−304, are classified as HBLs, while PKS 0625−354 appears to be an intermediate object between an HBL and a FR 1 radio galaxy. All sources are detected in the VHE regime by H.E.S.S., although not all of them feature variability and the bulk Lorentz factor was only computed for PKS 2155−304. The TANAMI VLBI data analyzed in this thesis yields low apparent velocities for all sources. PKS 2005−489 features a stationary component and a diffuse region which seems to be propagating at slightly superluminal apparent speed. PKS 1440−389 and PKS 0625−354 feature only stationary or one slightly superluminal component, depending on the method of fitting used. PKS 0447−439 and PKS 2155−304 feature the fastest components with

almost $8c$ in the case of the latter. However, the computed values are still lower than what is usually detected in BL Lac objects, where apparent speeds of 10s of c can be found (e.g. Piner et al. 2006). However, even the highest velocities do not contradict the apparent speeds computed by Piner and Edwards (2016) and rather confirm the previously established results. The statistics shown in Piner and Edwards (2016) can therefore be extended with the results of this sample, shown in Fig. 3.34. As in Piner and Edwards (2016), the peak jet speeds of each source are used for the histogram. The tail is extended with the fast moving component C2 in PKS 2155−304. Since the source is also in their sample, it is possible that it is counted twice in this histogram, since they did not give exact details on the data used for their histogram. In the case of PKS 2005−489, only the slower component is considered since the diffuse jet is not well fitted.

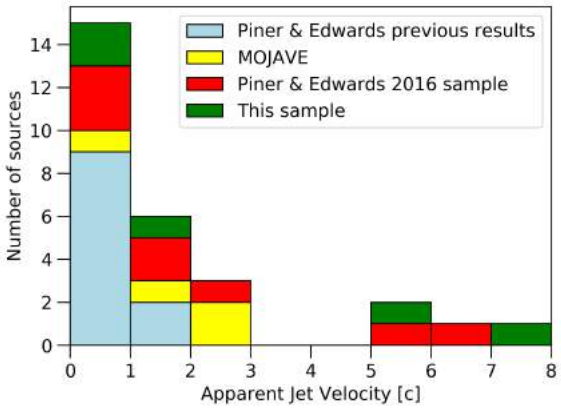

Figure 3.34.: Histogram of the peak apparent jet velocities. The green sources are from this sample and the others are reproduced from Piner and Edwards (2016). The tail is extended with PKS 2155−304 with $(7.8 \pm 2.5)c$.

The Lorentz factor computed for PKS 2155−304 of $\Gamma \sim 50$ implies an intrinsic jet velocity of $\beta \sim 0.9998$. With a known apparent speed β_{app}, Eq. 1.4.5 can be solved for the inclination angle ϕ. The peak apparent speed of C2 allows for moderate inclination angles of $\sim 14\,^\circ$. However, the low apparent speed of C3 yields a larger angle of $\sim 60\,^\circ$, which contradicts both the observed morphology as well as the high degree of Doppler boosting observed in the γ-rays. Much like in Piner and Edwards (2016), the only other solution would imply an inclination angle of $\phi \ll 1\,^\circ$. For simplicity, an angle of $\phi = 0.01\,^\circ$ is assumed in the following. The strongest peak of PKS 2155−304 in Seeg (2017) is located at ~ 14 as, corresponding to ~ 37 kpc at $z = 0.116$. Using the given ϕ, the deprojected size then becomes ~ 236 Mpc. This, of course, is only a rough estimate, especially considering the jet-bending in this source, potentially leading to differing inclination angles. However, this is a huge linear size for any jet and thus the assumption of low angles is unphysical. Additionally, all observed brightness temperatures are below or only very slightly above the equipartition limit of 10^{11} K, meaning that for the radio emission there is only little Doppler boosting present. The aforementioned conclusion is that the radio and γ-ray emission do not stem from a single-zone jet, but must rather be explained by regions with different properties within the jet.

Several approaches utilizing numerical simulations are present in the context of the Doppler crisis. Ghisellini, Tavecchio, and Chiaberge (2005) propose a structure consisting of a fast inner spine responsible for the γ-rays and a slow outer sheath, which acts as the synchrotron emitter. In this model, both regions see the photons of the other frame as blueshifted, increasing the inverse Compton emission in both regions. Limb-brightnening observed in Mrk 421 by Piner, Pant, and Edwards (2010) would be a property arising from such a structure. Other models include a velocity structure along the line of the jet (Georganopoulos and Kazanas 2003), where deceleration along the flow leads to regions of different velocities and therefore beaming between the different frames, reaching energies up to TeV. This model also helps the BL Lac - FR 1 unification scheme, since the debeamed BL Lac flux densities are not significantly lower than the observed FR 1 flux densities. Several other models include scenarios with fast moving blobs within the jet (Tavecchio et al. 2011), turbulent sub-regions leading to variability in a jet (Marscher 2014), small active regions, which occasionally point at the observer (Ghisellini and Tavecchio 2008) as well as plasmoids driven by magnetic reconnection processes (Giannios 2013).

4. Summary and Outlook

In this thesis several epochs of a sample of five TANAMI VLBI sources at 8.4 GHz were imaged and fitted with Gaussian model components to perform a kinematic analysis. With the exception of Centaurus A, the sample consists of all sources of the TANAMI sample which were detected in TeV energies and are bright enough to be observed with VLBI, namely PKS 1440−389, PKS 0447−439, PKS 2005−489, PKS 2155−304 and PKS 0625−354. All sources are classified as high frequency peaked BL Lacs, although PKS 0625−354 is also potentially a FR 1 radio galaxy.

Previous studies of TeV blazars by Piner & Edwards computed the apparent jet velocities of these types of sources. Their results showed stationary and slow moving jets, which are at most only slightly superluminal, with the fastest object being at $\sim 6c$. This is in contrast to variability studies of the VHE emission, yielding very high Lorentz factors of $\Gamma \sim 50$, needing unreasonably low inclination angles to work with a single zone model. The discrepancy of apparent vs. intrinsic speed is known as the Doppler crisis and while there are several approaches with multi-zone jets to properly model the emission, it stands to reason to perform an independent study to confirm or deny the slow moving radio jets in TeV sources.

This was the focus of this thesis. The provided data covered a time range of roughly 2007 to 2013, with six to nine epochs per source. All sources featured core-dominated emission and compact and collimated parsec-scale jets, propagating away from the core in a straight line. The jet of PKS 2005−489 is well defined in the inner region, but shows more complex and diffuse structure further out, which could not be modeled well. Additionally, the jet of PKS 2155−304 changes drastically between epochs and shows some degree of jet-bending, also seen on other frequencies. The jet-to-counterjet ratio was used to constrain the inclination angle to PKS 0625−354 to $\phi < 59\,^\circ$, classifying it as an intermediate object between a BL Lac and a FR 1 object. Furthermore, all sources showed only moderate brightness temperatures, implying small Doppler boosting factors. Finally, the apparent velocities computed with linear regression showed mostly stationary or subluminal component speeds. Only PKS 0447−439 and PKS 2155−304 featured slightly superluminal apparent motion with $(5.4 \pm 2.5)c$ and $(7.8 \pm 2.5)c$ respectively. The tail of the distribution is now extended by the fast moving component of PKS 2155−305 to higher velocities. Overall, the previous results by Piner & Edwards were positively confirmed, extending their previous statistic of TeV blazars.

The only source of the sample to feature sufficient analysis in the TeV range is PKS 2155−304. None of the other sources had bulk Lorentz factors derived from flux density variability. Additionally, the data coverage was sparse on some time intervals and the

computed apparent velocities show big uncertainties. These are due to a high degree of scattering in the component positions from bad data quality as well as a small number of epochs to better constrain this statistical error. Hopefully, future observations will allow to derive intrinsic Lorentz factors from the TeV data for all sources as well as new epochs to better constrain the apparent velocities in the radio frequencies. Finally, more HBLs need to be searched for to further confirm that the slow moving radio jets are a common feature of these types of AGN and to further establish multi-zone jet models.

Bibliography

Aartsen, M. G., K. Abraham, M. Ackermann, et al. (2016). *Phys. Rev. Lett.* 117 (7), p. 071801.

Abdo, A. A., M. Ackermann, M. Ajello, et al. (2010a). *Science* 328.5979, pp. 725–729.

Abdo, A. A. et al. (2010b). *The Astrophysical Journal* 716, p. 30.

Ackermann, M. et al. (2015a). *The Astrophysical Journal* 810.

Ackermann, M., M. Ajello, W. B. Atwood, et al. (2015b). *The Astrophyiscal Journal* 810, 14, p. 14.

Ackermann, M. et al. (2016). *The Astrophysical Journal Supplement Series* 222, 5, p. 5.

Aharonian, F., A. G. Akhperjanian, K.-M. Aye, et al. (2005). *Astronomy and Astrophysics* 436, p. L17.

Aharonian, F. et al. (2007). *The Astrophysical Journal* 664, p. L71.

Aharonian, F. et al. (2009). *The Astrophysical Journal* 696, p. L150.

Antonucci, R. (1993). *Annual review of astronomy and astrophysics* 31, p. 473.

Bai, J. M. and M. G. Lee (2001). *The Astrophysical Journal* 548, p. 244.

Begelman, M. C., A. C. Fabian, and M. J. Rees (2008). *MNRAS* 384, p. L19.

Blandford, R. D. and A. Königl (1979). *The Astrophysical Journal* 232, p. 34.

Böck, M. et al. (2016). *Astronomy and Astrophysics* 590, A40, A40.

Bolton, J. G., M. E. Clarke, and R. D. Ekers (1965). *Australian Journal of Physics* 18, p. 627.

Born, M. and E. Wolf (1999). 7. ed. Cambridge: Cambridge University Press.

Bridle, A. H. et al. (1994). *Astron. J.* 108.766.

Brodie, J. P. et al. (1983). *Bulletin of the American Astronomical Society*. Vol. 15. BAAS. United States: American Astronomical Society, p. 956.

Burke, B. F. and F. Graham-Smith (2010). 3. ed. Cambridge: Cambridge Univ. Press.

Camenzind, M. (2007). Astronomy and astrophysics library. Berlin: Springer.

Carini, M. T. and H. R. Miller (1992). *The Astrophysical Journal* 385, p. 146.

Chadwick, P. M. et al. (1999). *The Astrophysical Journal* 513, p. 161.

Clark, B. G. (1980). *Astronomy and Astrophysics* 89, p. 377.

Cornwell, T. J. (1989). *Science* 245, p. 263.

Cornwell, T., R. Braun, and D. S. Briggs (1999). *Synthesis Imaging in Radio Astronomy II*. Ed. by G. B. Taylor, C. L. Carilli, and R. A. Perley. Vol. 180. Astronomical Society of the Pacific Conference Series. San Francisco, Calif.: Astronomical Society of the Pacific, p. 151.

Cornwell, T. and E. B. Fomalont (1999). *Synthesis Imaging in Radio Astronomy II*. Ed. by G. B. Taylor, C. L. Carilli, and R. A. Perley. Vol. 180. Astronomical Society of the

Pacific Conference Series. San Francisco, Calif.: Astronomical Society of the Pacific, p. 187.
Costamante, L. et al. (2008). *International Cosmic Ray Conference* 3, p. 945.
Craig, N. and A. Fruscione (1997). *The Astronomical Journal* 114, p. 1356.
Dominici, T. P., Z. Abraham, and A. L. Galo (2006). *Astronomy and Astrophysics* 460, p. 665.
Dominici, T. P. et al. (2004). *The Astronomical Journal* 128, p. 47.
Dyrda, M. et al. (2015). *ArXiv e-prints*. arXiv: 1509.06851.
Edwards, P. G. and B. G. Piner (2002). *The Astrophysical Journal Letters* 579.2, p. L67.
Falomo, R., J. E. Pesce, and A. Treves (1993). *Astrohysical Journal Part 2 - Letters* 411, p. L63.
Falomo, R. et al. (1987). *Astrophysical Journal, Part 2 - Letters to the Editor* 318, p. L39.
Fanaroff, B. L. and J. M. Riley (1974). *MNRAS* 167, 31P.
Fichtel, C. E. et al. (1994). *The Astrophysical Journal Supplement Series* 94, p. 551.
Fomalont, E. B. et al. (2000). *The Astrophysical Journal Supplement Series* 131, p. 95.
Foschini, L. et al. (2011). *Astronomy and Astrophysics* 530.
Fumagalli, M. et al. (2012). *Astronomy and Astrophysics* 545, A68, A68.
Georganopoulos, M. and D. Kazanas (2003). *The Astrophysical Journal Letters* 594.1, p. L27.
Ghisellini, G. (1999). *The BL Lac Phenomenon*. Ed. by L. O. Takalo and A. Sillanpää. Vol. 159. ASP conf. series 311. San Francisco, Calif.: Astronomical Society of the Pacific.
Ghisellini, G. and F. Tavecchio (2008). *MNRAS* 386, p. L28.
Ghisellini, G., F. Tavecchio, and M. Chiaberge (2005). *Astronomy and Astrophysics* 432, p. 401. eprint: astro-ph/0406093.
Ghisellini, G. et al. (2017). *MNRAS* 469, p. 255.
Giannios, D. (2013). *MNRAS* 431, p. 355.
Giommi, P. et al. (2005). *Astronomy and Astrophysics* 434, p. 385.
Giroletti, M. et al. (2004). *The Astrophysical Journal* 600.1, p. 127.
Govoni, F. et al. (2000). *Astronomy and Astrophysics Supplement Series* 143, p. 369.
Greisen, E. W. (2003). *Information Handling in Astronomy - Historical Vistas* 285, p. 109.
Heidt, J. and S. J. Wagner (1998). *Astronomy and Astrophysics* 329, p. 853.
Henri, G. and L. Saugé (2006). *The Astrophysical Journal* 640, p. 185.
H.E.S.S. Collaboration et al. (2010a). *Astronomy and Astrophysics* 511, A52, A52.
H.E.S.S. Collaboration et al. (2010b). *Astronomy and Astrophysics* 520, A83, A83.
H.E.S.S. Collaboration et al. (2011). *Astronomy and Astrophysics* 533, A110, A110.
H.E.S.S. Collaboration et al. (2013). *Astronomy and Astrophysics* 552, A118, A118.
H.E.S.S. Collaboration et al. (2017). *Astronomy and Astrophysics* 600, A89, A89.
Högbom, J. A. (1974). *Astronomy and Astrophysics Supplement* 15, p. 417.
Jones, D. H. et al. (2009). *MNRAS* 399, p. 683.

Kadler, M., R. Ojha, and TANAMI Collaboration (2015). *Astronomische Nachrichten* 336, p. 499.
Kadler, M. et al. (2016). *Nature Physics* 12, p. 807.
Kellermann, K. I. et al. (1989), p. 1195.
Kembhavi, A. K. and J. V. Narlika (1999). Cambridge: Cambridge University Press.
Königl, A. (1981). *The Astrophysical Journal* 243.700.
Kovalev, Yuri Y. et al. (2005). *Astronomical Journal* 130, p. 2473.
Krauß, F. et al. (2016). *Astronomy and Astrophysics* 591, A130, A130.
Krawczynski, H. et al. (2004). *´The Astrophysical Journal* 601, p. 151.
Krolik, J. H. (1999). Princeton: Princeton University Press.
Kuehr, H. et al. (1981). *Astronomy and Astrophysics Supplement Series* 45.
Landt, H. (2012). *Monthly Notices of the Royal Astronomical Society: Letters* 423.1, pp. L84–L86.
Landt, H. and H. E. Bignall (2008). *MNRAS* 391, p. 967.
Lin, Y. C., D. L. Bertsch, S. D. Bloom, et al. (1997). *AIP Conference Proceedings* 410.1, p. 1371.
Lister, M. and the MOJAVE Collaboration (2016). *Galaxies* 4.3.
Mannheim, K. (1993). *Astronomy and Astrophysics* 269.67.
Marscher, A. P. (2014). *The Astrophysical Journal* 780, p. 87.
Morganti, R., N. E. B. Killeen, and C. N. Tadhunter (1993). *MNRAS* 263, p. 1023.
Müller, C. (2014). PhD thesis. Institut für Physik und Astronomie, Julius-Maximilians-Universität Würzburg.
Müller, C. et al. (2011). *Astronomy and Astrophysics* 530, L11, p. L11.
Müller, C. et al. (2017). *Astronomy and Astrophysics*.
Muriel, H. et al. (2015). *Astronomy and Astrophysics* 574, A101, A101.
Nesci, R. et al. (2013). *Astronomy and Astrophysics* 555, A2, A2.
Ojha, R., A. L. Fey, P. Charlot, et al. (2005). *Astronomical Journal* 130.2529.
Ojha, R. et al. (2010a). *Astronomy and Astrophysics* 519, A45.
Ojha, R. et al. (2010b). *Proceedings of the Workshop "Fermi meets Jansky - AGN in Radio and Gamma-Rays"*. Bonn, Germany: MPIfR.
Padovani, P. and P. Giommi (1995). *The Astrophysical Journal* 444, p. 567.
Pandey-Pommier, M. et al. (2016). *SF2A-2016: Proceedings of the Annual meeting of the French Society of Astronomy and Astrophysics*. Ed. by C. Reylé et al., p. 373. arXiv: 1610.05650.
Perley, R. A., A. G. Willis, and J. S. Scott (1979). *Nature* 281.437.
Perlman, E. S. et al. (1998). *The Astronomical Journal* 115, p. 1253.
Perlman, E. S. et al. (1999). *Astrophysical Journal, Part 2 - Letters to the Editor* 523, p. L11.
Peterson, B. M. et al. (2016). *The Astrophysical Journal* 613, p. 682.
Piner, B. G. and P. G. Edwards (2004). *The Astrophysical Journal* 600.1, p. 115.
– (2005). *The Astrophysical Journal* 622.1, p. 168.
– (2014). *The Astrophysical Journal* 797.1, p. 25.

Piner, B- G., N. Pant, and P. G. Edwards (2008). *The Astrophysical Journal* 678.1, p. 64.
Piner, B. G., N. Pant, and P. G. Edwards (2010). *The Astrophysical Journal* 723.2, p. 1150.
Piner, B. G. et al. (1999). *The Astrophysical Journal* 525.1, p. 176.
Piner, B. G. et al. (2006). *The Astrophysical Journal* 640, p. 196.
Piner, B. G. et al. (2009). *The Astrophysical Journal* 690, p. L31.
Piner, B. and P. Edwards (2016). *Galaxies* 4, p. 44.
Prandini, E., G. Bonnoli, and F. Tavecchio (2012). *Astronomy and Astrophysics* 543, A111, A111.
Prestage, R. M. and J. A. Peacock (1983). *MNRAS* 204, p. 355.
Prokoph, H., Y. Becherini, M. Böttcher, et al. (2015). *ArXiv e-prints*. arXiv: 1509.03972.
Readhead, A. C. S. and P. N. Wilkinson (1978). *The Astrophysical Journal* 223, p. 25.
Rector, T. A. and E. S. Perlman (2003). *The Astronomical Journal* 126, p. 47.
Robson, I. (1996). New York: Wiley, Chichester: Praxix Publishing.
Rovero, A. C. et al. (2013). *ArXiv e-prints*. arXiv: 1307.6907.
Rybicki, G. B. and A. P. Lightman (1979). A Wiley-Interscience publication. New York: Wiley.
Sahu, S., B. Zhang, and N. Fraija (2012). *Physical Review D* 85.4.
Sambruna, R. M. et al. (1995). *The Astrophysical Journal* 449, p. 567.
Schneider, P. (2008). Berlin: Springer.
Schwab, F. R. (1980). *1980 International Optical Computing Conference I*. Ed. by W. T. Rhodes. Vol. 231. Proc S.P.I.E. Washington, D.C., United States, p. 18.
– (1984). *Astronomical Journal* 89, p. 1076.
Seeg, M. (2017). Bachelor's thesis.
Seyfert, C. K. (1943). *The Astrophysical Journal* 97, p. 28.
Shakura, N. I. and R. A. Sunyaev (1973). *Astronomy and Astrophysics* 24, p. 337.
Shaw, M. S. et al. (2013). *American Astronomical Society Meeting Abstracts #221*. Vol. 221. American Astronomical Society Meeting Abstracts, p. 103.01.
Shen, Z.-Q. et al. (1998). *The Astronomical Journal* 115, p. 1357.
Shepherd, M. C. (1997). *Astronomical Data Analysis Software and Systems VI*. Ed. by G. Hunt and H. Payne. Vol. 125. San Francisco, Calif.: Astronomical Society of the Pacific, p. 77.
Stocke, J. T. et al. (1992). *The Astrophysical Journal* 396, p. 487.
Tagliaferri, G. et al. (1991). *The Astrophysical Journal* 380, p. 78.
Tagliaferri, G. et al. (2001). *Astronomy and Astrophysics* 368, p. 38.
Tavecchio, F. (2006). *The Tenth Marcel Grossmann Meeting. On recent developments in theoretical and experimental general relativity, gravitation and relativistic field theories*. Ed. by M. Novello, S. Perez Bergliaffa, and R. Ruffini. 5 Toh Tuck Link, Singapore: World Scientific Publushing Co. Pre. Ltd., p. 512.
Tavecchio, F. et al. (2011). *Astronomy and Astrophysics* 534, A86.
Thompson, A. R., J. M. Moran, and G. W. Swenson (2001). New York: Wiley.
Tiet, V. C., B. G. Piner, and P. G. Edwards (2012). *ArXiv e-prints*. arXiv: 1205.2399.

Trussoni, E. et al. (1999). *Astronomy and Astrophysics* 348, p. 437.
Trüstedt, J. E. (2013). Master thesis.
Ulvestad, J. S., K. J. Johnston, and K. W. Weiler (1983). *The Astrophysical Journal* 266, p. 18.
Urry, C. M. and P. Padovani (1995). *Publications of the Astronomical Society of the Pacific* 107, p. 803.
Urry, C. M., P. Padovani, and M. Stickel (1991). *The Astrophysical Journal* 382, p. 501.
Venturi, T. et al. (2000). *Astronomy and Astrophysics* 363, p. 84.
Vestergaard, M. and B. M. Peterson (2006). *The Astrophysical Journal* 641, p. 689.
Vestrand, W. T., J. G. Stacy, and P. Sreekumar (1995). *Astrophysical Journal Letters* 454, p. L93.
Wall, J. V. and J. A. Peacock (1985). *MNRAS* 216, p. 173.
Wall, J. V. et al. (1986a). *MNRAS* 219, 23P.
Wall, J. V. et al. (1986b). *Quasars*. Ed. by G. Swarup and V. K. Kapahi. Vol. 119. IAU Symposium. Netherlands: Springer Netherlands, p. 59.
Wierzcholska, A. et al. (2015). *Astronomy and Astrophysics* 573, A69, A69.
Wills, K. A. et al. (2004). *MNRAS* 347, p. 771.
Zacharias, N. et al. (1999). *The Astronomical Journal* 118, p. 2511.
Zech, A. et al. (2011). *ArXiv e-prints*. arXiv: 1105.0840.
Zhang, Y. H. et al. (2002). *The Astrophysical Journal* 572, p. 762.
Zhang, Y. H. et al. (2006). *The Astrophysical Journal* 651, p. 782.

List of Figures

List of Tables

Acknowledgements

First of all, I want to thank Prof. Dr. Matthias Kadler who offered me the great opportunity to work in this interesting and intriguing field of astronomy and for integrating me into his work group. The deep discussions with him about both the analysis methods in radio astronomy and the underlying theoretical questions of AGN greatly helped me in understanding this field and enabled me to work independently on this project with discussions when needed. Finally, while I was always interested in astronomy, his great lectures are what instigated me to actually pursue working in this field. For this, I am deeply grateful.

In addition I would like to thank the chair of astronomy, with Prof. Dr. Karl Mannheim as its holder. Every member of the chair offers a welcoming attitude and is always open for interesting discussions.

Next, I want to thank Paul Ray Burd, Jonas Ringholz and Florian Rösch, who also work in the field of radio astronomy, who were always open for both questions regarding the specifics of the analysis software and intriguing discussions about AGN.

I also want to thank Michael Kreter, who provided me with the light curves as well as with great feedback, which helped improve this thesis.

Furthermore I'd like to thank all members of the TANAMI project for providing the data used in this thesis as well as its a priori calibration and especially Dr. Roopesh Ojha for his coordination., who, together with Prof. Dr. Matthias Kadler, is head of the project.

I would also like to express my deepest thanks to all members of my family, most importantly my parents and my sister. Without your constant confidence in me and your support, both practical and emotional, I would have never been able to come this far. Thank you all dearly.

Finally, I want to thank my girlfriend, who was a great source of motivation and comfort in the last year. We met each other when we were both in critical times of our education, but we stuck together and supported each other to make it this far. Thank you, my dear.

This research has made use of the NASA/IPAC Extragalactic Database (NED) which is operated by the Jet Propulsion Laboratory, California Institute of Technology, under contract with the National Aeronautics and Space Administration.

This research has made use of the Interactive Spectral Interpretation System (ISIS) (Houck and Denicola, 2000) This research has made use of a collection of ISIS scripts provided by the Dr. Karl Remeis observatory, Bamberg, Germany at
http://www.sternwarte.uni-erlangen.de/isis/

A. (u, v)-coverages

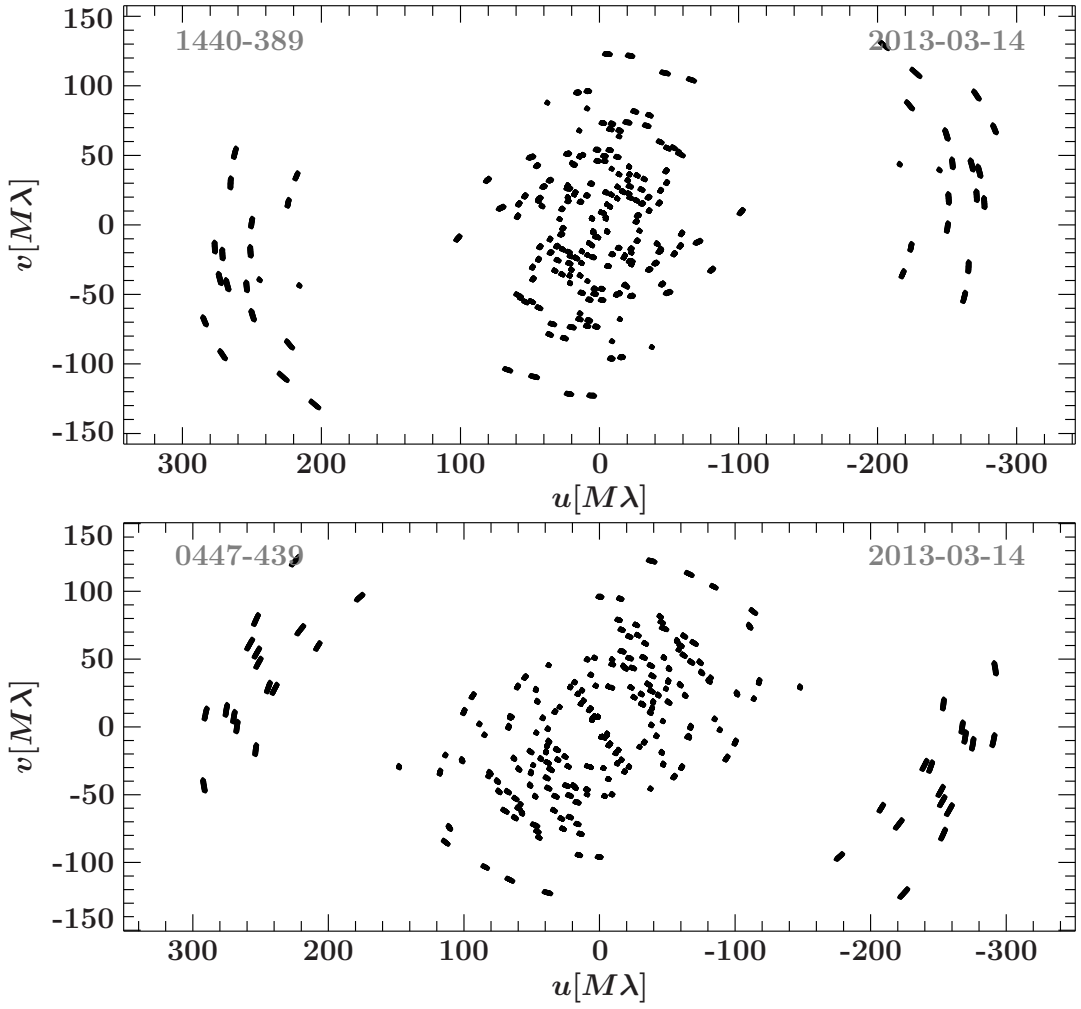

Figure A.1.: (u, v)-coverages of the most recent epoch for each source in the sample. Most of the other epochs show very similar coverages.

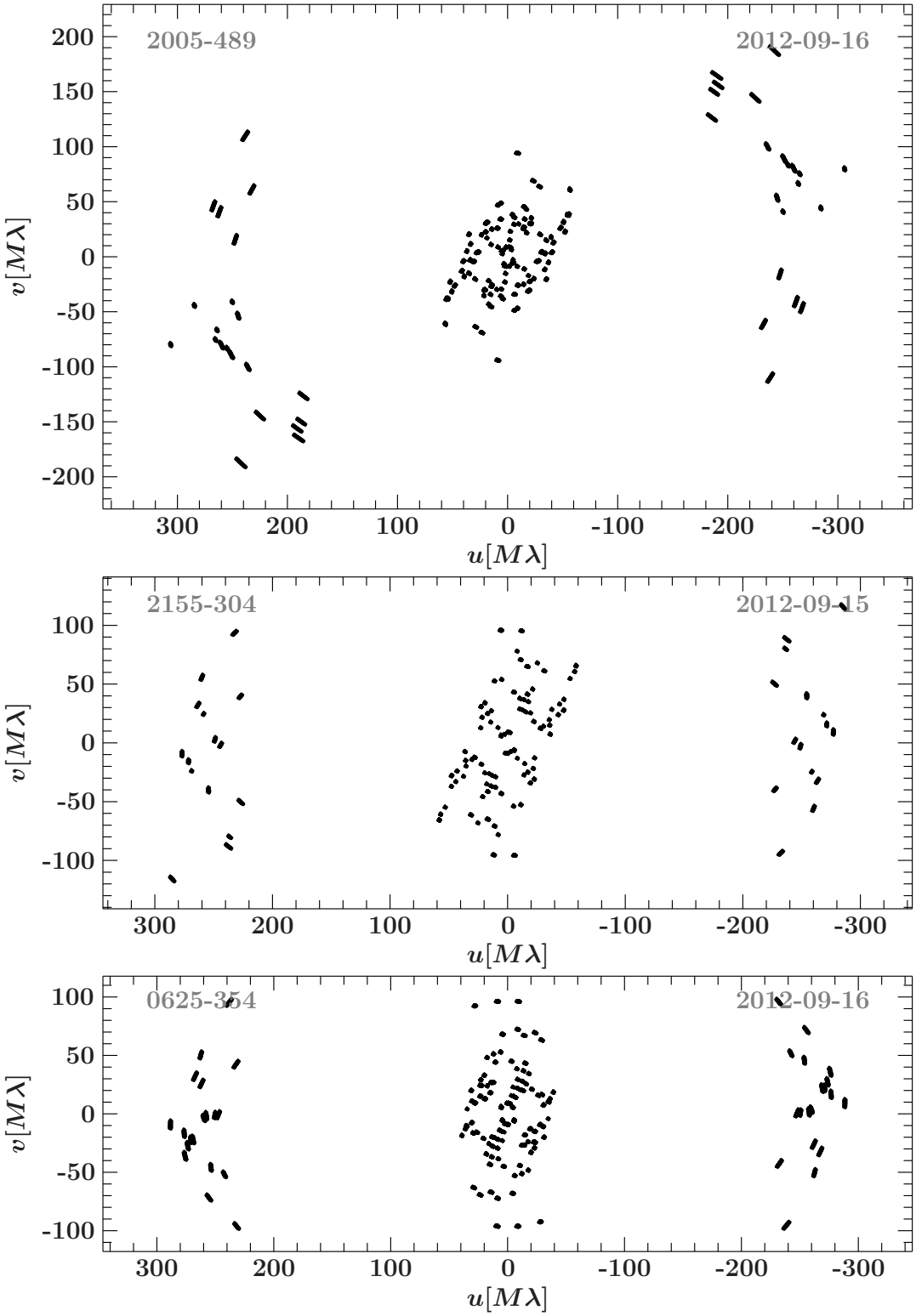

Figure A.2.: Continuation of Fig. A.1.

B. Imaging and Modelfit Parameters

Table B.1.: Image parameters for the TANAMI VLBI observations of PKS 1440−389 at 8.4 GHz.

Date [yyyy − mm − dd]	S_{tot} [a] [Jy]	S_{peak} [a] [Jy/beam]	σ [a] [mJy/beam]	b_{maj} [b] [mas]	b_{min} [b] [mas]	P.A. [b] [°]
2009-02-27	0.11	0.08	0.07	3.07	1.25	24.9
2010-03-12	0.08	0.07	0.03	4.41	3.56	80.8
2010-10-28	0.08	0.06	0.06	2.83	0.59	-0.6
2011-07-21	0.09	0.07	0.05	3.00	0.97	0.2
2012-04-27	0.08	0.07	0.05	3.32	2.66	19.8
2013-03-14	0.11	0.08	0.08	2.51	0.70	10.5

Note: [(a)] Total integrated and peak flux density as well as RMS of the 8.4 GHz image. [(b)] Major and minor axis as well as the position angle of the synthesized beam.

Table B.2.: Image parameters for the TANAMI VLBI observations of PKS 0447−439 at 8.4 GHz.

Date [yyyy − mm − dd]	S_{tot} [a] [Jy]	S_{peak} [a] [Jy/beam]	σ [a] [mJy/beam]	b_{maj} [b] [mas]	b_{min} [b] [mas]	P.A. [b] [°]
2009-02-27	0.12	0.09	0.07	2.54	1.23	38.5
2010-03-12	0.13	0.13	0.03	5.16	4.49	77.3
2010-10-28	0.13	0.10	0.04	3.28	0.70	-4.5
2011-07-21	0.11	0.09	0.05	2.56	0.76	0.0
2012-04-27	0.13	0.11	0.06	2.86	0.80	-0.3
2013-03-14	0.13	0.10	0.07	2.33	0.67	-5.7

Note: [(a)] Total integrated and peak flux density as well as RMS of the 8.4 GHz image. [(b)] Major and minor axis as well as the position angle of the synthesized beam.

Table B.3.: Image parameters for the TANAMI VLBI observations of PKS 2005−489 at 8.4 GHz.

Date [yyyy − mm − dd]	S_{tot}[a] [Jy]	S_{peak}[a] [Jy/beam]	σ[a] [mJy/beam]	b_{maj}[b] [mas]	b_{min}[b] [mas]	P.A.[b] [°]
2007-11-10	0.65	0.42	0.16	3.69	0.89	35.8
2008-03-28	0.72	0.40	0.35	3.01	0.74	-3.2
2008-08-08	0.88	0.63	0.28	3.71	2.64	-3.6
2009-02-23	0.84	0.46	0.20	2.27	0.72	35.0
2009-12-13	0.66	0.47	0.08	3.83	1.11	32.0
2010-07-24	0.62	0.44	0.24	4.26	2.08	23.5
2011-04-01	0.74	0.28	0.15	1.46	0.44	5.0
2011-11-13	0.56	0.27	0.17	1.86	0.53	7.1
2013-09-16	0.59	0.30	0.13	2.00	0.77	6.7

Note: (a) Total integrated and peak flux density as well as RMS of the 8.4 GHz image. (b) Major and minor axis as well as the position angle of the synthesized beam.

Table B.4.: Image parameters for the TANAMI VLBI observations of PKS 2155−304 at 8.4 GHz.

Date [yyyy − mm − dd]	S_{tot}[a] [Jy]	S_{peak}[a] [Jy/beam]	σ[a] [mJy/beam]	b_{maj}[b] [mas]	b_{min}[b] [mas]	P.A.[b] [°]
2008-03-28	0.48	0.38	0.09	3.82	0.60	1.1
2008-08-08	0.44	0.36	0.12	4.21	0.92	4.2
2009-02-27	0.36	0.32	0.12	2.74	1.02	6.7
2009-09-05	0.33	0.28	0.06	4.52	1.26	10.2
2010-03-12	0.24	0.20	0.05	4.48	3.35	67.6
2010-05-07	0.26	0.21	0.07	3.48	1.27	15.1
2011-08-13	0.35	0.30	0.12	2.77	1.41	18.2
2012-09-15	0.33	0.27	0.10	2.26	0.59	0.9

Note: (a) Total integrated and peak flux density as well as RMS of the 8.4 GHz image. (b) Major and minor axis as well as the position angle of the synthesized beam.

Table B.5.: Image parameters for the TANAMI VLBI observations of PKS 0625−354 at 8.4 GHz.

Date [yyyy − mm − dd]	S_{tot} [a] [Jy]	S_{peak} [a] [Jy/beam]	σ [a] [mJy/beam]	b_{maj} [b] [mas]	b_{min} [b] [mas]	P.A. [b] [°]
2007-11-10	0.37	0.30	0.12	2.83	0.89	4.9
2008-02-07	0.46	0.39	0.14	3.61	3.47	-62.3
2008-06-09	0.44	0.33	0.10	2.71	0.68	-3.3
2008-11-27	0.42	0.33	0.11	2.02	1.40	36.8
2009-12-13	0.39	0.31	0.07	3.93	1.24	6.3
2010-07-24	0.37	0.31	0.09	4.11	1.44	10.9
2011-04-01	0.42	0.25	0.14	2.31	0.50	1.8
2011-11-13	0.42	0.32	0.10	3.04	0.78	4.8
2012-09-16	0.42	0.31	0.08	2.69	0.75	3.8

Note: [(a)] Total integrated and peak flux density as well as RMS of the 8.4 GHz image.
[(b)] Major and minor axis as well as the position angle of the synthesized beam.

Table B.6.: Model fit parameters of PKS 1440−389 at 8.4 GHz

Label	S[a] [Jy]	d[b] [mas]	ϕ[b] [°]	θ_{maj}[c] [mas]	θ_{min}[c] [mas]	P.A.[c] [°]	T_b[d] [10^9 K]
2009-02-27							
Core	0.085	0.14	25.4	0.60	0.33	19.9	8.461
C1	0.022	2.50	-131.8	2.66	2.66	6.0	0.062
2010-03-12							
Core	0.066	0.08	47.0	0.31	0.31	5.3	14.045
C1	0.015	2.36	-143.0	2.38	2.38	5.9	0.052
2010-10-28							
Core	0.067	0.08	6.5	0.45	0.23	45.6	12.691
C1	0.018	2.55	-134.6	2.11	2.11	11.1	0.078
2011-07-21							
Core	0.071	0.08	1.8	0.32	0.09	58.8	47.679
C1	0.018	2.24	-132.7	2.38	2.38	24.0	0.063
2012-04-27							
Core	0.068	0.08	29.3	0.19	0.19	19.7	37.530
C1	0.012	2.97	-148.9	3.01	3.01	9.3	0.027
2013-03-14							
Core	0.092	0.05	5.3	0.63	0.36	7.1	7.893
C1	0.012	2.29	-140.4	2.53	2.53	13.7	0.036

Note: (a) Integrated flux density
(b) Distance and position angle from the phase center
(c) Major and minor axes and position angle of the major axis
(d) Brightness temperature

Table B.7.: Model fit parameters of PKS 0447−439 at 8.4 GHz

Label	S^{a} [Jy]	d^{b} [mas]	ϕ^{b} [°]	$\theta_{maj}{}^{c}$ [mas]	$\theta_{min}{}^{c}$ [mas]	P.A.^{c} [°]	$T_b{}^{d}$ [10^9 K]
2009-02-27							
Core	0.103	0.03	-156.1	0.44	0.27	-9.2	17.601
C1	0.010	2.71	-41.4	1.67	1.67	39.3	0.076
2010-03-12							
Core	0.122	0.10	144.5	0.34	0.34	8.5	21.878
C1	0.011	2.27	-33.7	1.31	1.31	11.1	0.126
2010-10-28							
Core	0.107	0.03	173.4	0.27	0.18	81.7	45.885
C1	0.019	2.20	-49.9	1.69	1.69	-5.3	0.135
C2	0.003	7.30	-24.4	2.58	2.58	-10.9	0.009
2011-07-21							
Core	0.100	0.00	-23.5	0.39	0.27	-32.1	19.344
C1	0.008	2.68	-36.7	0.92	0.92	14.4	0.184
C2	0.003	6.02	-25.7	1.44	1.44	-17.5	0.031
2012-04-27							
Core	0.118	0.02	6.8	0.41	0.22	-4.0	27.489
C1	0.004	4.24	-21.5	1.36	1.36	1.8	0.040
C3	0.009	1.84	-33.4	0.62	0.62	20.4	0.491
2013-03-14							
Core	0.112	0.02	151.0	0.51	0.30	-5.0	14.791
C1	0.006	3.89	-30.4	1.93	1.93	22.2	0.032
C3	0.008	1.73	-51.0	0.30	0.30	0.0	1.889

Note: [(a)] Integrated flux density
[(b)] Distance and position angle from the phase center
[(c)] Major and minor axes and position angle of the major axis
[(d)] Brightness temperature

Table B.8.: Model fit parameters of PKS 2005−489 at 8.4 GHz

Label	S[a] [Jy]	d[b] [mas]	ϕ[b] [°]	θ_{maj}[c] [mas]	θ_{min}[c] [mas]	P.A.[c] [°]	T_b[d] [10^9 K]
2007-11-10							
Core	0.456	0.07	71.8	0.56	0.56	9.5	6.860
C1	0.121	2.15	-114.7	0.51	0.51	-7.8	8.584
C3	0.069	21.69	-132.7	6.82	6.82	18.3	0.028
2008-03-28							
Core	0.447	0.10	29.0	0.50	0.50	6.2	32.945
C1	0.218	2.17	-121.9	2.12	2.12	-1.7	0.898
C3	0.046	20.38	-136.3	4.22	4.22	6.5	0.048
2008-08-08							
Core	0.538	0.11	31.4	0.39	0.39	12.2	65.486
C1	0.277	2.07	-123.3	1.50	1.50	-24.8	2.280
C2	0.018	8.25	-146.2	3.74	3.74	0.0	0.024
C3	0.054	21.51	-139.7	11.50	11.50	3.7	0.008
2009-02-23							
Core	0.562	0.16	45.4	0.78	0.49	72.3	27.574
C1	0.220	2.36	-124.8	1.42	1.42	0.0	2.016
C2	0.024	6.84	-128.6	0.36	0.36	5.1	3.462
C3	0.038	19.36	-144.6	4.47	4.47	7.8	0.035
2009-12-13							
Core	0.537	0.05	48.4	0.52	0.52	3.8	37.253
C1	0.057	4.09	-123.6	0.66	0.66	12.1	2.465
C3	0.069	17.36	-141.3	10.23	10.23	25.0	0.012
2010-07-24							
Core	0.386	0.23	31.7	0.37	0.37	7.3	51.961
C1	0.178	2.04	-126.1	1.77	1.77	0.0	1.048
C3	0.098	19.28	-139.8	12.88	12.88	11.2	0.011
2011-04-01							
Core	0.477	0.05	-54.2	0.63	0.34	68.5	40.719
C1	0.224	2.17	-122.7	1.92	1.92	-24.9	1.131
C3	0.037	25.88	-143.4	2.26	2.26	16.4	0.134
2011-11-13							
Core	0.345	0.07	13.6	0.59	0.42	48.7	25.491
C1	0.136	2.08	-127.9	1.25	1.25	-2.1	1.617
C3	0.087	20.85	-138.1	19.49	19.49	-3.1	0.004
2012-09-16							
Core	0.346	0.12	19.3	0.48	0.48	0.0	27.250
C1	0.143	2.24	-129.6	0.63	0.63	-3.3	6.787
C2	0.031	5.77	-150.0	3.38	3.38	-20.6	0.051
C3	0.032	25.02	-145.0	4.61	4.61	5.4	0.028

Note: [(a)] Integrated flux density
[(b)] Distance and position angle from the phase center
[(c)] Major and minor axes and position angle of the major axis
[(d)] Brightness temperature

Table B.9.: Model fit parameters of PKS 2155−304 at 8.4 GHz

Label	S^{a} [Jy]	d^{b} [mas]	ϕ^{b} [°]	$\theta_{maj}{}^{c}$ [mas]	$\theta_{min}{}^{c}$ [mas]	P.A.^{c} [°]	$T_b{}^{d}$ [10^9 K]
2008-03-28							
Core	0.419	0.05	2.2	0.26	0.26	9.9	117.594
C1	0.047	2.22	149.6	1.95	1.95	19.4	0.242
C2	0.006	12.97	148.3	2.59	2.59	14.6	0.018
2008-08-08							
Core	0.393	0.02	12.4	0.51	0.51	8.7	29.749
C1	0.030	2.91	141.8	3.34	3.34	-1.2	0.052
C2	0.009	13.84	142.3	4.44	4.44	20.6	0.009
2009-02-27							
Core	0.336	0.04	-2.1	0.53	0.27	7.6	44.817
C1	0.016	4.53	110.1	0.44	0.44	11.3	1.559
C2	0.008	14.83	144.3	1.63	1.63	21.3	0.059
2009-09-05							
Core	0.286	0.04	-6.2	0.46	0.29	-27.1	41.031
C1	0.021	4.10	114.4	2.39	2.39	18.6	0.072
C3	0.007	3.50	171.5	0.80	0.80	21.6	0.198
C4	0.014	8.37	161.6	7.23	7.23	21.6	0.005
2010-03-12							
Core	0.207	0.02	-32.4	0.69	0.69	4.4	8.339
C1	0.029	6.02	125.1	6.01	6.01	14.6	0.015
2010-05-07							
Core	0.214	0.01	-97.8	0.56	0.28	-3.0	26.731
C1	0.035	2.29	125.9	3.32	3.32	2.6	0.061
C2	0.005	13.49	142.1	3.93	3.93	11.1	0.007
C3	0.004	4.21	-168.9	0.14	0.14	-11.8	4.345
2011-08-13							
Core	0.305	0.02	-17.0	0.38	0.38	15.0	40.837
C1	0.021	1.31	158.7	0.40	0.40	20.1	2.547
C2	0.012	16.89	139.2	5.30	5.30	16.5	0.008
C3	0.010	3.54	-173.9	1.03	1.03	-9.5	0.183
2012-09-15							
Core	0.326	0.01	-165.2	0.54	0.37	-0.6	31.693
C3	0.010	3.06	179.5	2.20	2.20	4.8	0.040

Note: [(a)] Integrated flux density
[(b)] Distance and position angle from the phase center
[(c)] Major and minor axes and position angle of the major axis
[(d)] Brightness temperature

Table B.10.: Model fit parameters of PKS 0625−354 at 8.4 GHz

Label	S[a] [Jy]	d[b] [mas]	ϕ[b] [°]	θ_{maj}[c] [mas]	θ_{min}[c] [mas]	P.A.[c] [°]	T_b[d] [10^9 K]
2007-11-10							
Core	0.310	0.03	4.0	0.40	0.19	-3.7	72.456
C1	0.032	2.73	144.6	1.17	1.17	5.3	0.425
C2	0.015	6.66	140.2	2.18	2.18	-1.1	0.058
C3	0.013	18.88	143.1	3.55	3.55	-1.4	0.019
2008-02-07							
Core	0.355	0.09	-39.7	≤ 0.10	≤ 0.10	0.0	≥ 648.703
C1	0.070	1.74	137.6	1.47	1.47	5.4	0.590
C2	0.017	4.74	131.9	0.32	0.32	18.4	3.029
C3	0.022	16.97	143.4	3.56	3.56	2.8	0.032
2008-06-09							
Core	0.337	0.07	-4.5	0.09	0.09	-1.7	824.875
C1	0.075	2.39	142.7	1.43	1.43	1.2	0.670
C2	0.031	6.22	145.7	0.33	0.33	-3.3	5.207
2008-11-27							
Core	0.358	0.02	-11.3	0.49	0.20	-10.2	65.192
C1	0.039	2.99	139.6	0.73	0.73	0.0	1.334
C2	0.013	6.54	140.9	1.40*	1.40*	1.1	0.121
C3	0.008	16.56	144.2	3.69	3.69	3.4	0.010
C4	0.003	23.80	145.2	1.67	1.67	4.8	0.023
2009-12-13							
Core	0.320	0.09	-1.0	0.35	0.35	3.7	46.502
C1	0.041	2.80	164.2	0.53	0.53	11.3	2.662
C2	0.011	8.24	146.4	1.24*	1.24*	15.8	0.131
C3	0.016	15.57	142.0	2.98	2.98	-19.7	0.033
2010-07-24							
Core	0.327	0.04	-11.9	0.53	0.37	-32.5	30.734
C1	0.022	3.52	139.8	0.55	0.55	4.7	1.334
C2	0.014	8.15	143.0	2.64	2.64	0.0	0.037
C3	0.010	18.66	145.0	2.38	2.38	0.0	0.031
2011-04-01							
Core	0.314	0.05	3.3	0.39	0.39	-2.8	37.503
C1	0.077	1.49	140.7	1.53	1.53	16.5	0.603
C2	0.019	3.94	142.7	0.53	0.53	19.5	1.263
2011-11-13							
Core	0.338	0.04	1.0	0.32	0.23	-77.7	83.031
C1	0.055	2.40	143.0	0.52	0.52	-2.7	3.686
C2	0.022	6.31	142.0	1.60	1.60	17.4	0.157
C3	0.007	17.19	145.9	2.39	2.39	-36.9	0.021
2012-09-16							
Core	0.342	0.04	-5.8	0.48	0.28	-32.6	46.590
C1	0.050	2.21	141.1	1.30	1.30	18.8	0.540
C2	0.016	6.58	140.9	1.86	1.86	18.4	0.085
C3	0.007	18.65	147.8	3.45	3.45	7.6	0.011

Note: [(a)] Integrated flux density
[(b)] Distance and position angle from the phase center
[(c)] Major and minor axes and position angle of the major axis
[(d)] Brightness temperature
Values marked with * are restricted to the minor axis of the beam to prevent divergence to a point source.

C. Additional Linear Fits

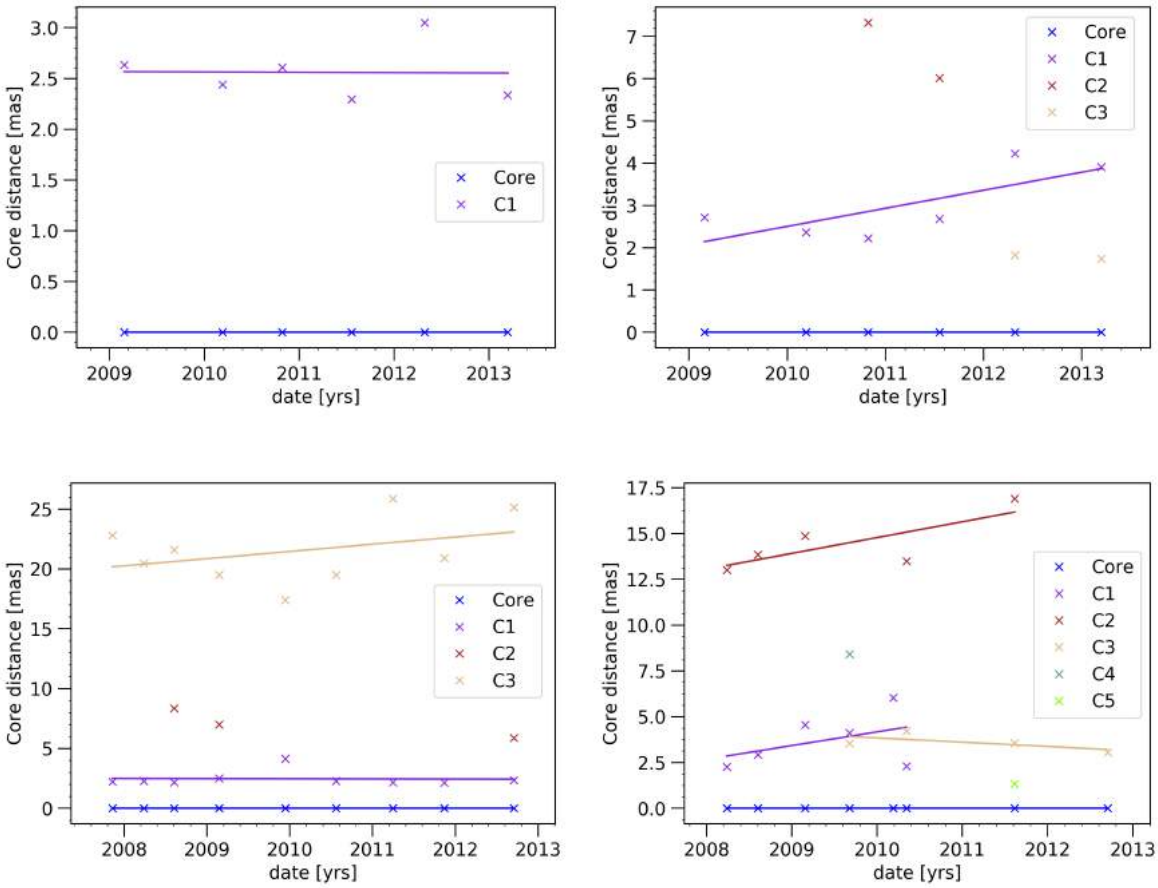

Figure C.1.: Distance to the core plotted vs time for PKS 1440−389 (upper left), PKS 0447−439 (upper right), PKS 2005−489 (lower left) and PKS 2155−304 (lower right). The solid lines are computed from unweighted linear regression.

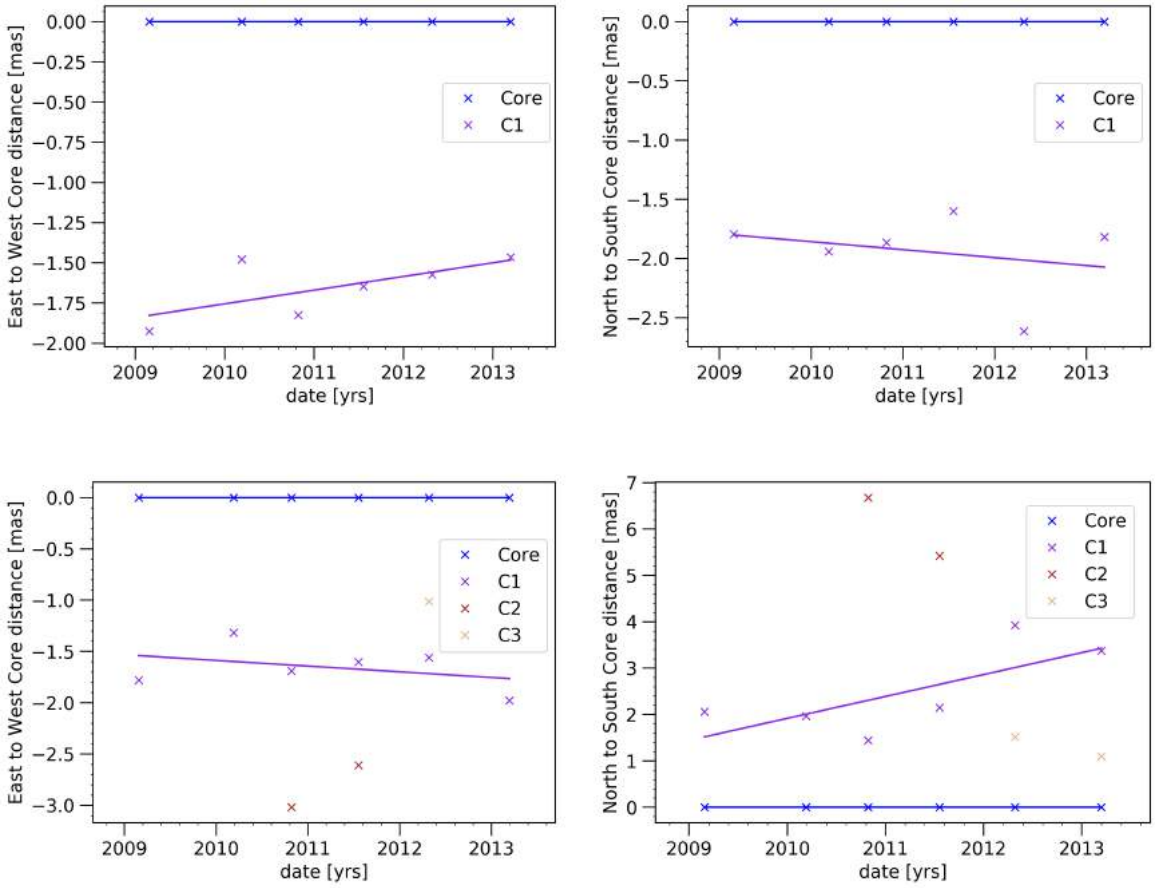

Figure C.2.: Separate x- and y-distance to the core plotted vs time for PKS 1440−389 (top) and PKS 0447−439 (bottom). The solid lines are computed from unweighted linear regression.

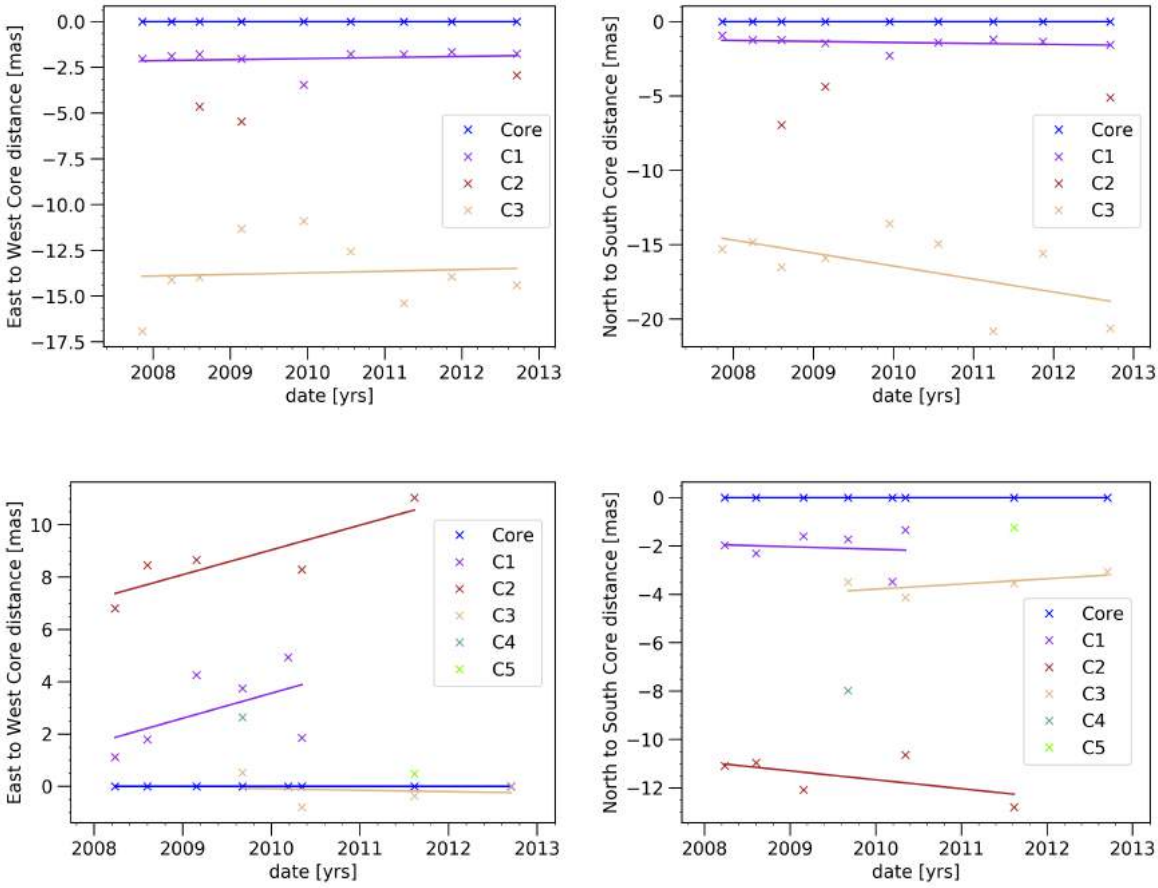

Figure C.3.: Separate x- and y-distance to the core plotted vs time for PKS 2005−489 (top) and PKS 2155−304 (bottom). The solid lines are computed from unweighted linear regression.

Declaration of authorship

I, Amar Hekalo, declare that this thesis titled 'VLBI monitoring of Five TeV Blazars' and the work presented in it are my own. I confirm that:

- This work was done wholly or mainly while in candidature for a research degree at this University.
- Where any part of this thesis has previously been submitted for a degree or any other qualification at this University or any other institution, this has been clearly stated.
- Where I have consulted the published work of others, this is always clearly attributed.
- Where I have quoted from the work of others, the source is always given. With the exception of such quotations, this thesis is entirely my own work.
- I have acknowledged all main sources of help.
- Where the thesis is based on work done by myself jointly with others, I have made clear exactly what was done by others and what I have contributed myself.

Location, Date

Amar Hekalo